2011

Deep 1.1 mm-wavelength imaging of the GOODS-South field by AzTEC/ASTE -- II. Redshift distribution and nature of the submillimetre galaxy population

Min S. Yun
K. S. Scott
Yicheng Guo
I. Aretxaga
Mauro Giavalisco, *University of Massachusetts - Amherst*, et al.

Deep 1.1 mm-wavelength imaging of the GOODS-South field by AzTEC/ASTE – II. Redshift distribution and nature of the submillimetre galaxy population

Min S. Yun,[1] K. S. Scott,[2] Yicheng Guo,[1] I. Aretxaga,[3] M. Giavalisco,[1]
J. E. Austermann,[4] P. Capak,[5] Yuxi Chen,[1] H. Ezawa,[6] B. Hatsukade,[7]
D. H. Hughes,[3] D. Iono,[8] S. Johnson,[1] R. Kawabe,[8] K. Kohno,[9]
J. Lowenthal,[10] N. Miller,[11] G. Morrison,[12,13] T. Oshima,[8] T. A. Perera,[14]
M. Salvato,[15] J. Silverman,[16] Y. Tamura,[9] C. C. Williams,[1] and G. W. Wilson,[1]

[1] *Department of Astronomy, University of Massachusetts, Amherst, MA 01003, USA*
[2] *Department of Physics & Astronomy, University of Pennsylvania, 209 South 33rd Street, Philadelphia, PA 19104, USA*
[3] *Instituto Nacional de Astrofísica, Óptica y Electrónica, Tonantzintla, Puebla, México*
[4] *Center for Astrophysics and Space Astronomy, University of Colorado, Boulder, CO 80309, USA*
[5] *Spitzer Science Center, 314-6 California Institute of Technology, 1200 East California Boulevard, Pasadena, CA 91125, USA*
[6] *ALMA Project Office, National Astronomical Observatory of Japan, 2-21-1 Osawa, Mitaka, Tokyo 181-8588, Japan*
[7] *Department of Astronomy, Kyoto University, Kyoto 606-8502, Japan*
[8] *Nobeyama Radio Observatory, National Astronomical Observatory of Japan, Minamimaki, Minamisaku, Nagano 384-1305, Japan*
[9] *Institute of Astronomy, University of Tokyo, 2-21-1 Osawa, Mitaka, Tokyo 181-0015, Japan*
[10] *Smith College, Northampton, MA 01063, USA*
[11] *Department of Astronomy, University of Maryland, College Park, MD 20742, USA*
[12] *Institute for Astronomy, University of Hawaii, Manoa, HI 96822, USA*
[13] *Canada-France-Hawaii Telescope Corp., Kamuela, HI 96743, USA*
[14] *Department of Physics, Illinois Wesleyan University, Bloomington, IL 61701, USA*
[15] *Max-Planck Institute for Plasma Physics & Cluster of Excellence, Boltzmann Strasse 2, 85748 Garching Germany*
[16] *Institute for the Physics and Mathematics of the Universe (IPMU), University of Tokyo, Kashiwa 277-8582, Japan*

29 September 2011

ABSTRACT
We report the results of the counterpart identification and a detailed analysis of the physical properties of the 48 sources discovered in our deep 1.1mm wavelength imaging survey of the GOODS-South field using the AzTEC instrument on the Atacama Submillimeter Telescope Experiment (ASTE). One or more robust or tentative counterpart candidate is found for 27 and 14 AzTEC sources, respectively, by employing deep radio continuum, *Spitzer* MIPS & IRAC, and LABOCA 870 μm data. Five of the sources (10%) have two robust counterparts each, supporting the idea that these galaxies are strongly clustered and/or heavily confused. Photometric redshifts and star formation rates ($SFRs$) are derived by analyzing UV-to-optical and IR-to-radio SEDs. The median redshift of $z_{med} \sim 2.6$ is similar to other earlier estimates, but we show that 80% of the AzTEC-GOODS sources are at $z \geqslant 2$, with a significant high redshift tail (20% at $z \geqslant 3.3$). Rest-frame UV and optical properties of AzTEC sources are extremely diverse, spanning 10 magnitude in the $i-$ and $K-$band photometry (a factor of 10^4 in flux density) with median values of $i = 25.3$ and $K = 22.6$ and a broad range of red colour ($i - K$ =0-6) with an average value of $i - K \approx 3$. These AzTEC sources are some of the most luminous galaxies in the rest-frame optical bands at $z \geqslant 2$, with inferred stellar masses $M_* = (1-30) \times 10^{10} M_\odot$ and UV-derived star formation rates of $SFR_{UV} \gtrsim 10^{1-3} M_\odot$ yr^{-1}. The IR-derived SFR, 200-2000 $M_\odot$ yr^{-1}, is independent of z or M_*. The resulting specific star formation rates, $SSFR \approx$ 1-100 Gyr^{-1}, are 10-100 times higher than similar mass galaxies at $z = 0$, and they extend the previously observed rapid rise in the $SSFR$ with redshift to $z = 2 - 5$. These galaxies have a SFR high enough to have built up their *entire* stellar mass within their Hubble time. We find only marginal evidence for an AGN contribution to the near-IR and mid-IR SEDs, even among the X-ray detected sources, and the derived M_* and SFR show little dependence on the presence of an X-ray bright AGN.

1   INTRODUCTION

Early studies of the far–infrared (FIR) cosmic background indicated that up to half of the cosmic energy density is generated by dusty starbursts and active galactic nuclei (Fixsen et al. 1998; Pei et al. 1999). Deep, wide field surveys at 850μm (Smail et al. 1997; Barger et al. 1998; Hughes et al. 1998; Eales et al. 1999, 2000; Cowie et al. 2002; Scott et al. 2002; Webb et al. 2003a; Serjeant et al. 2003; Wang et al. 2004; Coppin et al. 2006) with the Submillimeter Common–User Bolometric Array (SCUBA; Holland et al. 1999) on the James Clerk Maxwell Telescope (JCMT), and later surveys at millimetre wavelengths (Borys et al. 2003; Greve et al. 2004; Laurent et al. 2005; Bertoldi et al. 2007; Greve et al. 2008; Perera et al. 2008; Scott et al. 2008; Austermann et al. 2010; Scott et al. 2010), revealed that this IR background is resolved into a large population of discrete individual sources.

Identifying and understanding the nature of these discrete FIR sources ("submillimetre galaxies" or SMGs) has proven to be challenging because of the low angular resolution of these instruments and the faintness of counterparts in the rest-frame optical and UV-bands (see review by Blain et al. 2002). Utilizing sub-arcsec astrometry of interferometric radio continuum data and sensitive spectroscopy using the Keck telescopes, Chapman et al. (2005) reported spectroscopic redshifts of 73 SMGs culled from earlier SCUBA surveys and concluded that they are massive, young objects seen during their formation epoch, with very high star formation rates at $z > 1$. Deep 24 μm band imaging using the Multiband Imaging Photometer for *Spitzer* (MIPS; Rieke et al. 2004) on the *Spitzer* Space Telescope and follow-up spectroscopy using the Infrared Spectrograph (IRS; Houck et al. 2004) have also provided useful insights on the nature and redshifts of additional SMGs (Lutz et al. 2005; Menéndez-Delmestre et al. 2007; Valiante et al. 2007; Pope et al. 2008a; Menéndez-Delmestre et al. 2009; Huang et al. 2009). However, the use of high resolution radio continuum and MIPS 24 μm images for the counterpart identification suffers from a well-known systematic bias against high redshift ($z \gtrsim 3$) sources. Indeed, a large fraction of the counterpart sources identified using direct interferometric imaging in the mm/submm wavelengths are shown to be extremely faint in nearly all other wavelength bands ($r > 26, K > 24$) *with little or no radio or MIPS 24 μm emission* (Iono et al. 2006; Wang et al. 2007; Younger et al. 2007, 2009), and high redshift SMGs may have been missed or mis-identified with a foreground source in the earlier studies.

Obtaining a more complete understanding of the SMG population requires a study of a larger, more uniform sample identified utilizing the deepest available multiwavelength complementary data and a robust counterpart identification method that is less prone to a redshift bias. In this paper we present the identification of the 48 AzTEC 1.1 mm sources found in the deepest survey at mm wavelengths ever carried out in the Great Observatories Origins Deep Survey-South (GOODS-S) field by Scott et al. (2010, "Paper I" hereafter). Several different identification methods are employed simultaneously to complement and to calibrate each other. A thorough analysis of the counterpart properties and redshift distribution is also carried out as the

GOODS-S field represents one of the most widely studied regions of sky with some of the deepest multi-wavelength data: X-ray data from *Chandra* (Luo et al. 2008; Xue et al. 2011; Johnson et al. 2011), optical to near-IR photometry from the *Hubble Space Telescope* (*HST*; Giavalisco et al. 2004), *Spitzer* IRAC (Dickinson et al. in prep.) and MIPS (Chary et al. in prep.) imaging in the mid-IR, submm imaging at $250 - 500$ μm with the Balloon-borne Large Aperture Submillimeter Telescope (BLAST; Devlin et al. 2009), and 1.4 GHz interferometric imaging with the Very Large Array (VLA; Kellermann et al. 2008; Miller et al. 2008). Extensive spectroscopy of optical sources in this field is also available (Le Fevre et al. 2004; Szokoly et al. 2004; Mignoli et al. 2005; Vanzella et al. 2005, 2006; Norris et al. 2006; Kriek et al. 2008; Vanzella et al. 2008; Popesso et al. 2009; Treister et al. 2009; Wuyts et al. 2009; Balestra et al. 2010; Silverman et al. 2010; Casey et al. 2011). Including the AzTEC GOODS-North field sources (Perera et al. 2008; Chapin et al. 2009), our combined AzTEC-GOODS sample includes ~ 80 SMGs identified using a uniform set of criteria and the deepest multiwavelength data available and offers the best opportunity yet to examine the nature of the SMGs as a population and to verify the conclusions of earlier studies of mostly smaller and often radio-selected samples (Lilly et al. 1999; Fox et al. 2002; Ivison et al. 2002; Webb et al. 2003b; Borys et al. 2004; Chapman et al. 2005; Ivison et al. 2007; Clements et al. 2008).

2   COUNTERPART IDENTIFICATION

Here we describe the methods of identifying multiwavelength counterparts to the 48 AzTEC GOODS-S (AzTEC/GS hereafter) sources reported by Scott et al. (2010). We adopt the updated AzTEC source positions and photometry derived using the improved point source kernel by Downes et al. (2011). Our counterpart identification relies primarily on three observed multi-wavelength properties: (1) high resolution radio continuum; (2) *Spitzer* MIPS 24 μm photometry; and (3) red colors in the *Spitzer* IRAC bands. A robust counterpart is identified using a combination of these criteria for most AzTEC sources, and proposed identifications and multi-wavelength photometry for each of the AzTEC 1.1 mm sources are summarized in Table 1 and Table 2. A more detailed discussion of the individual identification and the nature of the individual counterpart candidates are discussed in Appendix A.

2.1   Methods

Since the origin of the millimetre continuum emission detected by the AzTEC instrument is likely reprocessed radiation from dust-obscured starburst or AGN activity, the main data sets we examine for the multi-wavelength counterpart identification are mid-IR data from the *Spitzer* MIPS 24 μm (full width at half maximum angular resolution of $\theta_{\mathrm{FWHM}} \sim 6''$) and IRAC 3.6 to 8.0 μm band ($\theta_{\mathrm{FWHM}} \sim 2''$) and deep radio continuum data obtained using the VLA ($\theta_{\mathrm{FWHM}} \sim 2''$), exploiting the well-known radio-IR correlation for star-forming galaxies (see review by Condon 1992). The *Spitzer* IRAC and MIPS images and catalogues used

come from the *Spitzer* GOODS[1], the FIDEL[2], and the SIMPLE[3] Legacy Surveys. The radio continuum data used come from the VLA 1.4 GHz deep imaging survey ($\sigma \sim 8\mu$Jy; Miller et al. 2008; Kellermann et al. 2008). Given their high resolution, the astrometric accuracy of these catalogues are sufficient to identify unique optical and near-IR counterparts in the deep ground-based telescope or HST images when such a counterpart is present. The $i-$band and $K-$band photometry of the counterpart candidates are also reported from the band-merged GOODS team photometry catalogue (Grogin et al., in prep.) constructed using a template fitting software package TFIT (Laidler et al. 2007) and the MUSYC survey (Gawiser et al. 2006).

Unlike most previous works, we employed a variable search radius based on the beam size ($\theta_{\mathrm{FWHM}} \sim 30''$) and the S/N of the AzTEC detection. Given the modest S/N (typically $\leqslant 10$), the positional offset between an AzTEC source and its counterpart is expected to be dominated by the map noise. This means we can exploit the measured S/N of each detection to constrain the counterpart identification. We derive the search radius, R_S, listed in Table 1 empirically through simulations by injecting artificial sources into the signal map one at a time and measuring the distribution in the input to output source positions as described in Paper I. For each AzTEC source we select R_S such that there is a 95% probability that the true position of the source (assumed to be the position of the radio and/or Spitzer counterpart) will be within R_s of the AzTEC centroid.

The primary method of identifying AzTEC counterparts is the "$P-$statistic" described by Downes et al. (1986). This method computes the likelihood of a chance coincidence for each source in the comparison catalogue from the measured catalogue source density and the distance to a given AzTEC source position. Following previous work, a counterpart with a $P-$statistic less than 0.05 is deemed a "robust" identification, while a counterpart with $0.05 < P < 0.20$ is considered a "tentative" identification. Unlike most works, however, we compute all P-statistics based on the number density of *all* sources in the comparison catalog, rather than the number density of sources *brighter* than the candidate counterpart in question. This means that all candidate counterparts equidistant from the AzTEC centroid will have the same P-statistic. This avoids biasing the identifications to the brightest radio and mid-IR sources, which could result in more misidentifications with low-redshift galaxies.

For the radio data, we created a $\geqslant 4\sigma$ catalog using the SAD program in the Astronomical Image Processing System (AIPS)[4]. This program builds a catalog iteratively by first identifying bright pixels and then quantitatively testing their significance by fitting the PSF to the surrounding pixel brightness distribution. By allowing for a collection of connected sources as an acceptable model, this algorithm also provides a good estimate of the radio flux for extended objects as well. Submm/mm galaxies are almost always associated with IRAC galaxies with faint but visible radio

emission. The extremely deep Spitzer data in these GOODS fields ensures that radio sources without an IRAC counterpart are rare as reported by Kellermann et al. (2008), who find that only three out of 266 cataloged radio sources have no apparent counterpart at any other wavelengths. Taking advantage of this fact, we probe deeper into the radio data by creating a combined IRAC+VLA radio catalog by using the positions of IRAC sources detected with $(S/N)_{3.6} \geqslant 4$ as prior positions. For each IRAC source, we fit a 2-D Gaussian to the radio map at the IRAC position, fixing the FWHM to $1.6''$ and $2.8''$ in RA and Dec, respectively, based on the best-fit Gaussian to the synthesized beam (Miller et al. 2008). We limit the location of the peak to within $2''$ of the initial IRAC position. If the best-fit 1.4 GHz peak emission is $> 3\sigma$ of the rms noise in the surrounding region, we include this in our combined IRAC+VLA catalog. This list is cross-checked with the $> 4\sigma$ radio catalog created by the SAD program, and we use the SAD catalogue flux estimates where available. The number density of IRAC+VLA sources in this catalog is $8330\,\mathrm{deg}^{-2}$ for the GOODS-S+VLA catalog, and $7860\,\mathrm{deg}^{-2}$ for the shallower SIMPLE+VLA catalog.

For the MIPS 24 µm catalogues, we use the number density of $(S/N)_{24} \geqslant 4$ sources to compute the P-statistics, which are $45700\,\mathrm{deg}^{-2}$ and $25600\,\mathrm{deg}^{-2}$ for the GOODS-S and FIDEL 24 µm catalogs, respectively.

The third and an entirely new method we use for identifying SMG counterparts employs their characteristic red IRAC color. Interferometric imaging studies of SMGs in submillimetre continuum (Iono et al. 2006; Wang et al. 2007, 2011; Younger et al. 2007, 2008, 2009; Hatsukade et al. 2010; Tamura et al. 2010; Ikarashi et al. 2011) have shown that every source is detected in the IRAC 3.6 µm and 4.5 µm bands at the $\geqslant 1\mu$Jy level, while their radio and MIPS 24 µm counterparts are not always detected in the best available data. By examining the spectral energy distribution (SED) of these IRAC counterparts, Yun et al. (2008) showed that SMGs as a population have characteristic red IRAC colors, similar to dust obscured AGN as proposed by Lacy et al. (2004) and Stern et al. (2005). These SMGs are systematically offset from the color region associated with power-law AGN, however. Citing theoretical color tracks of dust obscured starbursts, Yun et al. advocated a dust-obscured young stellar population as the origin of the red IRAC color (see their Figs. 1 & 2). Objects with red IRAC color are rare (~ 1 arcmin^{-2} for $[3.6] - [4.5] \geqslant 0.0$) and distinct from the large number of foreground galaxies with characteristically *blue* IRAC colors. Both of these qualities can be successfully exploited for distinguishing the SMG counterpart candidates. Several color combinations are proposed by Yun et al., and we adopt here the simplest form, $[3.6] - [4.5] \geqslant 0.0$, since these two bands are the most sensitive and the most robust among the four IRAC bands. In computing P-statistics for the IRAC counterparts, we thus use the number density of IRAC sources with $[3.6] - [4.5] \geqslant 0.0$, $(S/N)_{3.6} > 4$, and $S_{3.6} > 1\mu$Jy. These are $36900\,\mathrm{deg}^{-2}$ and $31400\,\mathrm{deg}^{-2}$ for the GOODS-S and SIMPLE IRAC catalogs, respectively.

Examining the *Spitzer* IRAC and MIPS properties of 73 radio-selected SMGs, Hainline et al. (2009) reported that an IRAC color selection method similar to what we adopted is more successful in identifying correct counterparts than the IRAC color-magnitude selection method described by Pope et al. (2006), but they caution that the density of

---

sources meeting the Yun et al. (2008) color selection criteria is high enough to diminish the utility of this method. We adopt a more selective limit of $[3.6] - [4.5] \geqslant 0.0$, which is more effective in reducing the foreground confusion. In addition, we also employ a $P-$statistic analysis to give our method a more discriminative power.

2.2   Counterpart Identification Results

Finding charts for the 48 AzTEC/GS sources (GS2 is split into two) are shown in Fig. 1 in the order they appeared in Scott et al. (2010). Sources meeting the radio, MIPS 24 µm, and red IRAC color selection criteria are identified in each $30'' \times 30''$ image centered on the AzTEC source position. A unique counterpart is easily identifiable in about 50% of the cases while two or more candidates are present in others, requiring a more systematic and quantitative analysis.

Candidate radio and *Spitzer* counterparts and their computed $P-$statistics are given in Table 1. All "robust" counterparts satisfying $P \leqslant 0.05$ in any of the 3 bands are highlighted in bold-faced letters based on the analysis of the radio ($P_{1.4}$), MIPS 24 µm ($P_{24\mu}$), or the IRAC color (P_{color}) properties. For 21 out of 48 cases, an 870 µm LABOCA source (Weiss et al. 2009) is found within a $10''$ radius. Given the extremely low source density at 870 µm, the likelihood of a chance coincidence is essentially zero. Therefore, we elevate the status of the 13 AzTEC/GS sources initially classified as only as a "tentative" identification based on the 3 bands analysis to "robust" by folding in the astrometry of the $19''$ resolution 870 µm LABOCA Survey data (see Appendix A and Table 1) – the remaining AzTEC-LABOCA sources are already classified as "robust". We note that the low rate of coincidence between the LABOCA and AzTEC surveys ($21/48 = 44\%$) can be largely accounted by the low S/N detections of sources in both surveys, although the presence of high redshift ($z > 3$) sources detected by AzTEC at 1.1mm (e.g., Eales et al. 2003) may play a role. Taking advantage of the available rich multiwavelength database, we provide complete photometry for each source in Table 2.

A robust counterpart is identified for 27 (56%) out of 48 AzTEC/GS sources using the $P-$statistic analysis combined with the LABOCA comparison. A total of 13, 8, and 5 AzTEC sources have a robust counterpart based solely on the radio, MIPS 24 µm, or IRAC color analysis, respectively. An additional 19, 14, and 18 have tentative identifications with $0.05 < P < 0.20$, respectively. The robust radio and MIPS 24 µm identification rates of 13/48 (27%) and 8/48 (17%) are consistent with other similar studies. For example, using similar depth *Spitzer* data and slightly deeper radio data in the GOODS-North field, Pope et al. (2006) reported robust identification rates of 21/35 (60%) and 6/35 (17%) for the 1.4 GHz radio and MIPS 24 µm data and additional 10 and 6 tentative identifications, respectively. For the SCUBA Half Degree Extragalactic Survey (SHADES), Ivison et al. (2007) reported 56% and 54% robust identification using much shallower MIPS 24 µm and comparable depth radio data.[5] The frequency of robust counterpart identification rate using red IRAC color is similar to the MIPS 24 µm identification rate, indicating that their respective candidate source density is comparable.

Five AzTEC/GS sources (10%) have two robust counterparts each. This multiple robust candidate identification rate is similar to those found in the GOODS-North field (Pope et al. 2006; Chapin et al. 2009) and the SHADES fields (Ivison et al. 2007; Clements et al. 2008). This multiple identification frequency is about 40 times higher than one would expect at random. A distinct possibility is that AzTEC counterpart sources are intrinsically strongly clustered (see Williams et al. 2011, and references therein), and the $P-$statistic computes implicitly the likelihood that a particular candidate is *either the AzTEC counterpart or a close companion*. A strong clustering of SMGs is also expected if they represent a rapid build-up of stellar mass for $\geqslant M_*$ galaxies associated with a $\gtrsim 10^{12} M_\odot$ dark matter halo – see discussions by Blain et al. (2004). Similar SEDs and redshifts of the multiple candidate counterparts for AzTEC/GS19, AzTEC/GS31, and GN19 (Pope et al. 2006) offer further anecdotal evidence for the clustering explanation. Wang et al. (2011) has reported two examples where a single SMG is broken up into multiple discrete components when observed at high angular resolution with an interferometer, further supporting the clustering scenario. Based on the simulations of two large gas-rich galaxies, Hayward et al. (2011) have suggested that some fraction of SMGs may be such closely interacting pairs just prior to a merger, and such a scenario would certainly boost the pair fraction. Uncertainties in the parameters chosen for the simulations, such as the details of the progenitors and the microphysics of star formation and gas consumption, make the comparison with the observed statistics difficult. These new observations should serve as important observational constraints for future modeling studies.

As shown in Table 2, only 22 out of 47 AzTEC/GS sources have an 870 µm LABOCA counterpart in the published catalog by Weiss et al. (2009). Utilizing the radio and MIPS 24 micron P-statistic and the IRAC 3.6 and 5.8 µm color-magnitude selection by Pope et al. (2006), Biggs et al. (2011) identified 16 secure and 3 tentative counterparts among these 22 sources in common. In comparison, we identify 16 robust counterparts based on the P-statistics alone, and all 19 individual candidates identified by Biggs et al. is either a robust (8) or tentative (11) counterpart in Table 1. The agreement between our results and theirs is very good mostly because both groups rely heavily on the radio continuum data for the counterpart identification.

2.3   Counterpart Identification for SMGs in GOODS-North

To improve the statistics of the subsequent analysis, we also apply the same counterpart identification methods to the AzTEC 1.1mm sources identified in the GOODS-North field

---

[5] The MIPS 24 µm robust detection rate by Ivison et al. (2007) is significantly higher than ours or by Pope et al. (2006), despite their much shallower data, and this analysis may be in error.

Although the majority of radio-identified sources in Table 1 as well as by Pope et al. have a MIPS 24 µm counterpart, the MIPS 24 µm source density is also much higher than the radio, leading to a greater chance-coincidence and thus a higher $P-$value in general.
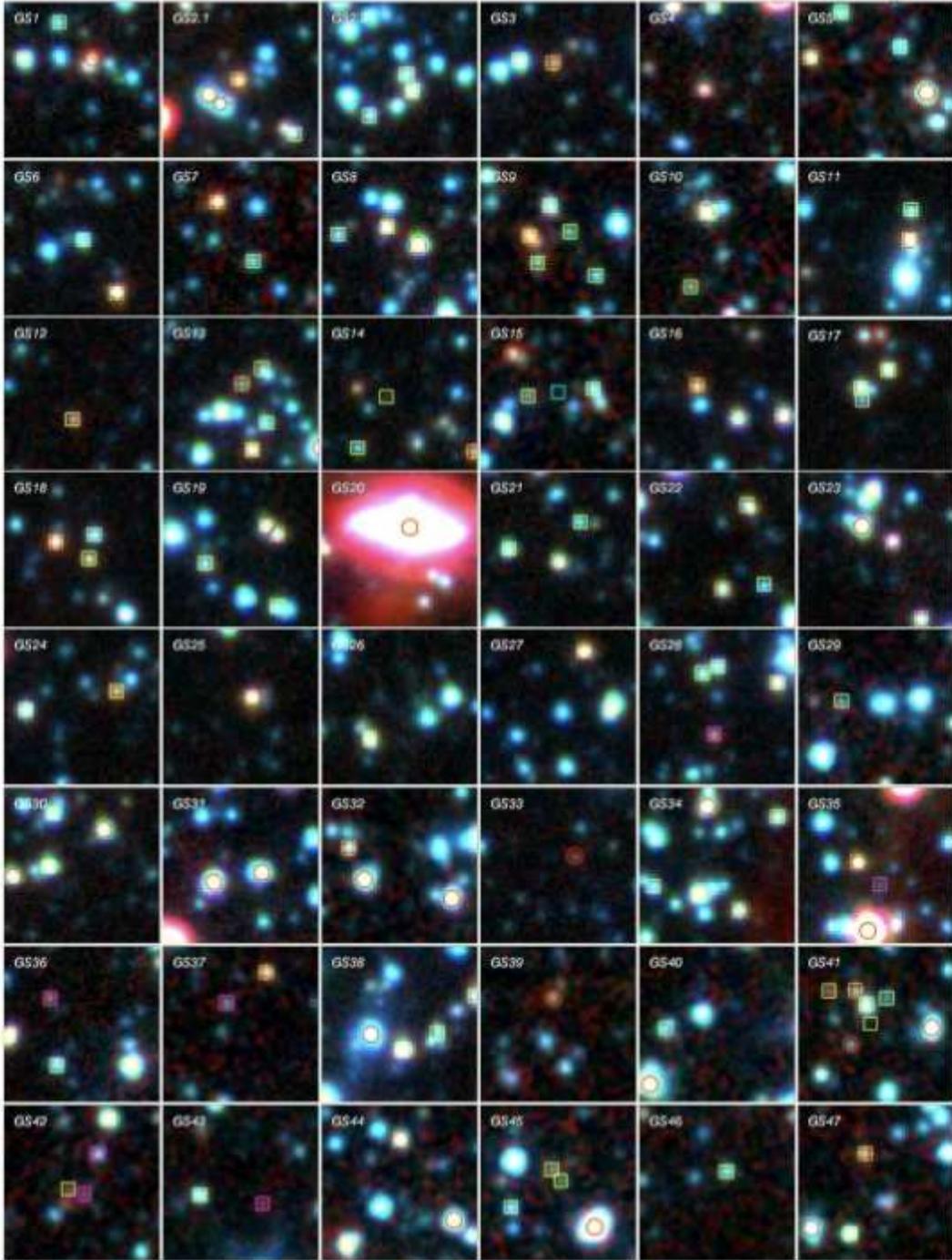
Figure 1. Finding charts for the 48 AzTEC/GS sources. These false color images are $30'' \times 30''$ in size and produced using the IRAC 3.6 µm (blue), 4.5 µm (green), and 8.0 µm (red) band images. Red circles mark the 1.4 GHz radio sources while yellow squares are MIPS 24 µm sources. For sources without a plausible radio or MIPS 24 µm counterpart, IRAC sources with red IRAC color ([3.6] − [4.5] > 0) are identified using magenta squares.

Table 1. Radio and *Spitzer* identifications of AzTEC sources (procedure described in Section 2). The counterpart search radius R_S and the likelihood P values are described in detail in the text (§ 2), and robust counterparts are emphasized in boldface. Spectroscopic redshifts are given in the column labeled $z_{\rm spec}$ (references for these measurements are given in Appendix A).

AzTEC ID	R_S ($''$)	radio coordinate (J2000)	Dist. ($''$)	*Spitzer* coordinate (J2000)	Dist. ($''$)	$P_{1.4}$	$P_{24\mu}$	P_{color}	[3.6]−[4.5] (mag)	$z_{\rm spec}$
GS1a	4.7	**J033211.37-275212.1**	4.8	J033211.36-275213.0	4.0	**0.045**	0.161	0.133	+0.37	...
GS2.1a	4.5	**J033219.06-275214.6**	0.8	**J033219.05-275214.3**	0.7	**0.001**	**0.006**	**0.005**	+0.38	...
GS2.1b		**J033219.14-275218.1**	3.9	...	...	**0.030**	...	...	...	...
GS2.1c		...	...	J033218.75-275212.7	3.9	...	0.154	...	-0.32	0.644
GS2.2a	8.7	...	...	J033216.62-275243.3	4.6	...	0.212	...	-0.23	1.046
GS2.2b		...	...	J033216.52-275246.5	7.4	...	0.457	0.390	+0.26	...
GS2.2c		...	...	J033216.75-275249.5	8.0	...	...	0.439	+0.10	...
GS3a	5.9	**J033247.99-275416.4**	4.8	J033247.96-275416.3	4.6	**0.045**[a]	0.211	0.174	+0.37	...
GS3b		...	...	J033247.70-275423.5	3.8	...	...	0.123	+0.14	...
GS4a	6.5	**J033248.97-274252.0**	3.2	J033248.96-274251.6	2.8	**0.021**[a]	...	0.070	+0.28	...
GS5a[d]	7.1	J033151.11-274437.5	6.4	J033151.08-274437.0	6.5	0.075	0.233[b]	0.274[c]	+0.23	**1.599**
GS5b		J033152.81-274430.3	17.4	J033152.80-274429.6	17.5	0.438	0.850[b]	0.903[c]	+0.43	...
GS6a[d]	7.5	J033225.27-275230.6	12.4	J033225.25-275230.2	12.2	0.268[a]	0.809	0.737	+0.45	...
GS6b		...	...	**J033225.76-275220.0**	0.4	...	**0.002**	...	-0.23	**1.102**
GS7a[d]	8.7	J033213.84-275600.2	8.4	J033213.85-275559.9	8.7	0.126	0.366[b]	0.439[c]	+0.46	**2.676**
GS7b		...	...	J033213.31-275611.5	4.9	...	0.151[b]	0.168[c]	+0.04	...
GS8a	8.7	**J033204.90-274647.4**	4.4	J033204.87-274647.3	4.5	**0.038**	0.203	0.168	+0.33	**2.252**
GS8b		...	...	J033205.35-274644.0	2.9	...	0.089	0.072	+0.17	...
GS9a	8.7	J033303.02-275146.5	6.2	J033302.99-275146.2	5.9	0.070	0.140[b]	0.232[c]	+0.52	...
GS9b		...	...	J033302.44-275145.3	3.5	...	0.090[b]	0.089[c]	+0.29	...
GS9c		...	...	J033302.90-275151.0	5.1	...	...	0.179[c]	+0.32	...
GS10a[d]	9.0	J033207.30-275120.8	5.3	J033207.27-275120.1	5.9	0.053	0.181[b]	0.233[c]	+0.14	**2.035**
GS10b		...	...	J033207.09-275128.9	3.2	...	...	0.077[c]	+0.04	...
GS11a	9.0	J033215.33-275037.6	6.5	J033215.29-275038.3	6.8	0.081	0.404	...	-0.02	...
GS12a	9.0	**J033229.30-275619.9**	4.0	J033229.29-275619.2	3.3	**0.032**[a]	0.113	0.092	+0.10	**4.762**
GS13a	9.0	**J033211.94-274615.3**	2.1	**J033211.92-274615.2**	2.2	**0.009**[a]	**0.050**	**0.041**	+0.24	...
GS13b		J033211.60-274613.0	5.7	J033211.56-274613.0	6.1	0.065[a]	0.338	0.283	+0.02	1.039
GS13c		J033212.23-274621.6	6.3	J033212.22-274620.6	5.5	0.076[a]	0.285	...	-0.25	1.033
GS14a[d]	9.0	...	...	J033234.73-275217.3	3.1	...	...	0.083	+0.04	**3.640**
GS15a[d]	9.0	J033151.61-274552.1	12.7	J033151.54-274553.1	11.3	0.264[a]	...	0.619[c]	+0.44	...
GS15b		...	...	J033151.36-274601.0	5.6	...	...	0.215[c]	+0.05	...
GS15c		...	...	J033150.97-274554.7	6.4	...	...	0.264[c]	+0.00	...
GS16a	10.5	J033238.00-274400.8	6.1	J033238.00-274400.6	6.2	0.072[a]	0.345	0.290	+0.53	1.719
GS16b		J033237.35-274407.8	7.9	J033237.40-274407.0	7.0	0.119[a]	0.419	...	-0.29	1.017
GS17a	10.5	**J033222.54-274818.2**	1.8	**J033222.54-274817.6**	1.2	**0.007**[a]	**0.017**	...	-0.27	...
GS17b		...	...	**J033222.54-274814.9**	1.5	...	**0.026**	**0.021**	+0.19	...
GS17c		...	...	J033222.15-274811.3	7.0	...	0.415	0.351	+0.36	...
GS17d		J033222.53-274804.6	11.8	J033222.51-274804.6	11.8	0.245	...	0.710	+0.23	...
GS17e		J033222.26-274804.8	12.1	J033222.26-274804.3	12.5	0.254[a]	0.824	0.755	+0.32	...
GS18a	9.3	**J033243.48-274639.5**	4.2	J033243.52-274639.1	3.7	**0.035**[a]	0.138	0.113	+0.47	...
GS18b		J033243.98-274635.9	5.2	J033244.01-274635.2	5.5	0.053[a]	0.288	0.240	+0.31	2.688
GS18c		...	...	J033243.45-274634.3	2.3	...	0.058	...	-0.39	...
GS19a	10.5	J033222.92-274125.4	7.3	J033222.87-274124.9	8.0	0.102	0.509	0.438	+0.22	...
GS19b		J033222.70-274126.7	8.7	J033222.70-274126.4	8.8	0.143	...	0.501	+0.36	...
GS19c		...	...	J033223.76-274131.5	6.6	...	0.181[b]	0.280[c]	+0.17	...
GS20a	10.5	**J033235.09-275532.6**	4.6	J033235.06-275532.7	4.5	**0.042**	0.200	...	-0.43	**0.0369**
GS21a	10.4	J033247.58-274452.4	7.5	J033247.59-274452.2	7.4	0.108	0.452	0.385	+0.24	1.910
GS21b		...	...	J033247.29-274444.3	2.5	...	0.065	0.053	+0.13	...
GS22a	13.0	J033212.56-274305.9	7.8	J033212.54-274306.1	7.9	0.116[a]	0.502	0.431	+0.30	1.794
GS22b		...	...	J033212.56-274252.9	5.4	...	...	0.231	+0.13	...
GS23a	12.2	**J033221.14-275626.6**	3.9	J033221.12-275626.5	4.2	**0.030**[a]	0.176	0.145	+0.45	...
GS23b[d]		J033221.61-275623.7	5.5	J033221.58-275623.5	5.4	0.058	0.274	0.228	+0.19	**2.277**
GS24a	12.2	J033234.29-274941.1	8.7	J033234.26-274940.1	9.7	0.141[a]	0.649	0.571	+0.35	...
GS25a[d]	13.6	J033246.84-275121.0	6.8	J033246.82-275120.8	7.0	0.089	0.416	0.352	+0.33	**2.292**

(a) Radio sources identified with IRAC positions priors; (b) MIPS 24 μm flux and P-statistic determined from the FIDEL catalog; (c) IRAC fluxes and P-statistic determined from SIMPLE catalog; (d) robust identification based on AzTEC+LABOCA analysis.

Table 1 – *continued*

AzTEC ID	R_S ($''$)	radio coordinate (J2000)	Dist. ($''$)	*Spitzer* coordinate (J2000)	Dist. ($''$)	$P_{1.4}$	$P_{24\mu}$	P_{color}	[3.6]−[4.5] (mag)	$z_{\rm spec}$
GS26a	12.2	...	...	J033215.56-274335.5	5.5	...	...	0.237	+0.22	...
GS26b		...	...	J033216.41-274341.1	7.1	...	...	0.366	+0.25	2.331
GS26c		...	...	J033215.42-274339.7	7.2	...	...	0.372	+0.10	...
GS27a	13.0	J033242.09-274141.7	13.0	J033242.06-274141.3	13.6	0.291^a	0.870	0.807	+0.38	2.577
GS28a	13.0	...	...	J033242.78-275212.6	2.9	...	0.089	0.073	+0.55	...
GS28b		...	...	J033242.53-275216.9	4.4	...	...	0.136^c	+0.07	...
GS29a	13.0	...	...	**J033158.67-274500.2**	3.8	...	$\mathbf{0.050}^b$	...	-0.43	**0.577**
GS29b		...	...	J033159.30-274500.4	4.6	...	0.122^b	...	-0.10	2.340
GS30a	13.5	J033220.65-274235.3	6.5	J033220.66-274234.5	7.2	0.082^a	0.439	0.373	+0.19	...
GS30b		J033221.52-274242.5	9.0	J033221.48-274241.7	8.4	0.152^a	0.540	0.466	+0.26	...
GS30c		...	...	J033220.90-274236.9	4.4	...	...	0.160	+0.29	...
GS31a	13.6	**J033242.76-273927.4**	2.7	**J033242.81-273927.1**	2.1	$\mathbf{0.015}^a$	**0.046**	...	-0.25	**1.843**
GS31b		J033243.47-273929.3	7.9	J033243.49-273929.1	7.9	0.118^a	0.502	...	-0.36	0.733
GS32a	13.5	J033308.60-275134.8	9.6	J033308.61-275134.4	9.2	0.162	0.421^b	...	-0.42	0.734
GS32b		J033309.93-275131.4	10.5	J033309.88-275131.0	9.8	0.191	0.456^b	...	-0.12	...
GS32c		J033310.13-275125.1	13.4	J033310.12-275124.7	13.3	0.291	0.683^b	0.741^c	+0.08	...
GS33a	13.0	J033248.78-275314.8	7.4	J033248.78-275314.4	7.4	0.104^a	0.457	0.390	+0.34	...
GS34a	13.5	J033229.94-274301.6	11.5	J033229.95-274301.7	11.5	0.235^a	0.768	0.693	+0.09	1.356
GS34b		...	...	J033229.85-274317.7	5.8	...	0.311	...	-0.15	1.097
GS34c		...	...	J033229.74-274306.7	6.0	...	0.326	0.273	+0.14	...
GS34d		...	...	J033230.07-274306.8	7.9	...	...	0.430	+0.12	...
GS34e		...	...	J033229.47-274322.2	9.9	...	0.664	0.586	+0.15	1.609
GS35a	13.0	**J033227.21-274052.1**	2.0	**J033227.17-274051.7**	1.6	**0.008**	**0.027**	**0.022**	+0.37	...
GS35b		...	...	J033226.84-274056.1	4.9	...	...	0.191	+0.37	...
GS36a	13.5	...	...	J033214.42-275515.1	6.4	...	...	0.304	+0.68	...
GS37a	15.0	J033256.83-274627.8	13.3	J033256.79-274626.8	12.2	0.285^a	0.631^b	0.675^c	+0.08	...
GS37b		...	...	J033256.79-274612.1	4.3	...	...	0.132^c	+0.15	...
GS38a	13.5	J033209.71-274248.6	7.8	J033209.70-274248.2	7.5	0.116	0.463	...	-0.55	0.735
GS38b		...	...	J033208.74-274248.6	7.4	...	0.453	0.386	+0.15	...
GS39a[d]	15.0	J033154.44-274531.6	6.7	J033154.39-274530.3	7.9	0.083	...	0.379^c	+0.55	...
GS39b		...	...	J033154.54-274539.5	2.8	...	0.053^b	...	-0.10	...
GS40a	15.0	...	...	J033201.15-274635.9	10.2	...	0.479^b	...	-0.01	...
GS41a	6.7	J033302.78-275653.1	8.2	J033302.79-275652.8	8.0	0.120^a	...	0.386^c	+0.23	...
GS41b[d]		J033302.71-275642.5	8.6	J033302.68-275642.6	8.3	0.132	0.348^b	0.408^c	+0.30	...
GS41c		...	...	J033302.23-275651.4	2.7	...	...	0.053^c	+0.23	...
GS41d		...	...	J033302.55-275644.8	5.5	...	0.173^b	0.208^c	+0.15	...
GS42a[d]	6.9	...	...	J033314.16-275612.0	4.6	...	...	0.146^c	+0.04	...
GS43a[d]	8.6	...	...	J033302.90-274432.9	4.7	...	...	0.157^c	+0.23	...
GS44a	10.4	J033240.84-273752.3	9.3	J033240.84-273752.6	8.9	0.151	0.389^b	...	-0.07	...
GS45a	12.2	J033218.65-273743.3	12.1	J033218.58-273742.3	12.0	0.244^a	0.620^b	...	-0.32	...
GS45b		...	...	**J033219.09-273733.5**	0.9	...	$\mathbf{0.004}^b$	$\mathbf{0.006}^c$	+0.18	...
GS45c		...	...	**J033219.21-273731.5**	1.9	...	$\mathbf{0.016}^b$	$\mathbf{0.026}^c$	+0.21	...
GS45d		...	...	J033218.94-273730.0	4.3	...	...	0.129^c	+0.20	...
GS46a	13.0	...	...	J033157.27-275656.2	6.2	...	0.226^b	0.255^c	+0.17	...
GS47a[d]	12.2	J033208.27-275814.0	7.6	J033208.23-275813.9	7.8	0.105^a	0.280^b	0.371^c	+0.46	...

(Perera et al. 2008), using the updated positions and photometry for these sources presented in Downes et al. (2011). Chapin et al. (2009) reported one or more robust counterpart to 21 out of 29 AzTEC sources and at least one tentative counterpart for the remainder. Our analysis, employing slightly different criteria, identifies 16 robust counterpart sources and one or more tentative counterpart to all but two of the remaining sources. The agreement between Chapin et al. and our work is quite good, as 13 out of 16 robust counterparts we identified were also identified as robust counterparts by Chapin et al.

3 REDSHIFTS AND SPECTRAL ENERGY DISTRIBUTIONS

Spectroscopic redshifts, z_{spec}, are available for only a small subset ($\sim$ 30%) of candidate counterparts despite the extensive redshift surveys that have been conducted in the GOODS-South field over the years (Le Fevre et al. 2004; Szokoly et al. 2004; Mignoli et al. 2005; Vanzella et al. 2005, 2006; Norris et al. 2006; Kriek et al. 2008; Vanzella et al. 2008; Popesso et al. 2009; Treister et al. 2009; Wuyts et al. 2009; Balestra et al. 2010; Silverman et al. 2010; Casey et al. 2011). The primary reason for this is that many of the candidate counterparts are extremely faint in the optical, with a median brightness of $i \sim 25.4$ among those listed in Table 2 (also see Fig. 6).

Table 2. Photometry data listed in the same order as the identifications in Table 1. All upper-limits are given at a significance of 3-σ. De-boosted AzTEC 1.1 mm flux densities are taken from Downes et al. (2011). The LABOCA 870 μm photometry comes from Weiss et al. (2009).

AzTEC ID	1.4 GHz (μJy)	1.1 mm (mJy)	870 μm (mJy)	24 μm (μJy)	8 μm (μJy)	5.8 μm (μJy)	4.5 μm (μJy)	3.6 μm (μJy)	i (mag)	K (mag)
GS1a	32.0 ± 6.3	$6.7^{+0.6}_{-0.7}$	9.2 ± 1.2	122.0 ± 5.2	28.2 ± 0.7	20.0 ± 0.6	14.60 ± 0.09	10.39 ± 0.06	> 25.3	> 22.9
GS2.1a	50.7 ± 6.2	$6.4^{+0.7}_{-0.6}$	9.1 ± 1.2	148.0 ± 4.1	21.4 ± 0.5	14.0 ± 0.4	10.62 ± 0.06	7.50 ± 0.04	26.1	24.2
GS2.1b	44.1 ± 6.2	...	...	< 13.9	< 1.3	< 1.2	< 0.19	< 0.11	> 27.5	> 24.5
GS2.1c	< 18	...	...	16.0 ± 3.2	6.9 ± 0.5	7.8 ± 0.4	7.73 ± 0.06	10.36 ± 0.04	22.1	21.8
GS2.2a	< 18	$4.0^{+0.6}_{-0.7}$	...	62.9 ± 3.9	16.2 ± 0.5	15.6 ± 0.4	17.98 ± 0.07	22.28 ± 0.04	22.9	21.1
GS2.2b	< 18	...	...	83.2 ± 4.2	23.8 ± 0.5	24.8 ± 0.4	20.46 ± 0.07	16.10 ± 0.04	26.4	23.3
GS2.2c	< 18	...	...	< 12.8	14.3 ± 0.5	19.9 ± 0.4	16.75 ± 0.07	15.30 ± 0.04	26.6	21.3
GS3a	40.7 ± 6.5	$4.8^{+0.6}_{-0.5}$	8.8 ± 1.2	49.2 ± 2.8	13.0 ± 0.5	8.7 ± 0.4	6.17 ± 0.06	4.38 ± 0.04	> 25.3	> 22.9
GS3b	< 19	...	...	< 12.6	3.1 ± 0.5	4.2 ± 0.4	3.13 ± 0.07	2.76 ± 0.04	> 25.3	> 22.9
GS4a	25.4 ± 6.5	$5.1^{+0.6}_{-0.6}$	8.8 ± 1.2	< 16.7	18.6 ± 0.9	13.6 ± 0.7	9.32 ± 0.13	7.21 ± 0.06	26.8	> 24.5
GS5a	96.4 ± 6.7	$4.8^{+0.6}_{-0.7}$	3.9 ± 1.4	521.7 ± 10.9	58.2 ± 0.9	62.6 ± 0.9	73.70 ± 0.18	59.67 ± 0.11	23.1	20.7
GS5b	111.7 ± 6.7	...	...	282.3 ± 7.7	16.1 ± 0.9	17.9 ± 0.9	14.12 ± 0.18	9.50 ± 0.11	25.7	22.6
GS6a	31.0 ± 6.3	$3.6^{+0.5}_{-0.6}$	5.8 ± 1.4	141.0 ± 4.0	27.4 ± 0.5	25.6 ± 0.4	17.70 ± 0.06	11.72 ± 0.04	28.3	22.8
GS6b	< 18	...	...	94.2 ± 3.7	11.4 ± 0.5	12.1 ± 0.4	17.00 ± 0.06	21.09 ± 0.04	23.5	21.1
GS7a	51.2 ± 6.4	$3.8^{+0.6}_{-0.7}$	9.1 ± 1.2	103.0 ± 9.3	22.4 ± 0.6	17.7 ± 0.6	12.03 ± 0.12	7.89 ± 0.08	> 25.3	> 22.9
GS7b	< 19	...	...	60.0 ± 9.5	5.0 ± 0.9	7.6 ± 0.7	9.33 ± 0.23	9.03 ± 0.09	24.2	> 22.9
GS8a	71.4 ± 6.6	$3.4^{+0.6}_{-0.6}$	7.5 ± 1.2	620.0 ± 6.5	42.9 ± 0.7	62.6 ± 0.6	50.07 ± 0.10	36.85 ± 0.06	24.7	21.6
GS8b	< 19	...	...	164.0 ± 4.8	27.5 ± 0.6	20.6 ± 0.5	15.73 ± 0.09	13.44 ± 0.05	26.6	> 22.9
GS9a	86.8 ± 6.6	$3.6^{+0.6}_{-0.6}$	...	228.9 ± 10.3	27.3 ± 0.9	14.9 ± 0.9	12.37 ± 0.17	7.69 ± 0.13	25.3	> 22.9
GS9b	< 19	...	...	117.4 ± 9.7	3.8 ± 0.9	6.3 ± 0.9	7.27 ± 0.17	5.58 ± 0.12	> 27.5	22.6
GS9c	< 19	...	...	< 23.1	8.7 ± 0.9	8.0 ± 0.9	8.06 ± 0.17	5.99 ± 0.13	> 25.3	> 22.9
GS10a	89.3 ± 6.4	$3.8^{+0.7}_{-0.7}$	7.6 ± 1.3	214.0 ± 8.4	32.0 ± 0.7	40.5 ± 0.9	47.03 ± 0.22	41.21 ± 0.15	23.6	21.3
GS10b	< 19	...	...	< 22.7	4.8 ± 1.0	6.9 ± 1.2	5.73 ± 0.22	5.52 ± 0.15	26.8	> 22.9
GS11a	46.0 ± 6.4	$3.3^{+0.6}_{-0.6}$	...	117.0 ± 4.5	32.5 ± 0.4	23.8 ± 0.3	22.45 ± 0.05	22.89 ± 0.04	> 25.3	> 22.9
GS12a	21.0 ± 6.5	$3.1^{+0.6}_{-0.6}$	5.1 ± 1.4	31.6 ± 5.1	12.2 ± 0.5	7.2 ± 0.5	3.89 ± 0.07	3.54 ± 0.04	25.2	> 22.9
GS13a	22.8 ± 6.3	$3.1^{+0.6}_{-0.6}$	...	34.7 ± 3.6	6.2 ± 0.5	6.0 ± 0.4	5.32 ± 0.07	4.24 ± 0.04	26.8	22.5
GS13b	24.0 ± 6.3	...	...	112.0 ± 3.8	13.8 ± 0.5	14.5 ± 0.4	14.03 ± 0.07	13.72 ± 0.04	23.2	22.0
GS13c	23.7 ± 6.3	...	...	224.0 ± 3.7	31.9 ± 0.5	33.1 ± 0.4	42.70 ± 0.07	53.65 ± 0.05	22.5	20.2
GS14a	< 18	$2.9^{+0.6}_{-0.5}$	3.3 ± 1.2	< 12.8	< 1.3	< 1.2	1.24 ± 0.06	1.19 ± 0.04	25.2	23.9
GS15a	27.6 ± 6.5	$3.9^{+0.7}_{-0.8}$	4.2 ± 1.4	< 24.2	16.0 ± 1.0	13.2 ± 0.9	9.29 ± 0.18	6.17 ± 0.12	> 25.3	> 22.9
GS15b	< 19	...	...	< 24.6	5.8 ± 1.0	5.7 ± 0.9	5.71 ± 0.18	5.47 ± 0.12	> 25.3	> 22.9
GS15c	< 19	...	...	< 25.0	< 2.9	< 2.6	1.12 ± 0.18	1.12 ± 0.12	> 25.3	> 22.9
GS16a	30.7 ± 6.4	$2.7^{+0.5}_{-0.6}$	...	46.4 ± 3.3	16.4 ± 0.5	10.9 ± 0.4	8.12 ± 0.07	4.98 ± 0.04	26.5	25.8
GS16b	22.1 ± 6.4	...	...	144.0 ± 3.5	15.7 ± 0.5	15.9 ± 0.4	21.74 ± 0.07	28.44 ± 0.04	23.0	20.6
GS17a	26.1 ± 6.3	$2.9^{+0.6}_{-0.6}$	...	71.3 ± 9.6	5.1 ± 0.4	4.6 ± 0.3	4.21 ± 0.05	5.42 ± 0.03	23.6	22.6
GS17b	< 18	...	...	61.9 ± 7.2	21.2 ± 0.4	26.3 ± 0.3	20.19 ± 0.05	16.94 ± 0.03	26.0	22.8
GS17c	< 18	...	...	200.0 ± 5.3	20.9 ± 0.4	23.9 ± 0.3	16.50 ± 0.05	11.79 ± 0.03	26.7	22.7
GS17d	42.1 ± 6.2	...	...	< 12.3	11.3 ± 0.4	12.0 ± 0.3	9.07 ± 0.05	7.37 ± 0.03	25.2	23.6
GS17e	37.9 ± 6.2	...	...	23.5 ± 4.1	9.7 ± 0.4	7.1 ± 0.3	5.23 ± 0.05	3.88 ± 0.03	27.6	23.5
GS18a	25.1 ± 6.3	$3.1^{+0.6}_{-0.6}$	6.4 ± 1.3	84.6 ± 2.9	13.1 ± 0.4	11.7 ± 0.3	7.56 ± 0.05	4.91 ± 0.03	28.1	> 24.5
GS18b	20.2 ± 6.3	...	...	126.0 ± 4.0	22.2 ± 0.4	16.0 ± 0.3	10.85 ± 0.05	8.19 ± 0.03	24.5	23.2
GS18c	< 18	...	...	91.4 ± 2.8	11.2 ± 0.4	12.6 ± 0.3	11.84 ± 0.05	16.97 ± 0.03	22.8	20.8
GS19a	34.0 ± 6.5	$2.6^{+0.5}_{-0.6}$	...	317 ± 17	18.9 ± 0.5	25.8 ± 0.4	22.97 ± 0.07	18.74 ± 0.04	24.2	21.7
GS19b	40.0 ± 6.5	...	...	149 ± 17	15.9 ± 0.5	22.7 ± 0.4	17.67 ± 0.07	12.72 ± 0.04	26.6	21.7
GS19c	< 19	...	...	105.1 ± 10.7	9.1 ± 0.3	12.3 ± 0.3	11.61 ± 0.06	9.97 ± 0.04	26.9	21.6
GS20a	793 ± 99	$2.7^{+0.6}_{-0.6}$	...	4030.0 ± 44.1	3499.5 ± 0.6	1113.8 ± 0.6	759.28 ± 0.11	1131.36 ± 0.16	16.1	15.0
GS21a	43.6 ± 6.3	$2.7^{+0.6}_{-0.7}$	...	299.0 ± 4.0	16.6 ± 0.5	24.0 ± 0.4	19.97 ± 0.08	15.98 ± 0.04	25.3	22.5
GS21b	< 18	...	...	27.8 ± 2.6	4.8 ± 0.5	6.9 ± 0.4	8.44 ± 0.08	7.51 ± 0.04	25.9	> 24.5
GS22a	34.6 ± 6.5	$2.1^{+0.6}_{-0.6}$	...	290.0 ± 4.4	13.7 ± 0.5	15.3 ± 0.4	13.23 ± 0.07	10.02 ± 0.04	26.4	21.5
GS22b	< 19	...	...	< 11.4	< 1.4	2.7 ± 0.4	2.55 ± 0.07	2.26 ± 0.04	25.9	22.8
GS23a	23.4 ± 6.5	$2.3^{+0.6}_{-0.6}$	...	42.4 ± 5.9	19.7 ± 0.5	18.9 ± 0.5	12.19 ± 0.07	8.06 ± 0.05	24.5	> 22.9
GS23b	35.2 ± 6.5	...	4.7 ± 1.4	586.0 ± 6.2	36.4 ± 0.5	47.1 ± 0.5	46.86 ± 0.07	39.37 ± 0.05	24.0	21.2
GS24a	18.5 ± 6.1	$2.3^{+0.6}_{-0.6}$	...	90.8 ± 3.8	16.4 ± 0.4	9.8 ± 0.3	6.61 ± 0.05	4.79 ± 0.03	25.5	24.1
GS25a	89.5 ± 6.2	$1.9^{+0.5}_{-0.6}$	5.9 ± 1.3	140.0 ± 3.6	32.2 ± 0.5	24.5 ± 0.4	18.81 ± 0.06	13.88 ± 0.04	23.9	22.6

Table 2 – *continued*

AzTEC ID	1.4 GHz (μJy)	1.1 mm (mJy)	870 μm (mJy)	24 μm (μJy)	8 μm (μJy)	5.8 μm (μJy)	4.5 μm (μJy)	3.6 μm (μJy)	i (mag)	K (mag)
GS26a	< 18	$2.2^{+0.5}_{-0.6}$	...	< 11.3	2.4 ± 0.5	2.7 ± 0.4	3.64 ± 0.07	2.98 ± 0.04	25.2	24.6
GS26b	< 18	...	...	< 12.1	9.0 ± 0.5	7.1 ± 0.4	6.71 ± 0.07	5.35 ± 0.04	24.9	23.3
GS26c	< 18	...	...	< 11.0	11.5 ± 0.5	18.5 ± 0.4	23.55 ± 0.07	21.52 ± 0.04	25.9	21.3
GS27a	23.6 ± 6.5	$2.2^{+0.6}_{-0.6}$	...	171.0 ± 5.6	25.3 ± 0.5	23.7 ± 0.5	16.57 ± 0.07	11.67 ± 0.04	24.8	24.2
GS28a	< 18	$2.1^{+0.6}_{-0.5}$	...	17.3 ± 2.6	10.8 ± 0.5	6.9 ± 0.4	4.33 ± 0.06	2.62 ± 0.04	26.5	23.6
GS28b	< 18	...	...	< 26.4	< 1.0	< 1.0	1.12 ± 0.06	1.05 ± 0.04	26.0	24.6
GS29a	< 19	$2.3^{+0.6}_{-0.6}$	...	54.4 ± 10.7	15.3 ± 1.0	27.4 ± 0.9	32.93 ± 0.20	49.07 ± 0.13	20.4	19.8
GS29b	< 19	...	...	47.4 ± 10.1	5.2 ± 1.0	6.2 ± 1.0	5.51 ± 0.19	6.04 ± 0.13	23.8	22.5
GS30a	37.2 ± 6.2	$1.8^{+0.5}_{-0.6}$	...	459.0 ± 6.2	25.9 ± 0.5	35.4 ± 0.4	32.99 ± 0.07	27.57 ± 0.04	24.6	21.0
GS30b	24.2 ± 6.2	...	...	316.0 ± 4.2	27.6 ± 0.5	33.7 ± 0.4	34.14 ± 0.07	26.96 ± 0.04	26.3	21.2
GS30c	< 18	...	...	< 10.5	2.4 ± 0.5	2.7 ± 0.4	2.20 ± 0.07	1.69 ± 0.04	25.7	24.2
GS31a	25.1 ± 6.9	$2.2^{+0.7}_{-0.7}$	...	427.0 ± 5.6	31.5 ± 0.7	49.3 ± 0.7	51.71 ± 0.11	64.98 ± 0.07	21.6	19.8
GS31b	37.5 ± 6.9	...	...	521.0 ± 6.7	60.0 ± 0.8	75.4 ± 0.7	70.27 ± 0.11	97.45 ± 0.07	22.5	19.6
GS32a	30.3 ± 6.8	$2.3^{+0.8}_{-0.8}$	...	371.1 ± 11.7	32.4 ± 0.9	47.0 ± 0.9	45.47 ± 0.17	67.02 ± 0.12	21.6	19.8
GS32b	34.8 ± 6.9	...	...	265.6 ± 11.9	32.8 ± 0.9	35.8 ± 0.9	57.75 ± 0.17	64.39 ± 0.13	22.4	20.2
GS32c	46.3 ± 6.9	...	...	270.4 ± 12.2	12.4 ± 0.9	12.2 ± 0.9	11.06 ± 0.17	10.27 ± 0.13	25.4	> 22.9
GS33a	28.6 ± 6.2	$2.0^{+0.5}_{-0.6}$	...	16.1 ± 3.7	5.1 ± 0.5	2.4 ± 0.4	1.70 ± 0.07	1.24 ± 0.04	26.9	24.1
GS34a	33.0 ± 6.3	$1.7^{+0.5}_{-0.6}$	...	173.0 ± 3.3	32.9 ± 0.5	28.8 ± 0.4	35.68 ± 0.07	32.72 ± 0.05	23.4	20.9
GS34b	< 19	...	...	41.4 ± 3.7	14.3 ± 0.5	16.7 ± 0.4	20.34 ± 0.07	23.42 ± 0.04	23.5	21.2
GS34c	< 18	...	...	56.8 ± 3.3	5.8 ± 0.5	8.1 ± 0.4	10.08 ± 0.07	8.83 ± 0.04	25.6	22.3
GS34d	< 19	...	...	< 10.5	3.5 ± 0.5	4.7 ± 0.4	4.54 ± 0.07	4.05 ± 0.04	24.3	23.4
GS34e	< 19	...	...	70.1 ± 3.2	14.9 ± 0.5	17.2 ± 0.4	19.86 ± 0.07	17.31 ± 0.04	24.4	22.1
GS35a	41.3 ± 6.7	$2.1^{+0.6}_{-0.6}$	...	153.0 ± 3.8	22.2 ± 0.5	19.8 ± 0.4	14.72 ± 0.07	10.51 ± 0.04	24.7	23.1
GS35b	< 19	...	...	< 12.9	2.4 ± 0.5	3.1 ± 0.4	2.76 ± 0.07	1.96 ± 0.04	25.3	23.5
GS36a	< 19	$2.0^{+0.6}_{-0.6}$	...	< 17.4	7.6 ± 0.7	5.2 ± 0.6	2.84 ± 0.10	1.52 ± 0.06	> 25.3	> 22.9
GS37a	20.5 ± 6.4	$2.1^{+0.8}_{-0.8}$	...	112.9 ± 7.0	17.1 ± 1.0	16.1 ± 1.0	15.08 ± 0.20	13.95 ± 0.13	25.4	> 22.9
GS37b	< 19	...	...	< 21.5	< 3.0	3.6 ± 1.0	2.89 ± 0.19	2.52 ± 0.13	25.9	> 22.9
GS38a	220.0 ± 6.5	$1.7^{+0.6}_{-0.6}$	...	39.2 ± 2.6	34.2 ± 0.5	58.1 ± 0.4	67.61 ± 0.08	112.41 ± 0.06	21.1	18.8
GS38b	< 19	...	...	184.0 ± 4.9	15.8 ± 0.5	21.2 ± 0.4	16.86 ± 0.07	14.66 ± 0.04	> 25.3	> 22.9
GS39a	37.2 ± 6.6	$1.5^{+0.7}_{-0.7}$	3.8 ± 1.4	< 26.9	8.4 ± 1.0	6.7 ± 0.9	4.91 ± 0.19	2.96 ± 0.12	> 25.3	> 22.9
GS39b	< 19	...	...	48.4 ± 7.4	5.9 ± 1.0	8.5 ± 0.9	9.17 ± 0.18	10.04 ± 0.12	23.1	22.3
GS40a	< 19	$1.8^{+0.6}_{-0.7}$	...	169.6 ± 8.3	7.9 ± 1.0	13.7 ± 1.1	13.45 ± 0.20	13.64 ± 0.13	25.1	22.0
GS41a	28.2 ± 7.0	$7.2^{+0.9}_{-1.0}$	...	< 22.4	4.9 ± 0.9	6.5 ± 0.9	4.35 ± 0.17	3.52 ± 0.12	> 25.3	23.3
GS41b	223.0 ± 7.0	...	12.0 ± 1.2	62.0 ± 6.0	4.7 ± 2.4	6.6 ± 2.6	5.35 ± 0.46	4.06 ± 0.34	> 25.3	> 22.9
GS41c	< 21	...	...	< 23.9	< 2.7	< 2.8	1.71 ± 0.12	1.39 ± 0.12	> 25.3	> 22.9
GS41d	< 20	...	...	212.2 ± 6.8	17.1 ± 0.9	19.9 ± 0.9	18.94 ± 0.17	16.55 ± 0.12	24.3	22.0
GS42a	< 21	$9.2^{+1.2}_{-1.4}$	14.5 ± 1.2	< 26.6	5.7 ± 0.9	< 2.7	2.50 ± 0.18	2.40 ± 0.13	25.4	> 22.9
GS43a	< 20	$6.1^{+1.0}_{-1.1}$	6.7 ± 1.3	< 25.6	4.0 ± 0.9	< 2.7	1.26 ± 0.16	1.02 ± 0.12	> 25.3	> 22.9
GS44a	43.5 ± 7.3	$3.2^{+0.8}_{-0.8}$	$^{\dagger}5.0 \pm 1.4$	143.1 ± 9.3	19.4 ± 1.0	17.9 ± 1.0	27.54 ± 0.19	29.39 ± 0.14	23.7	21.5
GS45a	33.7 ± 6.9	$4.0^{+1.2}_{-1.1}$	8.1 ± 1.2	446.3 ± 9.4	91.9 ± 1.1	106.6 ± 1.1	140.28 ± 0.21	188.72 ± 0.15	18.6	17.8
GS45b	< 20	...	...	64.4 ± 9.3	4.3 ± 1.1	5.9 ± 1.1	5.02 ± 0.21	4.24 ± 0.15	> 25.3	> 22.9
GS45c	< 20	...	...	48.9 ± 9.2	7.3 ± 1.1	5.8 ± 1.1	5.33 ± 0.22	4.41 ± 0.15	26.4	> 22.9
GS45d	< 20	...	...	< 37.7	3.8 ± 1.1	< 3.3	2.11 ± 0.22	1.75 ± 0.14	> 25.3	> 22.9
GS46a	< 21	$4.8^{+1.4}_{-1.7}$	$^{\dagger}4.8 \pm 1.4$	74.6 ± 9.6	6.7 ± 0.8	9.0 ± 0.9	10.54 ± 0.16	9.01 ± 0.11	25.1	> 22.9
GS47a	43.2 ± 7.0	$3.5^{+1.0}_{-1.0}$	7.3 ± 1.2	72.3 ± 10.6	9.7 ± 1.0	9.6 ± 0.9	6.88 ± 0.18	4.51 ± 0.12	> 25.3	> 22.9

† The AzTEC and LABOCA centroid positions are offset by a significant amount ($\gtrsim 10''$).

Robustly identified AzTEC counterparts are even fainter as discussed below.

To learn more about the redshift distribution of these AzTEC sources and their nature, we rely on the extensive database of extremely deep, multi-wavelength broad-band photometry to analyze their SEDs using empirical and theoretical models. We first examine the optical/near-IR photometry data using standard methods for estimating photometric redshift ("photoz" hereafter), stellar mass (M_*), and star formation rate (SFR_{UV}). We also employ an independent analysis of the IR-to-radio SEDs to derive photometric redshift, IR luminosity, and dust-obscured star formation rate (SFR_{IR}).

3.1 Optical/Near-IR SED Analysis

The photometric redshift of each galaxy is computed by fitting the observed optical and near-IR spectral energy distribution of the galaxies to stellar population synthesis models drawn from the PEGASE 2.0[6] library

---

[6] http://www2.iap.fr/pegase/
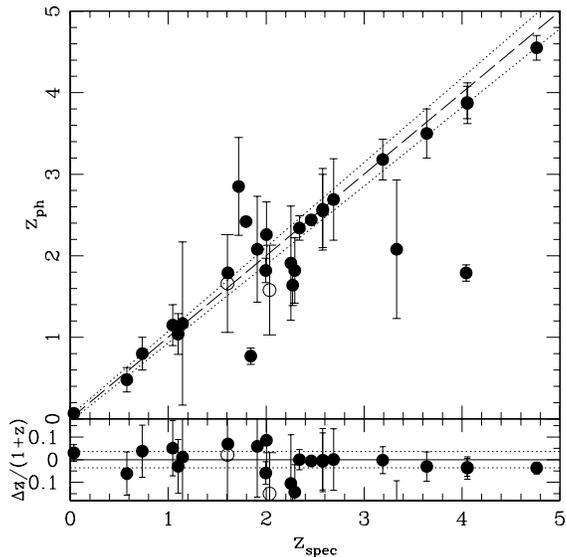
Figure 2. Comparison of spectroscopic and photometric redshifts for the candidate AzTEC counterpart sources in the GOODS-South (Table 1) field. Photometric redshifts based on the shallower MUSYC photometry (Gawiser et al. 2006) are shown in empty symbols. The two dotted curves represent redshift uncertainties of $\Delta z/(1+z) = 0.036$ (see the text). The distribution of $\Delta z/(1+z)$ is shown as a function of z in the bottom panel.

(Fioc & Rocca-Volmerange 1997). The models are shifted in the redshift range of $0 < z < 7$ with a step size of $\Delta z = 0.01$. For each galaxy, the weighted average photoz is derived as:

$$z_{photo} = \frac{\int z P(z) dz}{\int P(z) dz}, \qquad (1)$$

where $P(z)$ is the probability distribution function of redshift $P(z) \propto exp(-\chi^2(z))$. To evaluate the reliability of our photoz measurements, we compare the photozs with spectroscopic redshifts (specz) of GOODS galaxies with reliable emission line redshifts in Figure 2. We find that the relative error (defined as $(z_{phot} - z_{spec})/(1 + z_{spec})$) has a zero mean (0.0005) and a very small deviation of 0.036 after 3σ clipping of the outliers. The fraction of outliers beyond 3σ is 9.9%. The means of the relative errors have no significant offset from zero at all redshift bins, especially for our interested range of $1 < z < 5$. The demonstrated accuracy of our photoz estimation is sufficient to justify a statistical study of the physical properties of our selected galaxies. Derived photometric redshifts of the AzTEC counterpart candidates are listed as z_{opt} in Table 3. A blank entry notes that the optical counterpart is undetected or too faint.

Physical properties (stellar mass, SFR, dust reddening) of the galaxies are measured by fitting the observed SEDs with the CB09 (Charlot & Bruzual, in prep.) theoretical stellar population synthesis models. The Salpeter IMF with a lower and an upper mass cutoff of $0.1 M_\odot$ and $100 M_\odot$ are adopted.[7] The galaxy redshift is fixed to its z_{spec} or z_{opt} in this step. A regular grid of models spanning a wide range of $E(B - V)$, star formation history (characterized

by duration τ and age), and metallicity are examined. We apply the Calzetti law (Calzetti et al. 2000) for the internal dust extinction correction and follow the method described by Madau (1995) to account for the IGM opacity. The χ^2 value for each SED model fitting is computed as

$$\chi^2 = \Sigma_i \frac{(F_{obs,i} - \alpha F_{model,i})^2}{\sigma_i^2}, \qquad (2)$$

where $F_{obs,i}$, $F_{model,i}$, and σ_i are the observed flux, model flux, and observational uncertainty in the ith band. The normalization factor α is equal to stellar mass if $F_{model,i}$ is normalized to $1 M_\odot$ in our pre-computed database. The model with the smallest χ^2 is considered the best-fit model, and its parameters are used to compute the stellar mass and star formation rate SFR_{UV} – see Table 3.

We estimate the systematic uncertainties in the derived quantities using simulations. We generate theoretical SED templates with different redshift, stellar mass, SFR, age, and dust extinction. In each band, we randomly draw a photometric uncertainty from the error distribution of all sources with the same magnitude from the GOODS parent photometric catalog and perturb the photometry of the template using a Gaussian random deviation with variance equal to the drawn photometric uncertainty. These steps are repeated 100 times for each template in each band to generate mock SEDs. Our SED-fitting code is applied to these mock SEDs to derive the systematic uncertainties in the derived quantities. If redshift and IMF are known, a typical uncertainty in stellar mass from the SED-fitting is about 0.1-0.2 dex for all stellar masses. The uncertainty in SFR is about 0.1 dex for $SFR > 100 M_\odot$ yr^{-1}. If a photoz is used, a typical redshift error of $\delta z/(1 + z) = 0.05$ translates to a 0.2 dex error in M_* and SFR. Excluding the uncertainty in the IMF, the overall typical uncertainties in M_* and SFR are 0.3 dex and 0.5 dex, respectively.

3.2 IR/mm/radio SED Analysis

We derive an independent estimate of photometric redshift, IR luminosity, and dust-obscured star formation rate (SFR_{IR}) by analyzing the observed IR/mm/radio part of the SED. First, a photometric redshift is derived using an updated version of the photoz analysis method described by Carilli & Yun (1999). Noting a remarkably tight correlation between radio and far-IR luminosity for all star forming galaxies (see review by Condon 1992) and the rapid change in the observed flux density ratio between the 850 μm band and the 20 cm radio continuum with redshift, Carilli & Yun (1999) proposed this observed flux density ratio as a robust redshift indicator. The success of this method rests on the fact that the Rayleigh-Jeans (R-J) part of the dust spectrum rises rapidly with frequency as $S \propto \nu^{3-4}$ while the radio part of the spectrum falls as $S \propto \nu^{-0.75}$, leading to more than two orders of magnitudes change in the observed flux density ratio between $z = 0$ and $z \geqslant 2$.

Subsequent analysis by Hughes et al. (2002) and Aretxaga et al. (2003) have shown that incorporating additional photometric measurements in the far-IR to radio bands can improve the redshift estimate, but all of these methods are fundamentally limited by the intrinsic variation in the SED, arising from variations in the nature of the energy source and geometry of dust distribution. To improve

---

[7] Adopting the Chabrier or Krupa IMF will lower the derived M_* and SFR by a factor of 1.7 – see Salimbeni et al. (2009).

Table 3. Redshifts and derived properties of the AzTEC GOODS-South sources.

AzTEC ID	z_{spec}^a	z_{opt}^b	log M_* ($M_\odot$)	SFR_{UV} ($M_\odot$/yr)	z_{MR}^c	SFR_{IR} ($M_\odot$/yr)
GS1a	...	2.96 ± 0.45	11.24	94	$3.56^{+0.66}_{-1.20}$	439
GS2.1a	...	2.13 ± 0.60	9.81	234	$3.20^{+0.60}_{-1.10}$	500
GS3a	...	...	...	...	$3.09^{+0.55}_{-1.11}$	
GS4a	...	3.37 ± 0.25	10.87	75	$3.53^{+0.57}_{-1.27}$	416
GS5a	1.599	1.66 ± 0.60	11.15	1632	$2.03^{+0.37}_{-0.73}$	646
GS6a	...	2.47 ± 0.65	11.37	37	$2.78^{+0.60}_{-0.98}$	220
GS7a	2.676	...	...	...	$2.56^{+0.52}_{-0.92}$	638
GS8a	2.252	1.91 ± 0.70	11.04	1553	$2.11^{+0.41}_{-0.73}$	466
GS9a	...	3.49 ± 0.35	11.01	285	$1.98^{+0.38}_{-0.74}$	
GS10a	2.035	1.58 ± 0.55	11.27	1555	$2.03^{+0.41}_{-0.75}$	350
GS11a	...	...	...	...	$2.50^{+0.52}_{-0.88}$	
GS12a	4.762	4.55 ± 0.15	11.28	87	$3.28^{+0.70}_{-1.26}$	803
GS13a	...	2.28 ± 0.90	10.20	3172	$2.92^{+0.58}_{-1.10}$	250
GS14a	3.640	3.50 ± 0.30	9.36	459	> 3.0	600
GS15a	...	3.01 ± 0.45	10.00	1024	$3.23^{+0.67}_{-1.13}$	416
GS16a	1.719	2.85 ± 0.60	9.33	114	$2.67^{+0.55}_{-0.95}$	200
GS17a	...	1.01 ± 0.10	9.67	3.4	$2.94^{+0.44}_{-1.08}$	
GS17b	...	3.11 ± 0.20	11.41	14	> 3.1	330
GS18a	...	...	...	...	$3.00^{+0.56}_{-1.14}$	
GS19a	...	1.83 ± 0.35	10.93	99	$2.74^{+0.52}_{-1.04}$	200
GS20a	0.037	0.069 ± 0.038	9.52	339	$0.57^{+0.17}_{-0.41}$	0.9
GS21a	1.910	2.08 ± 0.65	10.77	295	$2.28^{+0.40}_{-0.90}$	322
GS22a	1.794	2.42 ± 0.05	...	...	$2.39^{+0.51}_{-0.93}$	204
GS23a	...	...	...	...	$2.77^{+0.47}_{-1.07}$	
GS23b	2.277	1.64 ± 0.25	11.35	33	$2.36^{+0.44}_{-0.90}$	393
GS24a	...	1.94 ± 0.50	9.37	130	$3.04^{+0.74}_{-1.10}$	200
GS25a	2.292	1.82 ± 0.40	10.11	467	$1.52^{+0.32}_{-0.68}$	300
GS26a	...	3.64 ± 0.15	9.61	47	> 2.6	150
GS27a	2.577	2.55 ± 0.45	10.02	383	$2.47^{+0.57}_{-0.99}$	322
GS28a	...	3.29 ± 0.65	9.95	1140	> 2.6	177
GS29a	0.577	0.48 ± 0.15	10.45	4.0	> 2.6	
GS29b	2.340	2.34 ± 0.15	10.36	75	> 2.6	200
GS30a	...	1.51 ± 0.25	11.02	6.0	$2.29^{+0.56}_{-0.88}$	182
GS31a	1.843	0.77 ± 0.10	11.96	0.3	$2.68^{+0.66}_{-1.00}$	222
GS33a	...	2.45 ± 0.15	10.08	6.0	$2.46^{+0.60}_{-0.96}$	200
GS35a	...	2.96 ± 0.35	10.74	127	$2.27^{+0.53}_{-0.91}$	508
GS37c	...	...	...	...	> 2.6	
GS39a	...	...	...	...	$2.01^{+0.51}_{-0.85}$	
GS42a	...	2.37 ± 0.15	9.56	4.1	> 4.5	
GS43a	...	...	...	...	> 4.0	
GS45b	...	2.07 ± 0.25	10.20	12	> 3.4	
GS45c	...	2.91 ± 0.35	10.46	156	> 3.4	
GS46a	...	1.67 ± 0.10	10.47	11	> 3.5	
GS47a	...	...	...	...	$2.59^{+0.55}_{-0.95}$	

(a) z_{spec} is a spectroscopic redshift. See § A for the individual references; (b) z_{opt}^a is a photometric redshift derived from the analysis of the optical/NIR SED – see § 3.1; and (c) z_{rm} is a new photometric redshift derived from the radio and AzTEC 1100 μm photometry – see § 3.2. The listed uncertainty corresponds to a redshift range that includes 68% of acceptable fits.

the accuracy of the derived redshift and its uncertainty, we adopted a three times larger set of SED templates, adding 34 new sources with two or more photometry measurements in the R-J part ($150\mu < \lambda < 1500\mu$) of the dust SED and at least one radio continuum measurement, mostly from the new study by Clements et al. (2010). We opted to use empirical templates of observed SEDs rather than a library of theoretical templates because there is growing evidence, such as the tightness of the radio-IR correlation, suggesting that nature favors a certain subset of SEDs.

Another important addition is the use of Monte Carlo simulations to improve the handling of measurement errors, noise bias, and the template variations. A notable outcome is that the derived redshift uncertainties, listed in Table 3, are asymmetric about the mean millimeter-to-radio photometric redshift (z_{MR}). Citing the flattening of the IR part of the SED with increasing redshift, Carilli & Yun (2000) have previously noted the asymmetry in the scatter of the "mean galaxy model", but *in the opposite sense* from the uncertainties in the derived z_{MR}. This actually makes sense
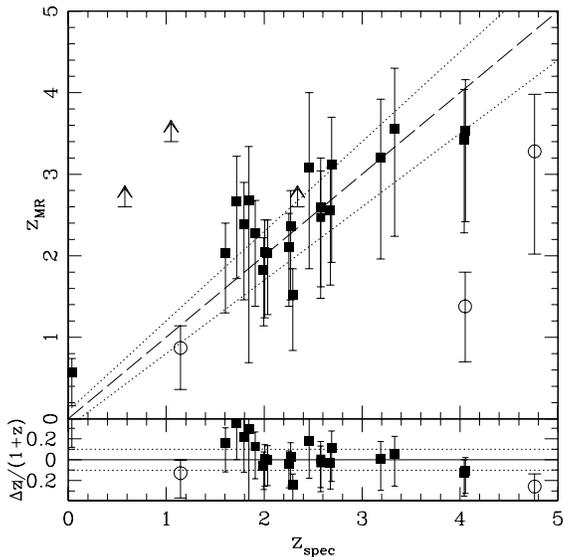
Figure 3. Comparison of spectroscopic and millimeter-to-radio (MR) photometric redshifts for the AzTEC sources with a robust counterpart in the GOODS-South (Table 1) and GOODS-North (Chapin et al. 2009) fields. Three objects with clear evidence for AGN activity are identified as empty circles. The two dotted curves represent redshift uncertainties of $\Delta z/(1+z) = 0.10$. The distribution of $\Delta z/(1+z)$ is shown as a function of z in the bottom panel.

since the asymmetry in the mean template and the uncertainty in the derived z_{MR} should be in the opposite sense. This comparison thus shows that the common practice of quoting the redshift uncertainty using the (sub)mm-radio spectral index method based on the scatter in the Carilli & Yun template (e.g., Aretxaga et al. 2007; Dannerbauer et al. 2008; Chapin et al. 2009) is in error.

The derived z_{MR} is in good agreement with z_{spec} in most cases as shown in Figure 3 with $\Delta z/(1+z) \sim 0.1$. This is not surprising given that the well-know radio-FIR correlation appears to hold among high-redshift IR-selected galaxies (see Ivison et al. 2010; Lacki & Thompson 2010). This estimator may be more accurate for starburst-dominated SMGs since two outliers at $z = 4.05$ and $z = 4.76$ are known AGNs, and a similar "radio-excess" due to an AGN contribution in the radio wavelength has been previously seen among other high redshift QSOs (Yun et al. 2002; Yun & Carilli 2002). In some cases (e.g., GS2.2a, GS29a) the derived z_{MR} is completely inconsistent with their z_{spec}, primarily because of their radio non-detection. Given that the radio-FIR correlation holds for all other objects, a likely explanation is that their optical counterparts are mis-identified, as is expected to happen in a small fraction ($\leqslant 5\%$) of cases (see § 2.1).

Once the redshift of an AzTEC counterpart is determined, its IR luminosity L_{IR} can be estimated by adopting an SED template most consistent with the observed FIR/mm/radio photometry data. For the ease of a direct comparison with optically derived SFR_{UV}, we fix the redshift of each source to z_{spec} or z_{opt}. Then we use this L_{IR} to derive a dust-obscured star formation rate (SFR_{IR} – e.g., Kennicutt 1998). We adopt a set of theoretical SED templates for an ensemble of GMCs centrally illuminated by young star clusters by Efstathiou et al.

(2000) that are shown to provide a good fit to a wide range of IR-selected sources at different redshifts (e.g., Efstathiou & Rowan-Robinson 2003; Clements et al. 2008; Rowan-Robinson 2010). Star formation rates derived from the IR SED fitting, SFR_{IR}, are computed directly from the best-fit model star formation history (also assuming the Salpeter IMF) and are summarized in the last column of Table 3. Note that z_{opt} and z_{MR} do not always agree well, particularly for the cases where the counterpart is not secure. Therefore SFR_{IR} is derived primarily for the securely identified AzTEC sources with a z_{spec} or a well-determined z_{opt} only.

4   REDSHIFT DISTRIBUTION OF AZTEC-GOODS SOURCES

4.1   Derived redshift distribution

The deep multiwavelength data and the extensive spectroscopic redshift surveys covering the two GOODS fields offer the best opportunity to identify millimetre- and submillimetre-bright galaxies and to construct the most complete redshift distribution yet. By utilizing the analysis of AzTEC sources in both GOODS fields discussed in § 3, we now have the opportunity to augment our understanding of the SMG redshift distribution with improved statistics.

In Figures 4 and 5, we show the redshift distributions for the robust AzTEC counterparts in both GOODS fields. We use spectroscopic redshifts when available (22 robustly identified sources) and photometric redshifts otherwise, and we plot separately the distributions determined using z_{opt} and z_{MR} in both Figures. The redshift distributions based
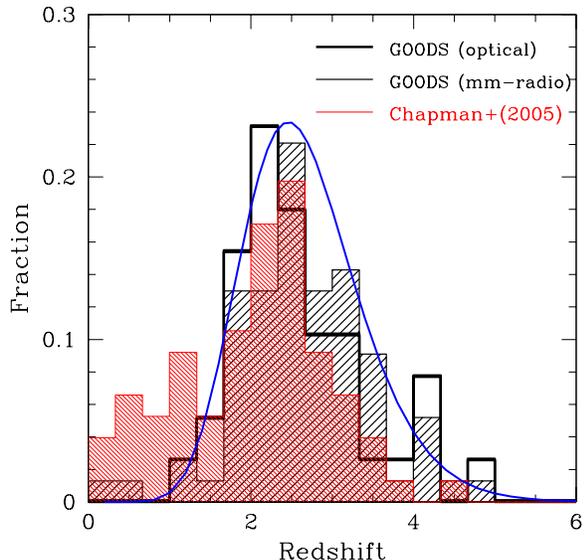
Figure 4. Redshift distributions of AzTEC sources in both GOODS fields based on the optical photoz (z_{opt}, $N = 38$; blank histogram) and the millimetric photoz (z_{MR}, $N = 74$; hatched histogram) are compared with that of the 76 radio-identified SCUBA sources with spectroscopic redshifts by Chapman et al. (2005, shaded histogram). The solid blue curve shown is a lognormal distribution as a function of $(1 + z)$ with a mean redshift of $z_{\mu} = 2.6$ and $\sigma = 0.2$.
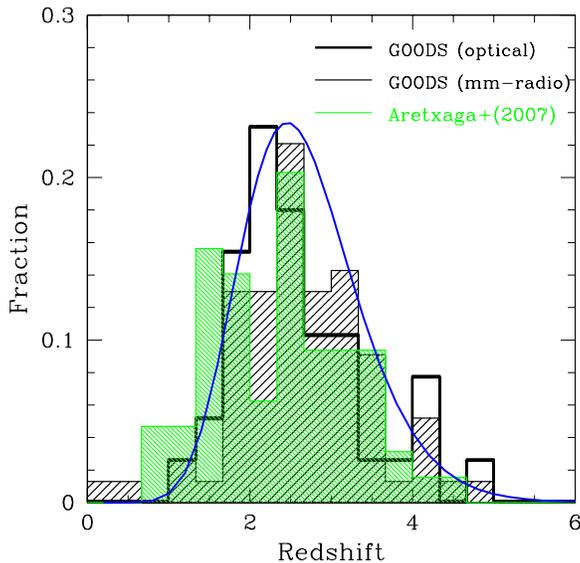
Figure 5. Redshift distribution of AzTEC sources in both GOODS fields based on the optical photoz (z_{opt}; blank histogram) and the millimetric photoz (z_{MR}; hatched histogram) are compared with that of the 64 robustly detected 850 μm sources in SHADES survey by Aretxaga et al. (2007, shaded histogram). Because of the shallow radio data in the Subaru/XMM Deep Field (SXDF), only the Lockman Hole sources are included for the Aretxaga et al. SHADES redshift distribution. The solid blue curve shown is a log-normal distribution as a function of $(1 + z)$ with a mean redshift of $z_\mu = 2.6$ and $\sigma = 0.2$.

on optical photoz (z_{opt}) and millimetric photoz (z_{MR}) are qualitatively in a good agreement with each other, while the two methods are each subject to potentially significant systematic uncertainties. These redshift distributions show that 80% of sources are at $z \gtrsim 2$, with 60% just within the redshift range between $2.0 \lesssim z \lesssim 3.3$. The relatively small number of robust counterparts with only a lower redshift limit (9 out of 74) assures that the median value of $z_{med} \approx$ 2.6 is a robust estimate. In comparison, using a different redshift estimator and analyzing the properties of 29 AzTEC sources in the GOODS-North field only, Chapin et al. (2009) derived a median redshift of $z = 2.7$, in good agreement.

The asymmetric redshift distribution of the AzTEC sources in the two GOODS fields shown in Figures 4 and 5 can be described reasonably well as a log-normal distribution of the form

$$f(z) = \frac{1}{(1+z)\sigma\sqrt{2\pi}} e^{-\frac{[ln(1+z)-ln(1+z_\mu)]^2}{2\sigma^2}} .$$

The solid curve shown in both Figures corresponds to a log-normal distribution with $z_\mu = 2.6$ and $\sigma = 0.2$ in $ln(1 + z)$. No attempt is made to derive the best fit values of z_μ and σ since some of the redshifts are only lower limits. Nevertheless, these nominal parameters simultaneously describe the rapid drop-off on the low-z side and the long tail on the high-z side.

4.2   Comparison with previous studies

The redshift distribution of the SMG population (and thus their cosmic evolution) is still poorly understood. A com-

parison of the redshift distribution derived from the AzTEC GOODS survey sources and those of of previous studies further illustrates this point. A comparison of the AzTEC sources in the two GOODS fields with that of the radio-selected SCUBA 850 μm sources by Chapman et al. (2005, Figure 4) gives an immediate impression that the two redshift distributions are substantially different. In particular, the population of $z \leqslant 1.5$ sources present in the Chapman sample is missing in our sample while the AzTEC-GOODS sample shows a broader higher redshift tail. It is important to understand the underlying causes of this difference since many studies have assumed that the redshift distribution derived by Chapman et al. is consistent with that of the SMG population as a whole (e.g. Cooray et al. 2010; Davé et al. 2010; Narayanan et al. 2010b; Vieira et al. 2010; Almeida et al. 2011; Williams et al. 2011). As noted by Chapman et al. and further discussed below (§ 4.3), these differences may be rooted in the use of radio selection for defining the Chapman sample.

Another insightful comparison is made in Figure 5 by examining the redshift distribution of the GOODS AzTEC sources with the photometric redshifts of the 64 robustly detected 850 μm sources in the SHADES survey by Aretxaga et al. (2007). The Aretxaga et al. redshift distribution is also largely missing the low-z population, and the agreement with our redshift distribution is better. If we take into account that 11 out 64 redshifts by Aretxaga et al. are only lower limits with $z_{lim} \leqslant 1.5$, the redshift distribution for the AzTEC-GOODS and the SHADES Lockman Hole sources is in fact very good.

A more quantitative comparison of the derived redshift distributions is made using the Astronomy Survial Analysis (ASURV; Feigelson & Nelson 1985) package, which properly takes into account lower redshift limits.[8] As summarized in Table 4, the only pairs of redshift distributions showing non-negligible probability of being drawn from the same parent sample are between z_{MR} and z_{opt} and between z_{MR} and the photometric redshifts of the 850 μm sources in the SHADES survey by Aretxaga et al. (2007). On the other hand, both Gehan's Generalized Wilcoxon test and the Logrank test suggest that there is *at most* 3% probability that the Chapman et al. redshift distribution is consistent with those of the GOODS AzTEC sources or the SHADES 850 μm sources in the Lockman Hole region as analyzed by Aretxaga et al. The Kaplan-Meier estimator gives the mean redshifts of $< z_{MR} >= 2.689 \pm 0.112$ and $< z_{opt} >= 2.516 \pm 0.129$. The inclusion of lower limits in the redshift for radio-undetected

---

[8] This analysis assumes that the censored data follow a similar distribution to that of the measured population.

Table 5. The K-S test probability that two redshift distributions are drawn from the same distribution, derived using the cumulative distributions of the same samples as in Table 4 but excluding lower limits.

	z_{opt}	z_{MR}	Chapman05	Aretxaga07
z_{opt}	–	0.845	0.250	0.098
z_{MR}		–	0.014	0.362
Chapman05			–	0.0014

Table 4. Comparison of mean redshifts and probabilities that two redshift distributions are drawn from the same parent distribution derived using the ASURV, as described in Section 4. The first row shows the number of redshift data points (N_d) and lower limits (N_l) used. The second row shows the Kaplan-Meier estimator for the mean and standard deviation of the redshift distribution. The last three rows show, first, the Gehan's Generalized Wilcoxon test probability for each pair, and second, the Logrank test probability.

	z_{opt}	z_{MR}	Chapman05	Aretxaga07
(N_d, N_l)	(38, 0)	(74, 9)	(76, 0)	(64, 23)
$< z >$	2.516 ± 0.129	2.689 ± 0.112	2.000 ± 0.104	2.695 ± 0.098
z_{opt}	–	0.19 / 0.21	0.030 / 0.026	0.06 / 0.30
z_{MR}		–	0.0001 / 0.0001	0.51 / 0.85
Chapman05			–	0.0000 / 0.0001

sources appears to be the primary difference for these estimates (see below). The mean redshift of the Aretxaga et al. sample is 2.695 ± 0.098, in a good agreement with that of $< z_{MR} >$. In contrast, the mean redshift of the Chapman et al. sample is 2.000 ± 0.104, significantly lower.

The robustness of these analyses is further tested by conducting a K-S test for the same pairs of redshift distributions but excluding lower redshift limits. Again, as summarized in Table 5, the hypothesis that the Chapman et al. redshift distribution is identical to the z_{MR} or Aretxaga et al. redshift distribution can be rejected with better than 98% confidence while the same hypothesis for the other combinations of pairs cannot be rejected. Nevertheless, both the survival analysis and the K-S tests are giving us consistent results in that the Chapman redshift distribution is substantially different from the SMG redshift distribution derived by us using the GOODS AzTEC sources and that of the Lockman Hole 850 µm sources in SHADES survey by Aretxaga et al.

4.3 Wavelength-dependent selection bias

As discussed in some detail by Chapman et al. (2005), their radio-selection for a spectroscopic redshift survey is intrinsically biased toward low redshift galaxies and those with cold dust temperature. The observed radio flux density suffers from a strong *positive* k-correction, fading faster with increasing redshift than expected from the inverse square law. This means the majority of faint ($S_{1.4GHz} \geqslant$ 30-40 µJy) radio sources are at $z \leqslant 1$ and only extremely luminous ($P_{1.4GHz} \geqslant 10^{24}$W Hz^{-1}) radio sources are detectable at $z > 2$ (e.g. Smolcic et al. 2008; Strazzullo et al. 2010). Chapman et al. discussed this foreground confusion and removed about 10% of the sources from their sample, but the significant number of $z \leqslant 1.5$ sources remaining in their sample (but unseen in our sample and Aretxaga et al. sample) suggests that they under-estimated the foreground confusion. Chapman et al. also considered the effects of rapidly declining sensitivity of the radio data with redshift, but they focused mainly on the dust temperature dependence on radio-IR correlation, assuming that the majority of sources undetected in the radio bands are at the same redshifts as those detected. The significant high redshift ($z > 3$) tail for the AzTEC and SCUBA sources seen in Figures 4 and 5 suggests that the highest redshift sources are missing in radio-selected samples like Chapman et al. because the depth of the available radio data is not sufficient to detect most SMGs at $z \gtrsim 3$. Mapping the true

redshift distributions of SMGs will require future complete spectroscopic redshift surveys using instruments such as the Redshift Search Receiver (Erickson et al. 2007) on the Large Millimeter Telescope or the Atacama Large Millimeter Array.

These discussions of k-correction and dust temperature raise another important question as whether SMGs selected at 850 µm and 1100 µm (and as a natural extension at 250-500 µm by the *Herschel* SPIRE instrument) are systematically different. Since the dust peak passes through these bands at different redshifts, some wavelength-dependent selection effects are expected. For example, identification of "drop-out" objects in these bands has been suggested as a means to identify the highest redshift SMG population (see Pope & Chary 2010). When we noted the low rate of coincidence between the LABOCA 870 µm sources and our AzTEC survey initially (see S 2.2), this wavelength-dependent selection bias was one of the causes we explored, although we eventually concluded that the low completeness of the both surveys is the primary cause. The general agreement between the redshift distributions of SCUBA 850 µm selected sources by Aretxaga et al. (2007) and the AzTEC 1100 µm sources seen in Figure 5 suggests that the redshift distribution and SEDs of the SMG population is such that the sources identified at these two wavelengths are indeed similar.

5 OPTICAL AND IR LUMINOSITY AND STAR FORMATION

5.1 Not all SMGs are faint and red in the rest-frame UV and optical bands

Although SMGs are a recently recognized class of galaxies, their relatively high density (0.1-0.5 arcmin^{-2}) and high luminosity ($L_{IR} \gtrsim 10^{12-13}L_\odot$) suggest that they represent a significant component of the general galaxy population and should play an important role in the overall galaxy evolution scenario. In the "down-sizing" scenario (Cowie et al. 1996), more massive galaxies are thought to have been assembled earlier in cosmic history, presumably with a higher star formation rate (SFR). Luminous infrared galaxies (LIRGs) and ultraluminous infrared galaxies (ULIRGs) with SFR $\gtrsim$ 10-100 $M_\odot$ yr^{-1} are the dominant contributor to the cosmic star formation history at $z \sim 1$ (Le Floc'h et al. 2005; Magnelli et al. 2009, 2011), and a significant contribution by SMGs with SFR of $\gtrsim 10^{2-3}M_\odot$ yr^{-1} would represent a natural progression at $z > 1$. Massive galaxies with stellar

ingly, Chapman et al. (2005) targeted their own sample for spectroscopy using the Keck Telescopes and successfully obtained emission and absorption line redshifts for about 50% of their sample.

A major motivation for this work is to clear up the confusion about the rest-frame optical and UV properties of SMGs by examining a robustly identified large sample with significantly improved statistics by taking advantage of the deep multiwavelength data available in the GOODS fields. In Fig. 6 we examine the rest-frame UV and optical properties of SMGs by plotting the measured i-band and K-band photometry of robustly identified AzTEC sources in the GOODS-South field (this work) and the GOODS-North field (Perera et al. 2008; Chapin et al. 2009) – also see Pope et al. (2006). Sources identified by the SCUBA 8-mJy survey (Ivison et al. 2002; Smail et al. 2004) and the SCUBA Lens Survey (Smail et al. 2002) are also shown for comparison. A remarkable result is that SMGs span a very broad range of brightness in both i- and K-band (rest frame $\lambda = 240$ nm & 630 nm at $z = 2.5$), spreading over 10 magnitudes, or a factor of 10^4 in flux density. The apparent brightness of the AzTEC GOODS sources by themselves span over 7 magnitudes with a median brightness of $i = 25.3$ and $K = 22.6$ when the upper limits are taken into account. Although there is some overlap with the sources identified by the earlier SCUBA 8-mJy survey and the SCUBA Lens Survey, the *AzTEC GOODS counterpart sources are systematically fainter by ~ 3 magnitudes on average.* Because earlier SMG identification studies relied on K-band data too shallow to detect the majority of the AzTEC counterparts in the GOODS-South field, this means earlier works may have missed or mis-identified the counterparts in many cases. The few but highly secure SMG counterparts identified recently using deeper optical and near-IR data and high resolution interferometric imaging in the millimeter and submillimeter bands (shown as asterisks – Iono et al. 2006; Younger et al. 2007, 2008, 2009; Hatsukade et al. 2010; Wang et al. 2007, 2011) have a brightness distribution more closely matching that of the AzTEC sources in both GOODS fields.

We also deduce from the observed scatter in Fig. 6 that there is at least a factor of 10 variation in the intrinsic rest frame optical luminosity among these SMGs. When viewed together with SCUBA-detected sources, these SMGs form a broad color track centered roughly around the $i - K = +3$ line (short-dashed line), which is quite red compared with field galaxies. Some sources show a relatively flat color ($i - K = +1$) while there are others with extremely faint i-band upper limits and colors redder than $i - K = +6$. The scatter about the mean relation appears to increase at $K \gtrsim 22$, but the source density is also higher at these fainter magnitudes. The full range of the scatter perpendicular to the mean relation is about 4 magnitudes in color. This large spread in color substantiates the earlier suggestion that optical properties of SMGs are quite diverse (e.g., Ivison et al. 2000, 2002). However it cannot fully account for the up to ~ 10 magnitude spread in their apparent brightness as a population. In other words, there is an additional factor of $\gtrsim 100$ variation (or $\gtrsim 5$ mag) in the apparent brightness of SMGs on top of the apparent differences in color, which may be due to variations in SED and extinction. Given their extreme luminosity, the SMG phase likely represents a brief, special moment during the rapid mass build-up phase (e.g.,

Figure 6. Measured K-band versus i-band magnitudes of the robustly identified AzTEC counterpart sources (circles). Lines of constant colors with $i - K = +0$, $+3$, & $+6$ are shown. Circles with filled dots are AzTEC sources with *Chandra* X-ray detection in the GOODS-North and GOODS-South fields while empty circles are the sources without X-ray detection. Crosses represent the 17 "securely" identified counterparts to the SCUBA 8-mJy survey (Ivison et al. 2002) and the SCUBA Lens Survey (Smail et al. 2002) sources. Asterisks are SMGs securely identified by interferometric measurements at millimetre and submillimetre wavelengths (Iono et al. 2006; Younger et al. 2007, 2008, 2009; Hatsukade et al. 2010).

mass $M_* \gtrsim 10^{11} M_\odot$ are thought to be already in place by $z \sim 2$ (van Dokkum et al. 2008). Galaxies with even higher SFR might be found at higher redshifts.

What would these SMGs look like in the rest-frame UV and optical bands? And how do they fit into the larger population of high redshift galaxies identified in those more traditional bands? Optical/UV size, morphology, and luminosity could provide an important test for their origin as merger-driven starbursts (e.g., Narayanan et al. 2010b) or large disk systems (Efstathiou & Rowan-Robinson 2003; Kaviani et al. 2003; Hayward et al. 2011) fueled by a high rate of cosmological gas accretion (Keres et al. 2005; Davé et al. 2010). Early studies in the optical and near-IR suggested a diverse population of bright, modest redshift ($z \lesssim 1$) and faint, high-redshift ($z \sim 2$) galaxies, as reported by Lilly et al. (1999), Barger et al. (1999, 2000), Ivison et al. (2000), Fox et al. (2002), and Ivison et al. (2002). However, high resolution interferometric imaging studies at millimeter wavelengths (Bertoldi et al. 2000; Frayer et al. 2000; Lutz et al. 2001; Dannerbauer et al. 2002) have shown that the SMG counterparts are often undetected in the optical bands. A study of a large sample of radio-identified SMGs using deeper optical data by Chapman et al. (2001) showed that their counterparts are indeed quite faint ($I > 25$), and Chapman et al. concluded that dust obscuration makes these galaxies essentially invisible in the ultraviolet bands. This conclusion is not universally accepted, however – see Ivison et al. (2002). Interest-

Narayanan et al. 2010b; Hayward et al. 2011). If the majority of SMGs are seen in the redshift range between 1.5 and 4.0 (see § 4), then the spread in the luminosity distance can account for about a factor of 10 in the apparent brightness variation. Therefore, the remaining factor of $\gtrsim 10$ scatter in apparent brightness has to be accounted for by an intrinsic scatter in the rest-frame optical band luminosity.

In the broader context of understanding star forming galaxies in the early universe, some of the AzTEC sources are bright in the rest-frame UV and optical bands and are already identified as star forming galaxies by past surveys. For example, about 30% are bright enough in the optical and NIR bands to be classified as "BzK" galaxies (Daddi et al. 2004) using the existing photometry – see discussions in Appendix. Some of the $z \sim 4$ SMGs have also been identified as "Lyman break galaxies" (see Capak et al. 2008). On the other hand, the majority of the AzTEC GOODS sources are too faint and red to have been identified in previous surveys of star forming galaxies and are likely to be entirely missed in the current accounting of the cosmic star formation history. Future millimetre wavelength surveys with higher angular resolution are needed to probe deeper into the lower flux density (and lower luminosity) regime in order to bridge these populations and obtain a complete census of star forming galaxies.

5.2 SMGs as massive galaxies in a phase of rapid stellar mass build-up

5.2.1 Stellar luminosity of SMGs

One constant in the high resolution interferometric millimetre and submillimetre observations of SMGs is the presence of a *Spitzer* IRAC counterpart in the 3.6-8.0 μm bands, and
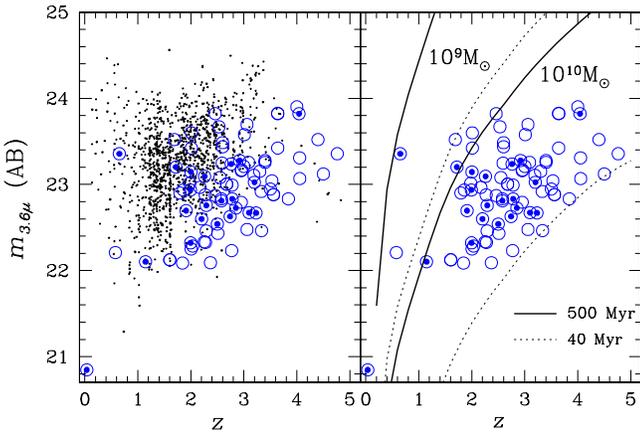
Figure 7. *Spitzer* IRAC 3.6 μm band "Hubble diagram". IRAC 3.6 μm band brightness ($m_{3.6\mu}$) of the robust AzTEC counterparts is plotted as a function of redshift. Symbols are the same as in Fig. 6. Small dots on the left panel are $K-$band selected star forming galaxies with known spectroscopic redshifts in both GOODS fields. The apparent brightness of a 40 Myr starburst population with a stellar mass of 10^9 and $10^{10} M_\odot$ is shown in dotted lines, while the same population after passively evolving for 500 Myr is shown in solid lines. An exponentially decaying starburst history with a 20 Myr e-folding time and solar metallicity is assumed for the models.

this is one of the key features we employ to identify AzTEC counterparts (see § 2). A comparison of the apparent brightness in the 3.6 μm band (rest-frame optical or near-IR) for the AzTEC counterparts and other K-band selected $z \sim 2$ starforming galaxies with known spectroscopic redshifts in both GOODS fields is shown in Fig. 7a. While there is some overlap between these two populations, the AzTEC counterparts are systematically brighter by $\gtrsim 1$ magnitude on average and represent the most luminous galaxies at these redshifts. This intrinsically high luminosity in the rest-frame optical and near-IR bands is clearly an important reason why these AzTEC sources are so readily detected by *Spitzer*.

Since AzTEC detection requires highly efficient dust-processing of the UV radiation from young stars, the high inferred luminosity in the rest-frame optical/NIR bands seems surprising. After all, we just established in the previous section (§ 5.1) clear evidence for severe attenuation of UV radiation among many of these objects. A natural explanation for this apparent puzzle is found in the studies of the local ULIRG population. An imaging study of local ULIRGs in the near- and far-UV bands by Goldader et al. (2002) has shown that activity traced in the UV bands is distributed over kiloparsec scales and is heavily obscured, particularly in the regions of the most intense starburst activities. When observed at redshifts of $z \sim 2$ to $z \sim 4$, these ULIRGs are expected to be extremely red and faint in the observed optical and NIR bands ($R-K$ = 4-6, $K \approx$ 21-24), similar to the observed values for the AzTEC sources shown in Fig. 6. At the same time, Chen et al. (2010) have shown that the stellar hosts of local ULIRGs are also extremely blue in rest-frame optical bands and are on average ~ 1 magnitude *brighter* than the field star-forming population, owing to distributed star formation activity and the high intrinsic luminosity of young stellar clusters. A Hubble Space Telescope NICMOS and ACS imaging study by Swinbank et al. (2010) has also found evidence for ongoing mergers and structured dust obscuration among $z \sim 2$ SMGs, further supporting the parallel in the observed source luminosity and structure between the local ULIRGs and high-z SMG population.

One cannot automatically conclude from their large observed luminosity that these SMGs are also the most massive galaxies at their observed epochs if their luminosity is powered by a large population of widely distributed young stellar clusters. The apparent 3.6 μm brightness of a single stellar population starburst model with a total accumulated stellar mass (M_*) of $10^9 M_\odot$ and $10^{10} M_\odot$ is shown in Fig. 7b for two different scenarios: 40 Myr (dotted lines) and 500 Myr (solid lines) after the initial burst. The observed brightnesses of AzTEC sources are well-bounded by the 40 Myr old starburst models with stellar masses of $10^9 M_\odot$ and $10^{10} M_\odot$, which are about *10 times smaller* than the stellar masses derived for the $K-$band selected star forming galaxies shown in comparison ($M_* = 10^{10-11} M_\odot$, Daddi et al. 2007). However, after just 500 Myr of passive evolution, the same starburst systems fade by ~ 2 magnitudes at $z \sim$ 2-4, bringing them back to a better agreement with the mass estimates for the $K-$band selected star-forming galaxies. Alternatively, accounting for the observed 3.6 μm band brightness of the AzTEC sources assuming a maturing stellar population would require stellar masses well in excess of $10^{11} M_\odot$.
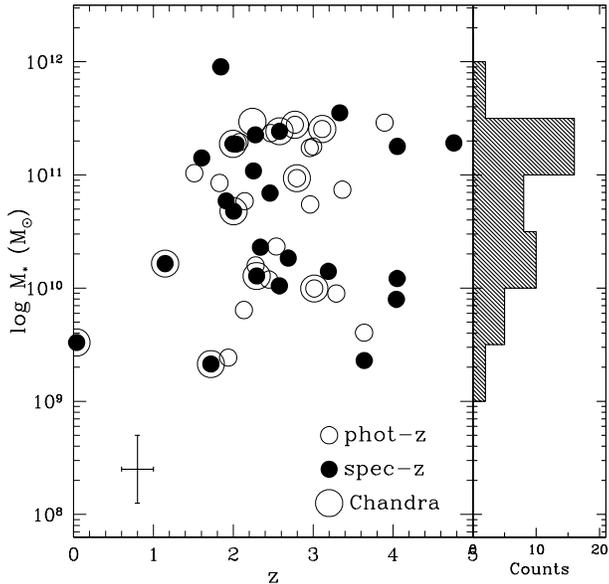
Figure 8. The stellar masses of AzTEC counterparts derived from optical and NIR photometry as a function of redshift. A histogram of stellar masses is shown on the right panel. Sources with a spectroscopic redshift are shown as solid symbols while the ones with a photometric redshift are shown as empty circles, and they represent similar ranges of stellar mass. Typical uncertainties for the M_* and photo-z estimates are shown on the bottom left corner. Those detected by the *Chandra* in the X-ray are identified with a larger circle. Only GOODS TFIT catalog sources with a proper stellar mass estimate are included.

5.2.2 *Stellar mass and star formation rate of SMGs*

We can get a better handle on the stellar mass by modeling the observed rest-frame UV and optical SED as discussed in § 3.1. The derived stellar masses from the modeling of the UV-optical SED, shown in Figure 8, range between 10^9 to $10^{12} M_\odot$. The majority of the derived stellar masses are between 1 and 30 times $10^{10} M_\odot$, similar to those of the $K-$band selected massive star-forming galaxies at the same redshift, such as those discussed in Daddi et al. (2007). Similarly large stellar masses were found previously for SMGs (e.g., Dye et al. 2008; Tacconi et al. 2008; Daddi et al. 2009; Hainline et al. 2009; Michalowski et al. 2010), and they are consistent with the idea that these submillimetre-bright galaxies are associated with the peak of the stellar mass function at $z = 2$-3.

Six out of 18 AzTEC counterparts with $M_* \geqslant 10^{11} M_\odot$ are also X-ray sources detected in deep *Chandra* surveys. The frequency of the *Chandra* detected sources is about the same for the lower stellar mass galaxies (seven out of 25), and there is little evidence for any dependence on stellar mass. The low number of $z \geqslant 3$ sources detected by the 2-4 Ms *Chandra* surveys may reflect the limiting sensitivity of the X-ray data, and the observed X-ray fraction is a lower limit. Given the poor statistics, it is difficult to conclude whether the presence of a luminous AGN is influencing the modeling of the rest-frame optical SEDs.

The rest-frame optical SED modeling also yields a UV-derived star formation rate (SFR_{UV}). The derived SFR_{UV} for the AzTEC-GOODS sources cover a broad range: $1 - 2000 M_\odot$ yr^{-1} – see the left panel of Figure 9. A sur-

prising result is that the derived SFR_{UV} is quite high, $\geqslant 100 - 1000 M_\odot$ yr^{-1} for about 50% of the cases. The observed SFR_{UV} distribution is also nearly independent of stellar mass. The SFR_{UV} distribution broadly overlaps the observed $SFR - M_*$ relation for the K-band selected galaxies studied by Daddi et al. (2007, dashed line), but there is little evidence that these AzTEC sources follow the same $SFR - M_*$ relation. The AzTEC-GOODS sources also do not follow the $SFR - M_*$ relation predicted by the $z = 2.5$ model SMGs fueled by cold flow accretion (Davé et al. 2010, solid line). Some of the galaxies with the highest SFR_{UV} are detected in the X-ray by *Chandra*, raising the possibility that the UV light from the central AGN might contribute to these high values. However, not all *Chandra* detected sources are associated with a high SFR_{UV}, and neither the SFR_{UV}/SFR_{IR} ratio nor the specific star formation rate discussed below offer any clear evidence to support this idea.

For comparison, IR-derived star formation rates (SFR_{IR}) determined from modeling the IR SED are shown in the middle panel of Figure 9. The SFR_{IR} is uniformly high, $\geqslant 100 - 1000 M_\odot$ yr^{-1}, with a much smaller scatter and completely independent of stellar mass. This is expected since these confusion-limited AzTEC surveys preferentially select sources with intrinsically large L_{IR}. We note that the 1.1mm selection does not *guarantee* a high L_{IR} or SFR_{IR} if cold dust ($T_d = 10 - 20$ K) emission dominates the millimetre spectrum. On the other hand, our SED modeling does not find any cold dust dominated sources with $L_{IR} < 10^{12} L_\odot$. Since the IR luminosity accounts for the total amount of dust-processed UV radiation, a comparison of SFR_{IR} with SFR_{UV} should offer a crude measure of the geometry between the young stars and the obscuring dust. The large SFR_{UV} derived for a large fraction of AzTEC-GOODS sources is particularly interesting in this regard, and this result may indicate that star formation activities and dust distribution in these SMGs are not as concentrated as in the local ULIRGs, where $L_{IR} \approx L_{bol}$ (see Sanders & Mirabel 1996).

To explore the relationship between SFR_{UV} and
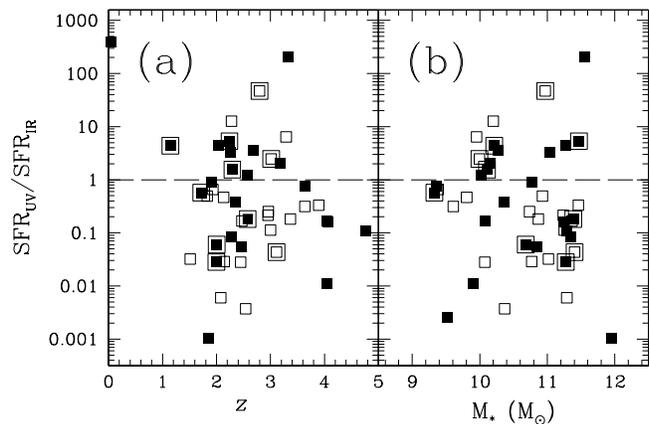
Figure 10. The ratio of SFR derived from the rest-frame UV (SFR_{UV}) and the rest-frame IR (SFR_{IR}) as a function of (a) redshift and (b) stellar mass (M_*). Galaxies with spec-z (photo-z) are shown in filled (empty) symbols, and those detected by the *Chandra* in the X-ray are identified with a larger square. The dashed line marks the $SFR_{UV} = SFR_{IR}$ relation.
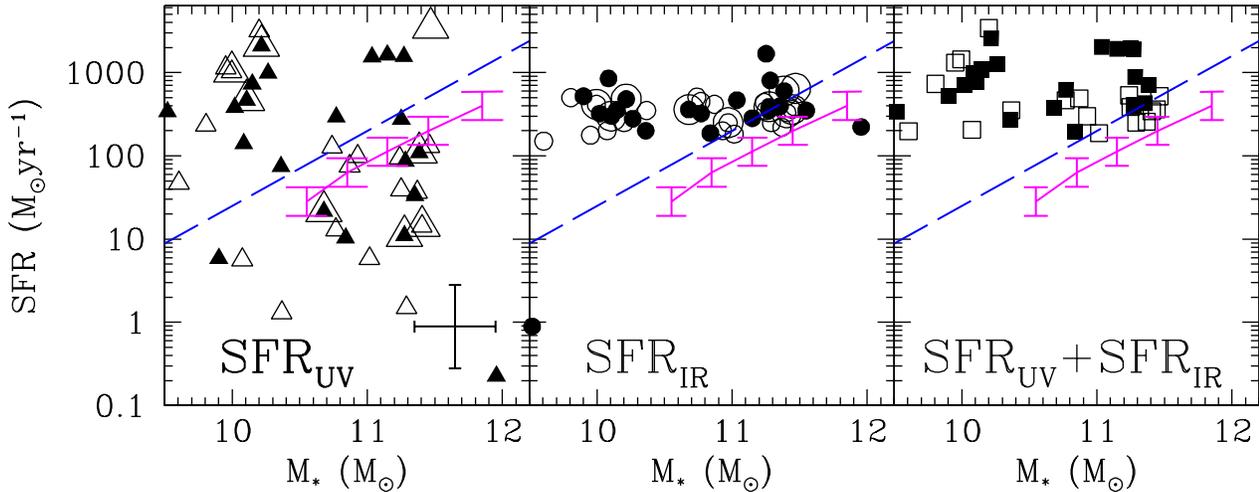
Figure 9. Star formation rates for AzTEC GOODS sources estimated from the rest-frame UV (SFR_{UV}) and IR (SFR_{IR}) as a function of stellar mass. Open and filled symbols represent photometric and spectroscopic redshifts, and those detected by the *Chandra* in the X-ray are identified with a larger symbol. A typical overall uncertainty for an object with photoz is shown on the bottom right corner of the left panel. The mean $SFR - M_*$ relation for the $z = 2.5$ model SMGs fueled by cold flow (Davé et al. 2010) is shown by a solid line. Long-dashed line is the observed mean $SFR - M_*$ relation for the K-band selected galaxies (Daddi et al. 2007). The SMGs do not seem to follow either trends.

SFR_{IR} further, their ratios are plotted as a function of redshift and M_* in Figure 10. This ratio varies widely from one source to another, spanning over 5 decades in total range, and it is independent of z and M_*. Finding a large number of sources with $SFR_{UV}/SFR_{IR} > 1$ is particularly puzzling for these galaxies with a large stellar mass. A misidentification of the counterparts is also a plausible explanation, but the observed distribution would require the failure of counterpart identification in a large fraction of cases. Either an under-estimate of SFR_{IR} or an over-estimate of SFR_{UV} (and possibly both) can provide an explanation, as the estimates of both SFR and M_* are subject to significant systematic uncertainties (e.g., see Maraston et al. 2010). If these galaxies represent young galaxies seen during their rapid mass build-up phase (see below), then the well-known mass-metallicity relation (Tremonti et al. 2004) and the attenuation of UV light in the local universe may not be directly applicable. The presence of an X-ray source detected by *Chandra* is not correlated with the SFR_{UV}/SFR_{IR} ratio, and the presence of an X-ray emitting AGN does not seem to contribute directly to the derived SFR_{UV} in most cases.

5.2.3 Specific star formation rate and mass build-up history

Charting the star formation and stellar mass build-up history is one of the most powerful tests for galaxy evolution theories. For example, the emergence of red sequence galaxies that are massive and passively evolving around $z \sim 1$ and their increase in number with time are widely cited as important observational constraints that require additional complexities such as AGN feedback and "dry" mergers (Bell et al. 2004, 2007; Faber et al. 2007). Statistical studies such as the Sloan Digital Sky Survey have shown that the bulk of stars now in massive galaxies formed at earlier epochs than stars in lower mass galaxies (e.g.,

Kauffmann et al. 2003), suggesting a strong link between galaxy mass and star formation history. A particularly useful quantity to examine in this regard is the specific star formation rate (SFR per unit stellar mass; $SSFR \equiv SFR/M_*$). A systematic dependence of $SSFR$ on galaxy mass and a rapid increase of $SSFR$ with redshift have been established by several recent studies (Zheng et al. 2007; Damen et al. 2009). Given the large stellar masses ($M_* = [1-30] \times 10^{10} M_\odot$) and SFRs ($> 10^{2-3} M_\odot \ yr^{-1}$) for these $z = $ 2-4 SMGs, examining their $SSFR$ in the context of the observed trends with stellar mass and redshift may provide a valuable new insight into the physical mechanisms driving the SMG phenomenon and massive galaxy formation.

The computed $SSFRs$ for the AzTEC-GOODS sources are shown in Figure 11. An immediately noticeable trend is that the derived $SSFRs$ are uniformly quite high, $SSFR \approx$ 1-100 Gyr^{-1}. Among the optically selected samples, galaxies with $SSFR \gtrsim 10 - 100 \ Gyr^{-1}$ are generally associated lower stellar mass ($M_* \leqslant 10^{10} M_\odot$) galaxies undergoing a starburst episode. More massive galaxies in the local universe are associated with 1-2 orders of magnitudes lower $SSFR$ (Bauer et al. 2005; Feulner et al. 2005; Erb et al. 2006; Elbaz et al. 2007). The same trend also holds at higher redshifts as the $K-$band selected star forming galaxies at $z \sim 2$ have on average $SSFR \approx 1 \ Gyr^{-1}$ (Daddi et al. 2007), overlapping only at the bottom range of the $SSFR$ associated with the AzTEC sources. Pannella et al. (2009) have also reported an average $SSFR \approx 5 \ Gyr^{-1}$ and $SFR \approx 100 M_\odot \ yr^{-1}$ for their $z \sim 2$ radio-identified star forming galaxies with an average $M_* = 3 \times 10^{10} M_\odot$ at $z \sim 2$ (also see Dunne et al. 2009).

The $SSFRs$ for the AzTEC-GOODS sources are significantly higher than those of similar stellar mass galaxies in the local Universe, and they appear to follow the same broad trend of rapidly increasing $SSFR$ with redshift. The dotted line shown in Figure 11 is the stellar mass-dependent $SSFR$ evolution mapped by Damen et al. (2009) for mas-
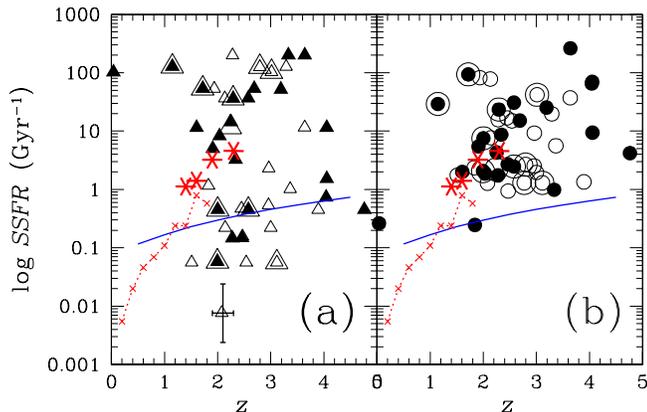
Figure 11. Specific star formation rate of AzTEC counterpart candidates derived from the (a) rest-frame UV and optical SED fitting and (b) far-IR SED fitting using Efstathiou et al. (2000) dusty starburst SED templates. Solid and empty symbols represent the sources with spectroscopic and photometric redshifts, respectively, and those detected by *Chandra* in the X-ray are identified with a larger symbol. A typical uncertainty is shown for one of the photo-z sources at the bottom of the left panel. The asterisks represent the radio-derived SSFRs for star forming galaxies with $M_* \sim 3 \times 10^{10} M_\odot$ derived by Pannella et al. (2009). The solid line represents the inverse of the Hubble time, and sources above this line are in a starburst mode. The dotted line connecting the crosses represents the average $SSFR$ for massive galaxies with $M_* \geqslant 10^{11} M_\odot$ found by Damen et al. (2009).

sive galaxies with $M_* \geqslant 10^{11} M_\odot$, and it shows a rapid rise as $SSFR \propto (1 + z)^5$ between $z = 0$ and $z = 2$. The radio-derived $SSFR$s for star forming galaxies with $M_* \sim 3 \times 10^{10} M_\odot$ derived by Pannella et al. (2009), shown in asterisks, extend this rapidly rising trend to $z \sim 2.5$. The AzTEC-GOODS sources extend this rise in $SSFR$ further to $z \sim 4$, although there is significant scatter. As noted by Damen et al. and others, there is a mass-dependence on the $SSFR$ evolution, and the spread in M_* for the AzTEC sources likely contributes to some of the observed scatter.

The $SSFR$s derived for the AzTEC-GOODS sources provide the strongest evidence yet that SMGs are seen during the brief phase of rapid stellar mass build-up. The solid lines in Figure 11 represent the inverse of the Hubble time, $1/t_H$: only galaxies with $SSFR$s above this line have sufficiently high SFRs to build up their current stellar masses within the Hubble time at their respective redshifts. Considering the SSFRs derived from fitting the FIR SEDs (right panel of Figure 11), all of the AzTEC GOODS SMGs are located at or above this critical line. We cannot exclude the possibility that these SMGs are rejuvenated galaxies, undergoing another episode of extreme luminosity, but it would require an even earlier episode of rapid stellar mass build-up. Citing extremely high SFR and similar density, previous studies have made plausible arguments for identifying SMGs as progenitors of present day massive elliptical galaxies (e.g., Blain et al. 2004). Our new analysis of the $SSFR$ allows us to demonstrate quantitatively that these SMGs are seen *during* a phase of rapid stellar mass build-up.

The absence of AzTEC sources with $SSFR$ below the $1/t_H$ line in the right panel of Figure 11 is primarily the result of AzTEC survey depth – in fact, all existing confusion limited surveys carried out with, e.g., AzTEC and

Herschel, probe only the brightest end of the luminosity function. Much of the cosmic IR background (CIRB) is expected to arise from fainter sources below the confusion limit, and their number counts can offer an important constraint to the evolution model for SMGs (Granato et al. 2004; Baugh et al. 2005; Rowan-Robinson 2009). The location of the $1/t_H$ line in Figure 11 leaves a fairly limited parameter space for a lower luminosity dust-obscured starburst population that can contribute significantly to the CIRB – e.g., $SFR \approx 20\text{-}100\ M_\odot\ \mathrm{yr}^{-1}$ for a (1-5) $\times 10^{10} M_\odot$ galaxy at $z = 2$. A $z \gtrsim 2$ galaxy with $M_* \geqslant 10^{10-11} M_\odot$ can still appear with a $SSFR$ below this $1/t_H$ line, but the presence of a large population of such galaxies would have an important consequence in that the formation epoch of those massive galaxies has to be pushed to a much earlier time. The decreasing t_H with redshift also requires an even larger SFR with increasing z, and in turn the submm/mm-detected fraction of galaxies with a stellar mass $M_* \geqslant 10^{10-11} M_\odot$ has to rise with increasing redshift. The high detection rate of optically selected $z \geqslant 4$ QSOs in the submm/mm continuum ($\sim 30\%$, Carilli et al. 2001; Wang et al. 2007, 2008), despite the selection bias against obscured systems, appears to be in line with this expectation.

The $SSFR$ analysis of the AzTEC-GOODS sources also suggests an intriguing idea that there may be two classes of SMGs, possibly driven by two different modes of star formation or observed at two different phases. While the M_* for these SMGs span over a factor of 30 (see Fig. 8), the SFR_{IR} and $SFR_{UV} + SFR_{IR}$ show no dependence on M_* in Figure 9. This is in contrast to the finding by Davé et al. (2011), where a tight M_*-SFR relation is a generic outcome of all of their cosmological hydrodynamic simulations incorporating galactic outflows. One way to interpret our observational results summarized in Figure 9 is that only SMGs with $M_* \gtrsim 10^{10.5}$ have properties similar to the objects modeled by Davé et al., following the M_*-SFR relation predicted for SMGs (solid line in Figure 9, Davé et al. 2010). AzTEC-GOODS sources with $M_* < 10^{10.5}$ may follow a different, currently unknown process that leads to 10 times larger $SSFR$. This is somewhat analogous to the mass-dependent $SSFR$ seen among galaxies in the local universe ("red" and "blue sequence") with a similar range of M_*, although with 1-2 orders of magnitudes lower $SSFR$s. A division by mass certainly seems somewhat arbitrary. On the other hand, these SMGs appear to show a sign of grouping by mass in the middle and right panel of Figure 11. A hint of bimodality in the histogram of M_* is also seen in Figure 8. Future LMT and ALMA surveys of much larger samples with higher angular resolution and spectroscopic redshifts should provide a definitive test on this intriguing possibility.
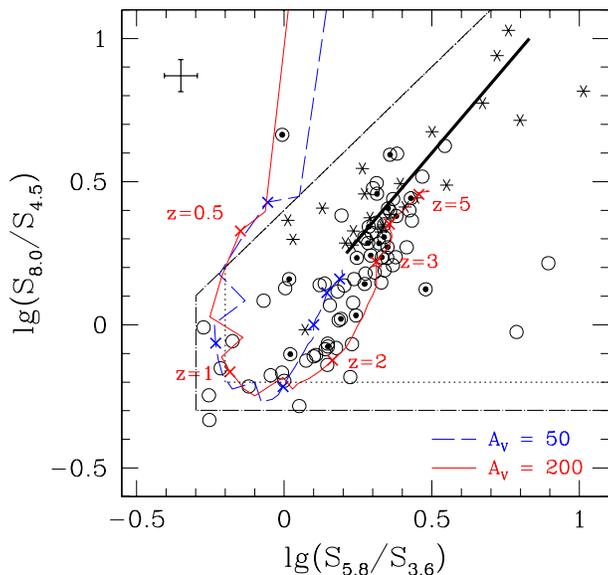
6 AGN AND STARBURST ACTIVITIES

Determining the source of enormous luminosity associated with SMGs is an outstanding problem that has important implications on understanding the mass assembly history of galaxies. To probe the nature of the heavily obscured power source, optically thin tracers in the X-ray, IR, or radio wavelengths are necessary. Here, we examine the proper-

ties of AzTEC sources identified in the GOODS-South and GOODS-North fields using several well-established diagnostic tests utilizing these optically thin tracers.
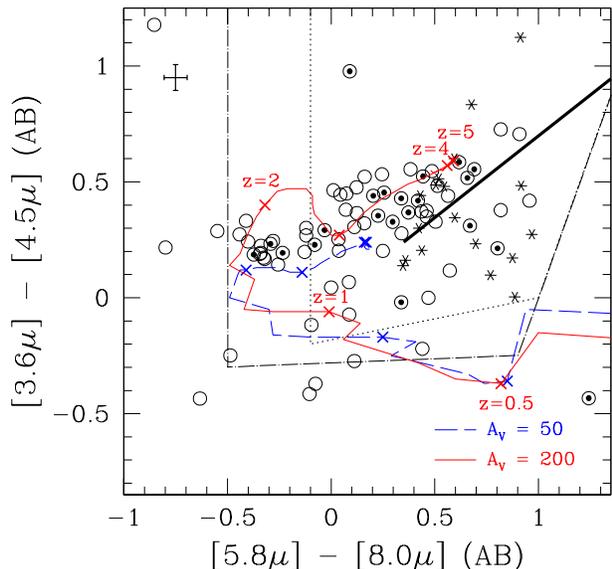
6.1   *Spitzer* **IRAC color-color diagram**

The first set of diagnostic tests to examine are the IRAC color-color diagrams that are commonly used for identifying heavily obscured AGNs based on the color combinations proposed by Lacy et al. (2004) and Stern et al. (2005) as shown in Fig. 12 and Fig. 13, respectively. The majority of robustly identified AzTEC sources in both GOODS fields fall within the regions previously identified with power-law AGNs in both plots. As argued in detail below, these results are not a direct consequence of using a *Spitzer* IRAC color selection for identifying AzTEC counterpart sources. Interpreting these results should also require some care as a young starburst population at $z > 1$ has a characteristic red SED in this part of the spectrum and should fall within the same color region (see Yun et al. 2008).

The sample size of AzTEC GOODS sources plotted in Figs. 12 & 13 is nearly 3 times larger than the sample previously analyzed by Yun et al., and these new plots show more clearly that these AzTEC sources cluster densely around

Figure 13. A $[3.6\mu] - [4.5\mu]$ versus $[5.8\mu] - [8.0\mu]$ IRAC color diagnostic diagram for heavily obscured starbursts and AGNs based on the color combinations proposed by Stern et al. (2005), adopted from Fig. 2 by Yun et al. (2008). All symbols and models shown are identical to those in Fig. 12.

Figure 12. A $S_{8.0\mu}/S_{4.5\mu}$ versus $S_{5.8\mu}/S_{3.6\mu}$ IRAC color diagnostic diagram for heavily obscured starbursts and AGNs based on the color combinations proposed by Lacy et al. (2004). Areas occupied by dusty young starbursts as noted by Yun et al. (2008, see their Fig. 1) are outlined by a dot-dashed line while the area previously identified with power-law spectrum AGNs by Lacy et al. is outlined using a dotted line. The IRAC counterparts identified with the AzTEC sources in GOODS-South and GOODS-North with empty (undetected in X-ray) and dotted circles (detected in X-ray) cluster around the theoretical dusty starburst SED tracks with different amounts of dust extinction ($A_V = 50$ & 200, Efstathiou et al. 2000), as discussed by Yun et al. (2008). The thick solid line represents the theoretical track expected of purely power-law IR AGNs, while asterisks are power-law AGNs reported by Lacy et al. and Martinez-Sansigre et al. (2008). Typical uncertainties in the colors are shown by the cross in the upper left corner.

the theoretical color tracks of 20-80 Myr old dusty starbursts at $z \gtrsim 2$ by Efstathiou et al. (2000). The dispersion in the model tracks and the observed color are larger in Fig. 13, but the AzTEC sources again mostly occupy the region spanned by the starburst model tracks, rather than the area surrounding the IR power-law track. It is particularly noteworthy that AzTEC sources identified with a *Chandra* X-ray source (dotted circles) occupy largely the same area as those without X-ray detection (empty circles), and only a small fraction of sources (both with and without X-ray detection) overlap with the IR power-law AGN (asterisks; see Yun et al. 2008). Conversely, many of the AzTEC sources appearing among the power-law IR sources are undetected in the 2 & 4 Ms *Chandra* surveys (Alexander et al. 2003; Luo et al. 2008; Johnson et al. 2011). There is a weak trend of an increasing fraction of X-ray detected sources with redder color. We can conclude from these diagnostic plots that nearly all of the AzTEC sources identified in the GOODS fields have IRAC SEDs consistent with that of a young starburst, while a small fraction ($\lesssim 20\%$) show IR colors of a power-law AGN.

One thing to clarify is that the use of IRAC colors as a method to identify the AzTEC counterparts does not lead directly to these observed trends. The adopted color selection, $[3.6\mu] - [4.5\mu] \geqslant 0.0$, imposes no restriction on the 5.8 μm and 8.0 μm photometry. This color selection is also only one of *three* independent criteria we examine jointly, and the radio data contribute overwhelmingly to the secure counterpart identification. In fact, *none* of the robustly identified sources in Table 1 are based on the IRAC color selection alone (see § 2.1). This color selection is not used to *reject* any counterpart candidates either, and indeed several robust counterparts shown in Fig. 13 have a *blue* IRAC color ($[3.6\mu] - [4.5\mu] < 0.0$). In the context of the starburst SED model tracks shown, the color selection

of $[3.6\mu] - [4.5\mu] \geqslant 0.0$ effectively imposes a redshift bias against sources at $z \lesssim 1$ such as AzTEC/GS20. However, this bias is more than compensated by the radio and MIPS identification methods that systematically favor low-z candidate counterparts.

6.2 Optical-IRAC-MIPS colors

Another widely used AGN diagnostic diagram is the *Spitzer* mid-IR color plot first introduced by Ivison et al. (2004). They noted that starburst and AGN color tracks as a function of redshift are well-separated in the plot of flux ratios $S_{24}/S_{8.0}$ vs. $S_{8.0}/S_{4.5}$ due to contributions by a power-law AGN and PAH emission in the 24 μm band. By analyzing *Spitzer* Infrared Spectrograph (IRS) data on 24 μm selected galaxies, Pope et al. (2008b) found that the main discriminatory information resides in the $S_{8.0}/S_{4.5}$ flux ratio, or the spectral slope in the rest-frame near-IR band. This color selection is similar to the earlier IRAC color analysis proposed by Lacy et al. (2004) and Stern et al. (2005), and it is again subject to the same confusion with young starburst systems as noted by Yun et al. (2008) and others. The new AGN diagnostic condition of $S_{8.0}/S_{4.5} \geqslant 2$ proposed by Pope et al. (2008b) corresponds to $lg(S_{8.0}/S_{4.5}) \geqslant +0.3$ in Fig. 12, and objects satisfying this criteria should also include dusty young starbursts at $z \leqslant 0.5$ and $z > 3$ as well as power-law IR AGNs.

Our version of the Pope et al. (2008b) diagnostic test is shown in Fig. 14, which shows the plot of the MIPS 24 μm to optical i-band flux ratio versus $S_{8.0\mu}/S_{4.5\mu}$ IRAC band flux ratio for AzTEC sources in both GOODS fields. Among
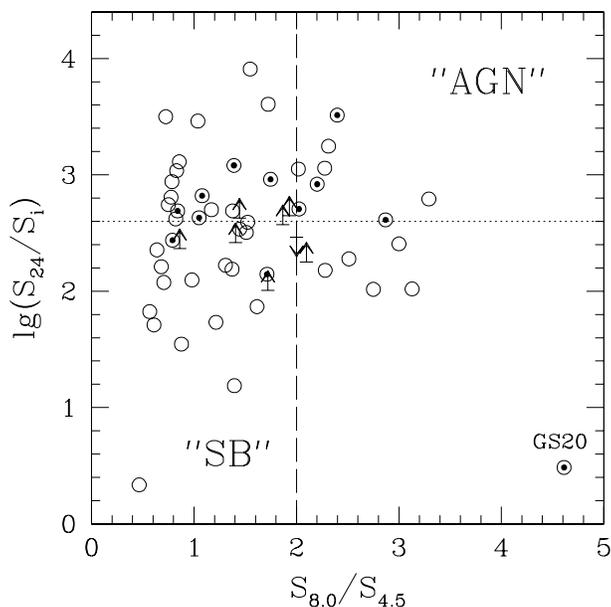
Figure 14. A diagnostic color-color diagram using MIPS 24 μm to optical i-band flux ratio versus $S_{8.0\mu}/S_{4.5\mu}$ IRAC band flux ratio. Symbols are identical to those in Fig. 12. The long-dashed line at $S_{8.0}/S_{4.5} = 2$ is the dividing line for AGNs and starbursts as proposed by Pope et al. (2008b). The dotted line near $lg(S_{24}/S_i)$=2.6 is the equivalent division line for the $z \sim 2$ "dust-obscured galaxies" with $F_\nu(24\mu m)/F_\nu(R) \gtrsim 1000$ – see Dey et al. (2008); Fiore et al. (2008).

the 57 sources plotted, only 16 (28%) have the $S_{8.0}/S_{4.5}$ flux ratio consistent with hosting an energetic AGN (right of the long-dashed line). Again, X-ray detection (dotted circles) appears to have little bearing on whether an object falls on the starburst ("SB") side or the "AGN" side. The source with the highest ratio $S_{8.0\mu}/S_{4.5\mu} = 4.6$ is AzTEC/GS20, which is a $z = 0.0369$ galaxy whose $S_{8.0\mu}/S_{4.5\mu}$ ratio arises from the bright PAH line emission in the 8 μm band, rather than due to a power-law AGN – also see Fig. 12.

The choice of the flux ratio between the MIPS 24 μm and the optical $i-$band for the vertical axis in Fig. 14 is motivated by the claim of a new class of faint MIPS 24 μm sources that were missed by earlier optical studies. These so-called "dust-obscured galaxies" ("DOGs"; Dey et al. 2008; Fiore et al. 2008) represent a population of infrared bright galaxies that are extremely faint in the optical bands, characterized by $F_\nu(24\mu m)/F_\nu(R) \gtrsim 1000$. These $z \sim 2$ galaxies have similar projected density as SMGs and may account for as much as $\sim 1/4$ of the IR luminosity density at this redshift (Dey et al. 2008; Pope et al. 2008b). Evidence for both star formation and AGN activity has been reported for these objects. Based on their stacking analysis of the X-ray hardness ratio, Fiore et al. (2008) proposed that as many as 80% of these dust-obscured galaxies host a Compton-thick AGN.

Adopting a mean color of $r - i \approx +1.0$ for the radio-selected SMGs (e.g., Ivison et al. 2002), the "$F_\nu(24\mu m)/F_\nu(R) \gtrsim 1000$" definition for DOGs translates to "$lg(S_{24\mu}/S_i) \gtrsim 2.6$" in Fig. 14. Among the 12 X-ray detected secure AzTEC counterpart sources with sufficient optical and Spitzer data to be included in this analysis, nearly equal numbers of SMGs fall on either side of this division line. One significant difference is that 9 X-ray detected AzTEC sources fall on the optically faint side (above the dotted line), while only 3 X-ray detected AzTEC sources (including the low-z source AzTEC/GS20) are found on the optically bright side. This trend is consistent with the suggestion by Fiore et al. that many of these dust-obscured galaxies host a Compton-thick AGN. However, there are just as many AzTEC sources undetected in the X-ray above the division line. Given that the observed X-ray emission can be largely accounted for by the starburst activity in many cases (see below and Alexander et al. 2005), the significance of a higher frequency of X-ray detection among these optically faint SMGs is not entirely clear.

6.3 X-ray

The 2 & 4 Ms *Chandra* X-ray surveys of the two GOODS fields (Alexander et al. 2003; Luo et al. 2008; Xue et al. 2011; Johnson et al. 2011) are some of the deepest X-ray data available and thus offers the best opportunity to determine X-ray properties of all types of extragalactic sources. A cross-correlation of the AzTEC and *Chandra* X-ray catalogue has shown that 16 (out of 48) and 8 (out of 40) AzTEC sources in the GOODS-South and North fields have an X-ray source within $6''$ of the AzTEC centroid positions (Johnson et al. 2011). Given the low density of X-ray sources, these coincidence are highly statistically significant. On the other hand, only a subset of these X-ray sources are robust counterparts, and another physical link such as the clustering of massive galaxies (e.g., Almaini et al. 2003) must play a role.

The derived 2-10 keV X-ray luminosity of these *Chandra* sources favor the AGN-origin for the observed X-ray emission. Examining the X-ray properties of faint radio sources in the Hubble Deep Field (North), Bauer et al. (2002) found that the linear correlation between X-ray luminosity and 1.4 GHz radio luminosity density of late type galaxies extends to luminous X-ray detected emission line galaxies at intermediate redshift, suggesting both the X-ray and radio processes are associated with star formation activities. Persic et al. (2004) have shown that the integrated emission from high-mass X-ray binaries (HMXBs) can offer a natural explanation for the observed correlation, and given their short lifetime the measured X-ray luminosity can offer an *instantaneous snapshot* of the ongoing star formation rate. Since HMXBs also display a characteristic hard X-ray spectrum, the hardness ratio of the observed X-ray emission does not provide a unique probe of AGN activity (e.g., Fiore et al. 2008, – see § 6.2). On the other hand, X-ray luminosity of these *Chandra* sources associated with AzTEC detection ranges between $L_X(2.0-10\ keV) = 10^{42}$ and 10^{43} erg s^{-1}. When converted to a SFR using the relation given by Persic et al. (2004), their inferred SFR ranges between 10^3 and $10^4 M_\odot$ yr^{-1}, exceeding the SFR derived from their UV and IR properties (see Fig. 9). A fainter X-ray source with 2-10 keV luminosity of 10^{42} ergs s^{-1} can be either a low luminosity AGN or an SMG with a $SFR = 10^3 M_\odot$ yr^{-1}, but any source with a higher X-ray luminosity would require a significant AGN contribution (see Johnson et al. 2011).

One intriguing trend found is that the fraction of robust AzTEC counterparts that are also *Chandra*-detected X-ray sources is higher for the brighter AzTEC sources. The 30% (7 and 8 out of 25) of the brightest AzTEC sources in the GOODS-South and GOODS-North fields are detected individually as a *Chandra* X-ray source, and an increasing AGN activity may be associated with the most luminous AzTEC sources. In the same vein, the number of candidate *Chandra* counterpart in the GOODS-South field did *not* change from the 2 Ms catalog to 4 Ms catalog, and the greater depth of the X-ray data had curiously little impact. The higher frequency of X-ray counterpart in the GOODS-South field (16/48 vs. 8/40) may reflect the cosmic variance in these two relatively small size fields. A more detailed discussion of the X-ray properties of AzTEC sources is presented elsewhere (Johnson et al. 2011).

The high detection rate for the AzTEC sources in the X-ray bodes well for coeval mass growth scenarios for the stellar component and the central supermassive black hole (SMBH) designed to explain the apparent correlation between the central blackhole mass and stellar velocity dispersion ("M-σ relation" – Magorrian et al. 1998; Ferrarese & Merritt 2000; Gebhardt et al. 2000). For example, through detailed numerical modeling, Narayanan et al. (2010b,a) have shown that a rapid build-up of stellar mass and the growth of the central supermassive black hole can be achieved through a merger-driven starburst, and can reproduce the observed properties of SMGs and dust-obscured QSOs. Winds driven by the starburst and the AGN activity can effectively disrupt the central concentration of gas and dust, driving the evolution of such objects from an SMG phase to a QSO phase (Narayanan et al. 2008).

A natural consequence of such a scenario is that a massive stellar galaxy with a maturing young stellar population would emerge unobscured as the central AGN begins to dominate the overall energetics. As the feedback process starts to clear out the obscuring dust and gas, the central AGN would also become more detectable in the X-ray, UV, and optical bands, marking the beginning of the classical QSO phase. However, the X-ray detected AzTEC sources in the optical and near-IR bands span the entire observed range of brightness, indistinguishable from the X-ray undetected sources in Fig. 6. The $i - K$ colors of the X-ray detected sources are also indistinguishable from the others, suggesting that either (1) the X-ray detection does *not* signal the emergence of the central AGN as the dominant energy source or (2) additional complexity is required in the SMG-QSO evolution model.

By analyzing the properties of a sample of $z \approx 2$ SMGs exhibiting broad Hα and Hβ emission lines, Alexander et al. (2008) have estimated their black hole mass to be $\gtrsim 3$ times smaller than those found in comparable mass normal galaxies in the local universe, and $\gtrsim 10$ times smaller than those predicted for $z \approx 2$ luminous quasars and radio galaxies. Based on this evidence, they argued that the growth of the black hole lags that of the host galaxy in SMGs. We find only marginal evidence for AGN contribution to the near-IR (Figs. 12 & 13) and mid-IR (Fig. 14) SEDs for the robust AzTEC sources, even among those detected in the X-ray. The spectral decomposition and the analysis of the emission, absorption, and continuum features in the *Spitzer* IRS spectra of SMGs by Pope et al. (2008a), Menéndez-Delmestre et al. (2009), and Murphy et al. (2009) have found that a starburst dominates the luminosity in the large majority of cases, even when the sample is selected to have AGN-like colors (Coppin et al. 2010b). A consistent trend emerging from these multiwavelength data analyses is that dust-obscured starburst activity can account for most of the luminosity in SMGs, with little or only a minor contribution from AGNs.

7 SUMMARY AND DISCUSSION

Taking advantage of some of the deepest imaging and photometry data and extensive spectroscopic information in the GOODS-South field, we searched for counterparts to the 48 AzTEC sources found in the deep 1.1 mm wavelength survey by Scott et al. (2010), using a P-statistic analysis involving VLA 1.4 GHz, Spitzer/MIPS 24 μm, and IRAC catalogs, combined with cross identification with LABOCA 870 μm sources. Robust ($P \leqslant 0.05$) and tentative ($0.05 < P \leqslant 0.20$) counterpart candidates are found for 27 and 14 AzTEC GOODS-South sources, respectively. Five of the sources (10%) have two robust counterparts, supporting the idea that these SMGs are strongly clustered and/or confused. A spectroscopic redshift is available for 12 robust counterparts and 12 tentative counterparts while photometric redshifts based on rest-frame UV-to-optical and radio-millimetric SED analysis are available for the remainder. Stellar mass (M_*) and SFR_{UV} are derived by modeling the observed optical and *Spitzer* IRAC photometry while SFR_{IR} is derived by analyzing the IR, (sub)millimetre, and radio photometry using theoretical templates. To improve the statistics of the subsequent analysis, we applied the same counterpart identification and SED analysis to the

AzTEC 1.1mm sources identified in the GOODS-North field (Perera et al. 2008; Downes et al. 2011).

Estimates of the redshift distribution of AzTEC-GOODS sources are constructed by combining spectroscopic redshifts with UV+optical and radio-millimetric photometric redshifts, and these two redshift distributions agree well with each other as shown in Figure 4. Our analysis shows that 80% of AzTEC sources are at $z \geqslant 2$, with a median redshift of $z_{med} \sim 2.6$, and there is a significant high-redshift tail with 20% of AzTEC sources at $z \geqslant 3.3$. These distributions are quite different from the commonly cited SMG redshift distribution of Chapman et al. (2005), primarily at the low redshift end. The SHADES survey redshift distribution by Aretxaga et al. (2007) is in better agreement with our redshift distribution derived from the AzTEC GOODS surveys, and like ours, is missing the low-redshift tail seen in Chapman et al. (2005). Complete CO spectroscopic redshift surveys using the LMT and ALMA will be able to accurately determine the SMG redshift distribution by overcoming the large number of systematic biases inherent in all of these analyses.

An examination of the rest-frame UV and optical photometry for the securely identified AzTEC sources shows a nearly 10 magnitude (a factor of 10^4 in flux density) spread in the $i-$ and $K-$band photometry and extremely red colors spanning $i - K$ color between 0 and +6. There are a small minority of SMGs that are bright in the rest frame UV bands, overlapping with star forming galaxy population previously identified in the rest-frame UV searches. On the other hand, AzTEC GOODS sources are on average quite red and faint, with a median brightness of $i = 25.3$ and $K = 22.6$, and a large fraction of AzTEC sources are entirely missed by previous surveys of star forming galaxies. Examining the observed scatter in the $i-K$ color, we deduce that there is at least a factor of 10 variation in the intrinsic rest frame optical luminosity among these SMGs.

A Hubble diagram of the observed IRAC 3.6 μm flux density shows that these AzTEC-GOODS sources are some of the most luminous galaxies in the rest-frame optical bands at $z \geqslant 2$, offering a good explanation as to why nearly every SMG identified with interferometric observations shows a relatively bright IRAC counterpart. Modeling of the observed rest-frame UV and optical SEDs shows that the stellar masses are rather large, $M_* = (1\text{-}30) \times 10^{10} M_\odot$, with a surprisingly large $SFR_{UV} \gtrsim 100 - 1000\, M_\odot\, \mathrm{yr}^{-1}$ for about 50% of these galaxies. In comparison, SFR_{IR} derived from modeling the IR to radio SED covers a relatively tight range of 200-2000 $M_\odot\, \mathrm{yr}^{-1}$, independent of the redshift or stellar mass. Whether a galaxy has been detected in the X-ray by *Chandra* appears to have no influence on the derived M_*, SFR_{UV}, SFR_{IR}, and SFR_{UV}/SFR_{IR} ratio, and the presence of an X-ray bright AGN appears to have relatively little influence on these quantities.

These AzTEC-GOODS sources have a specific star formation rate 10-100 times higher ($SSFR \approx$ 1-100 Gyr^{-1}) than similar stellar mass galaxies at $z = 0$, and they extend the previously observed rapid rise of $SSFR$ with redshift ($SSFR \propto (1+z)^5$, Damen et al. 2009) to $z = 2-5$. More importantly, *all* of the AzTEC-GOODS sources have a $SSFR$ above the inverse Hubble time line, indicating that they have a current SFR high enough to have built up their entire stellar mass within the Hubble time at their observed redshift.

This might be the best quantitative evidence yet that we are witnessing these galaxies during their rapid mass build-up phase. The flat $SSFR$ as a function of redshift we deduce contradicts the model prediction of a tight M_*-SFR relation based on cosmological hydrodynamic simulations incorporating galactic outflows (Davé et al. 2010, 2011). However, AzTEC sources with $M_* \gtrsim 10^{10.5} M_\odot$ appear to follow this model prediction, and one plausible explanation is that a different mechanism is operating for the lower mass SMGs, leading to a 10 times higher $SSFR$. Alternatively, they are seen at a different phase of rapid mass build-up. Much of the cosmic IR background (CIRB) is expected to be associated with fainter sources below the confusion limit of our AzTEC surveys, and their number counts can offer an important constrain to the evolution model for SMGs (Granato et al. 2004; Baugh et al. 2005; Rowan-Robinson 2009). It still remains to be shown whether these are young, lower mass galaxies seen in their rapid formation epoch or the simmering activities in more massive galaxies that have already undergone an SMG-like rapid build-up phase in even earlier epochs.

Lastly, we examine the evidence for luminous AGNs in these systems using three different diagnostic tests: (1) the *Spitzer* IRAC color-color diagram; (2) optical-IRAC-MIPS colors; and (3) X-ray luminosity. We find only marginal evidence for AGN contribution to the near-IR (Figs. 12 & 13) and mid-IR (Fig. 14) SEDs for the robust AzTEC sources, even among those detected in the X-ray. A consistent trend emerging from this multiwavelength data analysis and similar studies by other groups is that dust-obscured starburst activity can account for most of the luminosity in submm/mm-selected galaxies, with little or only a minor contribution from AGNs.

REFERENCES

Akiyama M., 2005, ApJ, 629, 72

Alexander D. M., Bauer F. E., Chapman S. C., Smail I., Blain A. W., Brandt W. N., Ivison R. J., 2005, ApJ, 632, 736

Alexander D. M., et al., 2003, AJ, 126, 539

Alexander D. M., et al., 2008, AJ, 135, 1968

Almaini O., et al., 2003, MNRAS, 338, 303

Almeida C., Baugh C. M., Lacey C. G., 2011, MNRAS

Aretxaga I., et al., 2003, MNRAS, 342, 759

Aretxaga I., et al., 2007, MNRAS, 379, 1571

Austermann J. E., et al., 2010, MNRAS, 401, 160

Balestra I., et al., 2010, A&A, 512, id.A12

Barger A. J., Cowie L. L., Richards E. A., 2000, AJ, 119, 2092

Barger A. J., Cowie L. L., Sanders D. B., Fulton E., Taniguchi Y., Sato Y., Kawara K., Okuda H., 1998, Nature, 394, 248

Barger A. J., Cowie L. L., Smail I., Ivison R. J., Kneib J.-P., 1999, AJ, 117, 2656

Bauer A. E., Drory N., Hill G. J., Feulner G., 2005, ApJ, 621, L89

Bauer F. E., Alexander D. M., Brandt W. N., Hornschemeier A. E., Vignali C., Garmire G. P., Schneider D. P., 2002, AJ, 124, 2351

Baugh C. M., Lacey C. G., Frenk C. S., Granato G. L., Silva L., Bressan A., Benson A. J., Cole S., 2005, MNRAS, 356, 1191

Bell E. F., et al., 2004, ApJ, 608, 752

Bell E. F., Zheng X. Z., Papovich C., Borch A., Wolf C., Meisenheimer K., 2007, ApJ, 663, 834

Bertoldi F., et al., 2000, A&A, 360, 92

Bertoldi F., et al., 2007, ApJS, 172, 132

Biggs A. D., et al., 2011, MNRAS

Blain A. W., Chapman S. C., Smail I., Ivison R., 2004, ApJ, 611, 725

Blain A. W., Smail I., Ivison R. J., Kneib J.-P., Frayer D. T., 2002, Physics Reports, 369, 111

Borys C., Chapman S., Halpern M., Scott D., 2003, MNRAS, 344, 385

Borys C., et al., 2004, MNRAS, 355, 485

Calzetti D., et al., 2000, ApJ, 533, 682

Capak P., et al., 2008, ApJ, 681, L53

Carilli C. L., et al., 2001, ApJ, 555, 625

Carilli C. L., Yun M. S., 1999, ApJ, 513, L13

Carilli C. L., Yun M. S., 2000, ApJ, 530, 618

Casey C. M., et al., 2011, MNRAS, 411, 2739

Chapin E. L., et al., 2009, MNRAS, 398, 1793

Chapin E. L., et al., 2011, MNRAS, 411, 505

Chapman S. C., Blain A. W., Smail I., Ivison R. J., 2005, ApJ, 622, 772

Chapman S. C., Richards E. A., Lewis G. F., Wilson G., Barger A. J., 2001, ApJ, 548, L147

Chen Y., Lowenthal J. D., Yun M. S., 2010, ApJ, 713, 1385

Clements D. L., Dunne L., Eales S., 2010, submitted to MNRAS, 403, 274

Clements D. L., et al., 2008, MNRAS, 387, 247

Condon J. J., 1992, ARA&A, 30, 575

Cooray A., et al., 2010, A&A, 518, L22

Coppin K., et al., 2006, MNRAS, 372, 1621

Coppin K., et al., 2009, MNRAS, 395, 1905

Coppin K., et al., 2010a, MNRAS, 407, L103

Coppin K., et al., 2010b, ApJ, 713, 503

Cowie L. L., Barger A. J., Kneib J.-P., 2002, AJ, 123, 2197

Cowie L. L., Sangaila A., Hu E. M., Cohen J. G., 1996, AJ, 112, 839

Daddi E., Cimatti A., Renzini A., Fontana A., Mignoli M., Pozzetti L., Tozzi P., Zamorani G., 2004, ApJ, 617, 746

Daddi E., et al., 2007, ApJ, 670, 156

Daddi E., et al., 2009, ApJ, 694, 1517

Damen M., et al., 2009, ApJ, 690, 937

Dannerbauer H., Lehnert M. D., Lutz D., Tacconi L., Bertoldi F., Carilli C., Genzel R., Menten K., 2002, ApJ, 573, 473

Dannerbauer H., Walter F., Morrison G., 2008, ApJ, 673, L127

Davé R., et al., 2010, MNRAS, 404, 1355

Davé R., Oppenheimer B., Finlator K., 2011, submitted to MNRAS

Devlin M. J., et al., 2009, Nature, 458, 737

Dey A., et al., 2008, ApJ, 677, 943

Diaz-Sanchez A., Villo-Perez I., Perez-Garrido A., Rebolo R., 2007, MNRAS, 377, 516

Downes A. J. B., Peacock J. A., Savage A., Carrie D. R., 1986, MNRAS, 218, 31

Downes T. P., Welch D., Scott K., Austermann J., Wilson G. W., 2011, submitted to MNRAS

Dunlop J. S., et al., 2010, submitted to MNRAS

Dunne L., et al., 2009, MNRAS, 394, 3

Dye S., et al., 2008, MNRAS, 386, 1107

Eales S., Bertoldi F., Ivison R., Carilli C., Dunne L., Owen F., 2003, MNRAS, 344, 169

Eales S., Lilly S., Gear W., Dunne L., Bond J. R., Hammer F., Le Fèvre O., Crampton D., 1999, ApJ, 515, 518

Eales S., Lilly S., Webb T., Dunne L., Gear W., Clements D., Yun M., 2000, AJ, 120, 2244

Efstathiou A., Rowan-Robinson M., 2003, MNRAS, 343, 322

Efstathiou A., Rowan-Robinson M., Siebenmorgen R., 2000, MNRAS, 313, 734

Elbaz D., et al., 2007, A&A, 468, 33

Erb E., et al., 2006, ApJ, 647, 128

Erickson N., Narayanan G., Goeller R., Grosslein R., 2007, in Baker A. J., Glenn J., Harris A. I., Mangum J. G., Yun M. S., eds, From Z-Machines to ALMA: (Sub)Millimeter Spectroscopy of Galaxies Vol. 375 of Astronomical Society of the Pacific Conference Series, An Ultra-Wideband Receiver and Spectrometer for 74–110 GHz. pp 71–+

Faber S. M., et al., 2007, ApJ, 665, 265

Feigelson E. D., Nelson P. I., 1985, ApJ, 293, 192

Ferrarese L., Merritt D., 2000, ApJ, 539, L9

Feulner G., Gabasch A., Salvato M., Drory N., Hopp U., Bender R., 2005, ApJ, 633, L9

Fioc M., Rocca-Volmerange B., 1997, A&A, 326, 950

Fiore F., et al., 2008, ApJ, 672, 94

Fixsen D. J., Dwek E., Mather J. C., Bennett C. L., Shafer R. A., 1998, ApJ, 508, 123

Fox M. J., et al., 2002, MNRAS, 331, 839

Frayer D. T., Smail I., Ivison R. J., Scoville N. Z., 2000, AJ, 120, 1668

Gawiser E., et al., 2006, ApJS, 162, 1

Gebhardt K., et al., 2000, ApJ, 539, L9

Giavalisco M., et al., 2004, ApJ, 600, L93

Goldader J. D., Meurer G., Heckman T. M., Siebert M., Sanders D. B., Calzetti D., Steidel C. C., 2002, ApJ, 568, 651

Granato G. L., De Zotti G., Silva L., Bressan A., Danese L., 2004, ApJ, 600, 580

Greve T. R., Ivison R. J., Bertoldi F., Stevens J. A., Dunlop J. S., Lutz D., Carilli C. L., 2004, MNRAS, 354, 779

Greve T. R., Pope A., Scott D., Ivison R. J., Borys C., Conselice C. J., Bertoldi F., 2008, MNRAS, 389, 1489

Hainline L. J., Blain A. W., Smail I., Frayer D. T., Chapman S. C., Ivison R. J., Alexander D. M., 2009, ApJ, 699, 1610

Hatsukade B., et al., 2010, ApJ, 711, 974

Hayward C. C., et al., 2011, submitted to ApJ

Holland W. S., et al., 1999, MNRAS, 303, 659

Houck J. R., et al., 2004, ApJS, 154, 18

Huang J.-S., et al., 2009, ApJ, 700, 183

Hughes D. H., et al., 1998, Nature, 394, 241

Hughes D. H., et al., 2002, MNRAS, 335, 871

Ikarashi S., et al., 2011, submitted to MNRAS

Iono D., et al., 2006, ApJ, 640, L1

Ivison R., et al., 2010, A&A, 518, L31

Ivison R. J., et al., 2000, MNRAS, 315, 209

Ivison R. J., et al., 2002, MNRAS, 337, 1

Ivison R. J., et al., 2004, ApJS, 154, 124

Ivison R. J., et al., 2007, MNRAS, 380, 199

Johnson S. P., Wilson G. W., Wang Q. D., Williams C. C., Scott K., Yun M. S., Lowenthal J., 2011, submitted to MNRAS

Kauffmann G., et al., 2003, MNRAS, 341, 33

Kaviani A., Haehnelt M. G., Kauffmann G., 2003, MNRAS, 340, 739

Kellermann K. I., Fomalont E. B., Mainieri V., Padovani P., Rosati P., Shaver P., Tozzi P., Miller N., 2008, ApJS, 179, 71

Kennicutt Jr. R. C., 1998, ARA&A, 36, 189

Keres D., Katz N., Weinberg D. H., Davé R., 2005, MN-RAS, 363, 2

Kriek M., et al., 2008, ApJ, 677, 219

Lacki B., Thompson T., 2010, ApJ, 717, 196

Lacy M., et al., 2004, ApJS, 154, 166

Laidler V. G., et al., 2007, PASP, 119, 1325

Laurent G. T., et al., 2005, ApJ, 623, 742

Le Fevre O., et al., 2004, A&A, 428, 1043

Le Floc'h E., et al., 2005, ApJ, 632, 169

Lilly S. J., et al., 1999, ApJ, 518, 641

Luo B., et al., 2008, ApJS, 179, 19

Lutz D., et al., 2001, A&A, 378, 70

Lutz D., et al., 2005, ApJ, 625, L83

Madau P., 1995, ApJ, 441, 18

Magnelli B., et al., 2009, A&A, 496, 57

Magnelli B., et al., 2011, A&A, 528, A35

Magorrian J., et al., 1998, AJ, 115, 2285

Maraston C., et al., 2010, MNRAS, 407, 830

Martinez-Sansigre A., Lacy M., Sajina A., Rawlings S., 2008, ApJ, 674, 676

Menéndez-Delmestre K., et al., 2007, ApJ, 655, L65

Menéndez-Delmestre K., et al., 2009, ApJ, 699, 667

Michalowski M., Hjorth J., Watson D., 2010, A&A, 514, A67

Mignoli M., et al., 2005, A&A, 437, 883

Miller N. A., Fomalont E. B., Kellermann K. I., Mainieri V., Norman C., Padovani P., Rosati P., Tozzi P., 2008, ApJS, 179, 114

Murphy E. J., Chary R.-R., Alexander D. M., Dickinson M., Magnelli B., Morrison G., Pope A., Teplitz H. I., 2009, ApJ, 698, 1380

Narayanan D., et al., 2008, ApJS, 176, 331

Narayanan D., et al., 2010a, MNRAS, 407, 1701

Narayanan D., et al., 2010b, MNRAS, 401, 1613

Norris R. P., et al., 2006, AJ, 132, 2409

Pannella M., et al., 2009, ApJ, 698, L116

Pei Y. C., Fall S. M., Hauser M. G., 1999, ApJ, 522, 604

Perera T. A., et al., 2008, MNRAS, 391, 1227

Persic M., Rephaeli Y., Braito V., Cappi M., Della Ceca R., Franceschini A., Gruber D. E., 2004, A&A, 419, 849

Pope A., Chary R.-R., 2010, ApJ, 715, L171

Pope A., et al., 2006, MNRAS, 370, 1185

Pope A., et al., 2008a, ApJ, 675, 1171

Pope A., et al., 2008b, ApJ, 689, 127

Popesso P., et al., 2009, A&A, 494, 443

Retzlaff J., et al., 2010, A&A 511, 50

Rieke G., et al., 2004, ApJS, 154, 25

Rigopoulou D., Mainieri V., Almaini O., Alonso-Herrero A., Huang J.-S., Hasinger G., Rieke G., Dunlop J., Lehmann I., 2009, MNRAS, 400, 1199

Rowan-Robinson M., 2009, MNRAS, 394, 117

Rowan-Robinson M., 2010, MNRAS

Salimbeni S., Fontana A., Giallongo E., Grazian A., Menci N., Pentericci L., Santini P., 2009, in Probing Stellar Populations out to the Distant Universe Vol. 1111 of AIP Conference Proceedings, Uncertainties and Systematic Effects on the estimate of stellar masses in high z galaxies. pp 207–211

Sanders D. B., Mirabel I. F., 1996, ARA&A, 34, 749

Scott K. S., et al., 2008, MNRAS, 385, 2225

Scott K. S., et al., 2010, MNRAS, 405, 2260

Scott S. E., et al., 2002, MNRAS, 331, 817

Serjeant S., et al., 2003, MNRAS, 344, 887

Silverman J. D., et al., 2010, ApJS, in press, 191, 124

Smail I., Chapman S. C., Blain A. W., Ivison R. J., 2004, ApJ, 616, 71

Smail I., Ivison R. J., Blain A. W., 1997, ApJ, 490, L5

Smail I., Ivison R. J., Blain A. W., Kneib J.-P., 2002, MN-RAS, 331, 495

Smolcic V., et al., 2008, ApJS, 177, 14

Stern D., et al., 2005, ApJ, 631, 166

Strazzullo V., Pannella M., Owen F. N., Bender R., Morrison G. E., Wang W.-H., Shupe D. L., 2010, ApJ, 714, 1305

Swinbank K., et al., 2010, MNRAS, 405, 234

Szokoly G. P., et al., 2004, ApJS, 155, 271

Tacconi L. J., et al., 2008, ApJ, 680, 246

Tamura Y., et al., 2010, ApJ, 724, 1270

Treister E., et al., 2009, ApJ, 693, 1713

Tremonti C. A., et al., 2004, ApJ, 613, 898

Valiante E., et al., 2007, ApJ, 660, 1060

van Dokkum P. G., et al., 2008, ApJ, 677, L5

Vanzella E., et al., 2005, A&A, 434, 53

Vanzella E., et al., 2006, A&A, 454, 423

Vanzella E., et al., 2008, A&A, 478, 83

Vieira J. D., et al., 2010, ApJ, 719, 763

Wang R., et al., 2007, ApJ, 134, 617

Wang R., et al., 2008, ApJ, 687, 848

Wang W.-H., Cowie L. L., Barger A. J., 2004, ApJ, 613, 655

Wang W.-H., Cowie L. L., Barger A. J., Williams J. P., 2011, ApJ, 726, L18

Wang W.-H., Cowie L. L., van Saders J., Barger A. J., Williams J. P., 2007, ApJ, 670, L89

Webb T. M., et al., 2003a, ApJ, 587, 41

Webb T. M., et al., 2003b, ApJ, 597, 680

Weiss A., et al., 2009, ApJ, 707, 1201

Williams C. C., et al., 2011, ApJ, 733, 92

Wuyts S., et al., 2009, ApJ, 706, 885

Xue Y. Q., et al., 2011, submitted to ApJ

Younger J. D., et al., 2007, ApJ, 671, 1531

Younger J. D., et al., 2008, MNRAS, 387, 707

Younger J. D., et al., 2009, ApJ, 704, 803

Yun M. S., Carilli C. L., 2002, ApJ, 568, 88

Yun M. S., Carilli C. L., Kawabe R., Tutui Y., Kohno K., Ohta K., 2002, ApJ, 528, 171

Yun M. S., et al., 2008, MNRAS, 389, 333

Zheng X. Z., et al., 2007, ApJ, 661, L41

APPENDIX A: NOTES ON INDIVIDUAL SOURCES

AzTEC/GS1. There is one clear, robust counterpart (GS1a in Table 2), which is a radio source found 4.8″ north of AzTEC/GS1 ($P_{1.4} = 0.045$). This faint radio source has an IRAC/MIPS counterpart ($P_{24\mu} = 0.161$), which is also a *Chandra*/X-ray source. This source has a red IRAC color with $[3.6\mu m] - [4.5\mu m] = +0.37$ ($P_{color} = 0.133$), similar to the AzTEC sources identified using submillimetre interferometry (Younger et al. 2007; Yun et al. 2008). The 870 μm LABOCA source LESS J033211.3−275210 ($S_{870\mu} = 9.2 \pm 1.2$ mJy) position is only 2.1″ away from GS1a, and Biggs et al. (2011) also identify GS1a as the robust counterpart. No spectroscopic redshift is available for this extremely faint optical source ($i > 23.5$, $K > 22.9$), and it is likely a high redshift ($z \geqslant 3$) source with $z_{opt} = 2.96 \pm 0.45$ and $z_{MR} = 3.56^{+0.66}_{-1.20}$.

AzTEC/GS2.1. There are two radio sources (GS2.1a & GS2.1b) within the 4.5″ search radius, each with a high likelihood of being the AzTEC counterpart. The western-most source GS2.1a with a red IRAC color ($[3.6\mu m] - [4.5\mu m] = +0.38$) is a robust identification ($P_{1.4} = 0.001$). The 870 μm LABOCA source LESS J033219.0−275219 ($S_{870\mu} = 9.1 \pm 1.2$ mJy) position is only 4.8″ away from GS2.1a. The adjacent, second faint radio source GS2.1b is an extremely rare example of a faint radio source without any counterpart in the IRAC and MIPS images. Both radio sources are formally considered robust counterparts by our analysis and by Biggs et al. (2011). There are two additional faint radio sources just outside the search radius, making this an exceptionally crowded field in the radio band. These two more distant radio sources have the same spectroscopic redshift of $z = 1.097$ (Le Fevre et al. 2004; Norris et al. 2006), and their blue IRAC color, $[3.6\mu m] - [4.5\mu m] = -0.27$ suggests that they are indeed foreground sources. The catalog position for the BLAST 250 μm source 59 (Dunlop et al. 2010) is located near the peak of the AzTEC/GS2 contours but between the two deconvolved components AzTEC/GS2.1 and AzTEC/GS2.2. A third potential counterpart, GS2.1c, identified by MIPS 24 μm detection is only 3.9″from the AzTEC centroid; however it has a blue IRAC color ($[3.6\mu m] - [4.5\mu m] = -0.32$) with a spectroscopic redshift of $z = 0.644$, and is likely a foreground object.

AzTEC/GS2.2. There are no radio sources within 15″ of AzTEC/GS2.2. The MIPS 24 μm source GS2.2a is a potential counterpart with $P_{24\mu} = 0.212$ with a blue IRAC color ($[3.6\mu m] - [4.5\mu m] = -0.23$) and a spectroscopic redshift of $z = 1.046$ (Popesso et al. 2009). Therefore, it is likely a member of the foreground $z = 1.10$ cluster

GCL J0332.2−2752 ($\sigma_v = 433$ km/s; Diaz-Sanchez et al. 2007) whose center is located only $\sim 20''$ to the northeast, at $\alpha = 03^h 32^m 17.5^s$ and $\delta = -27°52'32''$. This MIPS source is blended with a second IRAC source located 3″ to the southwest, GS2.2b, which has a red IRAC color ($[3.6\mu m] - [4.5\mu m] = +0.26$; $P_{color} = 0.390$). GS2.2b is also a BzK galaxy and thus is an actively star forming system. The IRAC source GS2.2c is another BzK galaxy with a red IRAC color ($[3.6\mu m] - [4.5\mu m] = +0.10$) and is an interesting alternative counterpart, though $P_{color} = 0.439$. The closest 870 μm LABOCA source LESS J033217.6−275230 ($S_{870\mu} = 6.3 \pm 1.3$ mJy) position is 15″ northeast of the AzTEC centroid, nearly centered on the $z = 1.1$ cluster. The position of AzTEC/GS2.2, however, is very uncertain as it is blended with AzTEC/GS2.1, so the counterpart identification is highly problematic.

AzTEC/GS3. The faint IRAC source GS3a ($S_{1.4GHz} = 40.7 \pm 6.5$ μJy; $P_{1.4} = 0.045$) is also a MIPS 24 μm source with a red IRAC color ($[3.6\mu m] - [4.5\mu m] = +0.37$; $P_{color} = 0.174$). The 870 μm LABOCA source LESS J033248.1−275414 ($S_{870\mu} = 8.8 \pm 1.2$ mJy) is only 2.4″ away from GS3a, leading Biggs et al. (2011) to conclude this source as a secure counterpart as well. Dunlop et al. (2010) also identified GS3a as the counterpart to the 250 μm BLAST source 593 and estimated a redshift $z > 2.5$ for this optically invisible source. Our radio-mm photometric redshift of $z_{MR} = 3.09^{+0.55}_{-1.11}$ supports this high-z hypothesis. There is a faint red IRAC source, GS3b, which is is also a tentative detection that cannot be ruled out.

AzTEC/GS4. There is only one red IRAC source (GS4a; $P_{color} = 0.070$) within the 6.5″ search radius. It is a faint radio emitter ($S_{1.4GHz} = 25.4 \pm 6.5$ μJy, $P_{1.4} = 0.021$). There are two other radio sources within 17″ from the AzTEC position, but GS4a is the only source falling within the error circle of the 870 μm LABOCA source LESS J033249.2−274246 ($S_{870\mu} = 8.8 \pm 1.2$ mJy). Therefore GS4a is a robust counterpart for the AzTEC source although it is only a tentative counterpart for the LABOCA source (Biggs et al. 2011). This is another high-z candidate source with $z_{opt} = 3.37 \pm 0.25$ and $z_{MR} = 3.53^{+0.57}_{-1.27}$.

AzTEC/GS5. There is a single tentative counterpart within the 7.1″ search radius from the AzTEC/GS5 position. However, the AzTEC contours are elongated in the east-west direction, joining the two VLA radio sources GS5a & GS5b. Both radio sources have red IRAC counterparts, and both sources may contribute to the AzTEC emission. The 870 μm LABOCA source LESS J033150.8−274438 ($S_{870\mu} = 3.9 \pm 1.4$ mJy) is located only 4.1″ away from GS5a (also a *Chandra* X-ray source), and Biggs et al. (2011) and Chapin et al. (2011) also identify GS5a as the secure counterpart to the LABOCA source. Casey et al. (2011) reported a spectroscopic redshift of $z = 1.599$ for GS5a based on some absorptions features, and this redshift is further supported by the 9 hr long integration VLT spectrum by Silverman et al. (2010).

AzTEC/GS6. The IRAC/MIPS source GS6b is located only 0.4″ from the AzTEC/GS6 centroid. However, its blue IRAC color ($[3.6\mu m] - [4.5\mu m] = -0.23$) and spectroscopic redshift of $z = 1.102$ (Stern et al., in prep) suggest that GS6b is likely a foreground object. At a distance of 12.4″,

the IRAC/MIPS source GS6a is located outside the 7.5″ formal search radius for a counterpart, but it has very red IRAC color ($[3.6\mu m] - [4.5\mu m] = +0.45$) and is a faint radio source ($S_{1.4GHz} = 31.0 \pm 6.3$ μJy; $P_{1.4} = 0.268$). Biggs et al. (2011) identify GS6a as the robust counterpart for the 870 μm LABOCA source LESS J033225.7−275228 ($S_{870\mu} = 5.8 \pm 1.4$ mJy) located 6.2″ away, and this galaxy is likely the primary counterpart to the AzTEC source as well.

AzTEC/GS7. The red IRAC/MIPS source GS7a is the only radio source within the 8.7″ search radius ($S_{1.4GHz} = 51.2 \pm 6.4$ μJy; $P_{1.4} = 0.126$). Therefore, it is considered a tentative counterpart to AzTEC/GS7. The spectroscopic redshift of GS7a, which is also identified as a *Chandra* X-ray source, is $z = 2.676$, in excellent agreement with its radio-mm photometric redshift of $z_{MR} = 2.56^{+0.52}_{-0.92}$. The 870 μm LABOCA source LESS J033213.6−275602 ($S_{870\mu} = 9.1 \pm 1.2$ mJy) is located only 4.2″ away, and Biggs et al. (2011) also identify GS7a as a robust counterpart. A second possible counterpart, GS7b, is a red IRAC/MIPS source ($P_{24\mu} = 0.151$, $P_{color} = 0.168$) located on the other side of the AzTEC centroid and may contribute to the observed 1100 μm emission.

AzTEC/GS8. There is a single robust radio counterpart GS8a, 4.4″ from the AzTEC centroid position with $P_{1.4} = 0.038$. The IRAC/MIPS counterpart GS8a also has a red IRAC color ($[3.6\mu m] - [4.5\mu m] = +0.33$) and relatively bright MIPS 24 μm emission ($S_{24\mu} = 620$ μJy; $P_{24\mu} = 0.203$). Both Chapin et al. (2011) and Biggs et al. (2011) have identified this $z = 2.252$ galaxy as the counterpart to the 870 μm LABOCA source LESS J033205.1−274652 ($S_{870\mu} = 7.5 \pm 1.2$ mJy), located only 7.7″ away from AzTEC position. The second IRAC/MIPS source GS8b, located 2.9″ from the AzTEC position, is also a plausible MIPS 24 μm counterpart ($P_{24\mu} = 0.089$) with red IRAC color and is also a *Chandra* X-ray source.

AzTEC/GS9. The single tentative radio counterpart ($S_{1.4} = 86.8 \pm 6.6$ μJy; $P_{1.4} = 0.070$) is associated with a red IRAC/MIPS source GS9a, located 6.2″ from the AzTEC centroid position. It is also a *Chandra*-detected X-ray source and should be considered a strong candidate for the AzTEC counterpart. Located only 3.5″ away from the AzTEC centroid, the IRAC/MIPS source GS9b is an intriguing alternate counterpart candidate given its red IRAC color ($[3.6\mu m] - [4.5\mu m] = +0.29$) and MIPS 24 μm emission. If GS9b is the primary source of 1100 μm continuum emission, then it is likely to be a high redshift system as its radio non-detection requires $z_{MR} > 3.3$. Slightly further away is GS9c, also a tentative red IRAC source. No nearby source is found in the 870 μm LABOCA catalog, but the LABOCA map shows a $S/N = 3.0$ peak (3.4 ± 1.2 mJy) at the position of GS9a.

AzTEC/GS10. There is a single robust radio counterpart to AzTEC/GS10, located 5.3″ from the AzTEC centroid ($S_{1.4} = 89.3 \pm 6.4$ μJy; $P_{1.4} = 0.053$). Its red IRAC/MIPS counterpart GS10a ($[3.6\mu m] - [4.5\mu m] = +0.14$) has a reported spectroscopic redshift of $z = 0.0338$ in the GOODS/ESO VIMOS DR1 catalog (Popesso et al. 2009), but the same group revised its redshift to $z = 2.035$ using new data (Balestra et al. 2010). This revised spectroscopic redshift is in excellent agreement with our photomet-

ric redshift, $z_{MR} = 2.03^{+0.41}_{-0.75}$. Another red IRAC source GS10b ($[3.6\mu m] - [4.5\mu m] = +0.04$; $P_{color} = 0.077$), located only 3.2″ away from the AzTEC position, is not detected in the radio or by MIPS. The 870 μm LABOCA source LESS J033207.6−275123 ($S_{870\mu} = 7.6 \pm 1.3$ mJy) is located only 4.3″ away from GS10a, and it is also identified as a robust LABOCA counterpart by Biggs et al. (2011).

AzTEC/GS11. There is a single tentative VLA radio counterpart for this source located 6.5″ from the AzTEC centroid ($S_{1.4} = 46.0 \pm 6.4$ μJy; $P_{1.4} = 0.081$), and it is also a *Chandra* X-ray source. Its IRAC/MIPS counterpart GS11a has a slightly blue color ($[3.6\mu m] - [4.5\mu m] = -0.02$), but the VLT ISAAK $K-$band image (Retzlaff et al. 2010) shows that this IRAC source is a blend of an optically bright ($i = 21.7$) $z = 0.246$ foreground source and an optically faint source second source, which is the radio source. The 250 μm BLAST source 109, located $\sim 30''$ southeast of the AzTEC centroid, is undetected at longer wavelength bands and is identified with a $z = 0.124$ foreground disk galaxy (Dunlop et al. 2010). Our photometric redshift for GS11a, $z_{MR} = 2.50^{+0.52}_{-0.88}$, is completely inconsistent with this identification, and the proposed BLAST counterpart is unlikely to be related to the AzTEC source. No nearby source is found in the 870 μm LABOCA catalog, but the LABOCA map shows a $S/N \sim 3$ peak (3.5 ± 1.2 mJy) at the position of GS11a.

AzTEC/GS12. The most likely counterpart candidate is a faint radio, red IRAC source GS12a located 4.0″ away from the AzTEC position with $[3.6\mu m] - [4.5\mu m] = +0.10$. This $z = 4.762$ galaxy was also identified as the counterpart to the LABOCA 870 μm survey source LESS J033229.3−275619 ($S_{870\mu} = 5.1 \pm 1.4$ mJy) by Coppin et al. (2009) based on its proximity to the LABOCA position and the presence of a $\sim 3\sigma$ radio source. Redshifted CO emission at $z_{CO} = 4.755$ has been reported by Coppin et al. (2010a), lending further support for the counterpart identification.

AzTEC/GS13. There is a high concentration of IRAC/MIPS sources with spectroscopic redshifts between 1.0 and 1.6 in the region surrounding AzTEC/GS13. The most likely counterpart for AzTEC/GS13 is a red IRAC/MIPS source GS13a ($[3.6\mu m] - [4.5\mu m] = +0.24$), located only 2.1″ away from the AzTEC centroid. This source is also a faint radio source with no known spectroscopic redshift. A second IRAC/MIPS sources GS13b is a *Chandra* X-ray source at $z = 1.039$ (Mignoli et al. 2005), but its statistical likelihood of being the AzTEC counterpart is lower (see Table 1). A third candidate counterpart, GS13c, is a faint radio source, but it has a blue IRAC color ($[3.6\mu m] - [4.5\mu m] = -0.25$) and is therefore likely a foreground source. The 250 μm BLAST source 193 is located $\sim 25''$ south of the AzTEC position. Although the low density of the AzTEC and BLAST sources make the chance coincidence of these two sources even at such a substantial separation small, few plausible candidates are found within the BLAST position error circle. No nearby source is found in the 870 μm LABOCA catalog, but the LABOCA map shows a $S/N \sim 3$ peak (3.6 ± 1.2 mJy) near the AzTEC centroid position.

AzTEC/GS14. There are no radio sources within the 9.0″ search radius. The only tentative counterpart is a faint, red IRAC source GS14a ($[3.6\mu m] - [4.5\mu m] = +0.04$; $P_{color} = $

0.083) located only 3.1″ from AzTEC/GS14. Although no nearby source is found in the 870 μm LABOCA catalog, the LABOCA map shows a $S/N \sim 3$ peak (3.3±1.2 mJy) nearly coincident with this position. The previously unpublished redshift of $z = 3.640$ (Keck LRIS spectrum, H. Spinrad, priv. comm.) for GS14a is consistent with its photoz $z_{opt} = 3.50\pm0.30$ and the non-detection in the radio and the MIPS 24 μm bands, similar to the $z = 4.762$ AzTEC/LABOCA source GS12a.

AzTEC/GS15. There are several faint, red IRAC/MIPS sources within the 9.0″ search radius, although they are individually not particularly compelling. The faint radio source GS15a, although 12.7″from the AzTEC centroid, is also a *Chandra* X-ray source and is located 1.4″from the centroid of the LABOCA 870 μm source LESS J033151.5−274552 ($S_{870\mu} = 4.2\pm1.4$ mJy), and GS15a is the secure LABOCA counterpart (Biggs et al. 2011).

AzTEC/GS16. There are two faint radio sources within the counterpart search radius of 10.5″. The red IRAC/MIPS source GS16a ($[3.6\mu m] - [4.5\mu m] = +0.53$) is 6.1″ away from the AzTEC position, and it is a tentative radio counterpart with $P_{1.4} = 0.072$. GS16a is also an X-ray source detected by *Chandra* and has a spectroscopic redshift of $z = 1.719$ (Silverman et al., in prep.). The second radio source GS16b is located slightly further away, 7.9″. Although it is a brighter MIPS 24 μm source, it has a blue IRAC color ($[3.6\mu m]$ - $[4.5\mu m] = -0.29$) and a spectroscopic redshift of $z = 1.017$ (Mignoli et al. 2005), suggesting it is a foreground source. No nearby source is found in the 870 μm LABOCA catalog, but the LABOCA map shows a $S/N \sim 2$ peak near the position of G16a.

AzTEC/GS17. Two plausible IRAC/MIPS sources are found within the 10.5″ search radius. The IRAC/MIPS source GS17a is a faint radio source with $P_{1.4} = 0.007$, making it formally a robust identification. However, it has a blue IRAC color with $[3.6\mu m] - [4.5\mu m] = -0.27$ and is thus likely a foreground object($z_{opt} = 1.01 \pm 0.10$). The IRAC/MIPS source GS17b is another robust identification based on the MIPS detection ($P_{24\mu} = 0.026$) and red IRAC color ($[3.6\mu m] - [4.5\mu m] = +0.19$, $P_{color} = 0.021$), and this *Chandra* detected X-ray source has a photometric redshift of $z = 2.66$ (Silverman et al. 2010). Though slightly further from the AzTEC centroid, GS17c is an interesting alternative possibility: this red IRAC/MIPS source ($[3.6\mu m] - [4.5\mu m] = +0.36$) has optical colors satisfying the BzK criteria for star forming galaxies at high redshifts. There is also a close pair of radio sources, GS17d and GS17e, located 12″north of the AzTEC position; though they are outside the nominal search radius, both have red IRAC colours and remain plausible counterparts to the AzTEC source. No nearby source is found in the 870 μm LABOCA catalog, but the LABOCA map shows a $S/N \sim 3$ emission peak between GS17b and the two radio sources GS17d & GS17e.

AzTEC/GS18. There are two faint radio sources within the 9.3″ search radius of AzTEC/GS18. The closest IRAC/MIPS source GS18a is formally a robust counterpart owing to its proximity to the AzTEC position and its very red IRAC color ($[3.6\mu m] - [4.5\mu m] = +0.47$, $P_{color} = 0.113$). Additionally, GS18b is a $z = 2.688$ galaxy which is an X-ray source detected by *Chandra* (Akiyama 2005) and has

a red IRAC color ($[3.6\mu m] - [4.5\mu m] = +0.31$), making it a plausible candidate for the counterpart to AzTEC/GS18. A third radio-faint IRAC/MIPS source GS18c is a tentative candidate based on its MIPS 24 μm emission, but it has very blue colour ($[3.6\mu m] - [4.5\mu m] = -0.39$) and is likely a foreground object. The 870 μm LABOCA source LESS J033243.6−274644 ($S_{870\mu} = 6.4 \pm 1.3$ mJy) is located $\sim8.4''$ south of the AzTEC position, putting GS18a between the AzTEC and LABOCA centroids. Biggs et al. (2011) identified GS18a as a tentative (and only) counterpart to the LABOCA source. This extremely faint optical source ($i = 28.1$, $K > 24.5$) is another high-z candidate with $z_{MR} = 3.00^{+0.56}_{-1.14}$.

AzTEC/GS19. A pair of radio sources, GS19a & GS19b (with $P_{1.4} = 0.102$ and $P_{1.4} = 0.143$, respectively), are strongly favored as the counterparts to AzTEC/GS19 when all statistical measures are taken into account. They form a blended source in the MIPS 24 μm band, and both have red IRAC colors. It is possible that these two sources are physically related and both contribute to the AzTEC emission. No spectroscopic redshift is available for either sources while their photometric redshifts are quite similar ($z_{opt} = 1.83 \pm 0.35$ & 2.08 ± 0.25). At $z = 2.0$, their projected separation of 3.2″ corresponds to 27 kpc. There is a third IRAC/MIPS counterpart, GS19c, that is a tentatively counterpart with a lower likelihood ($P_{24\mu} = 0.181$). No nearby source is found in the 870 μm LABOCA catalog, but the LABOCA map shows a $S/N \sim 2.4$ emission peak near GS19a & GS19b.

AzTEC/GS20. The AzTEC contours are well centered and follow the light profile of the $z = 0.0369$ galaxy GS20a, which is also a bright and well resolved radio, MIPS 24 & 70 μm, and X-ray source. This source is quite blue ($[3.6\mu m] - [4.5\mu m] = -0.43$) and is obviously a bright foreground galaxy. It is the brightest BLAST 250 μm source within the GOODS-South survey field proper, and Dunlop et al. (2010) argue that this foreground galaxy is the correct counterpart for the BLAST source. It is possible that the 1.1 mm emission originates from the cold dust associated with this spiral galaxy (as seen in the HST images), but it is difficult to reproduce the entire measured spectral energy distribution from $\lambda = 1$ μm to 20 cm using a reasonable set of assumptions on dust temperature, IR luminosity, and star formation rate for this low redshift galaxy. Instead, the AzTEC emission may originate from a background object, possibly lensed by this foreground galaxy, similar to AzTEC J100008.05+022612.2 imaged at high angular resolution by Younger et al. (2007).

AzTEC/GS21. The single tentative radio counterpart (GS21a) has $[3.6\mu m] - [4.5\mu m] = +0.24$ and a spectroscopic redshift of $z = 1.910$ (Vanzella et al. 2008). The position centroid of the BLAST 250 μm source 861 is displaced by $\sim7''$ to the northeast, but GS21a is still within the error-circle of the BLAST source. No nearby source is found in the 870 μm LABOCA catalog, but the LABOCA map shows a $S/N \sim 1.8$ emission peak near GS21a. A second tentative counterpart GS21b is a red IRAC/MIPS galaxy located just 2.5″away from the AzTEC centroid.

AzTEC/GS22. The faint radio source GS22a, located 7.8″ away from the AzTEC centroid, is the most likely coun-

terpart ($S_{1.4} = 34.6 \pm 6.5$ μJy). This galaxy is also a red IRAC/MIPS source ([3.6μm] − [4.5μm] = +0.30) and has a spectroscopic redshift of $z = 1.794$ (Wuyts et al. 2009). The 250 μm BLAST source 552 position centroid is ~10″ east of the AzTEC position, and Dunlop et al. (2010) also identified the radio source GS22a (located ~7″ away from the BLAST position) as the likely counterpart. A second red IRAC/MIPS candidate counterpart, GS22b, is closer to the AzTEC centroid and is an interesting alternative. No nearby source is found in the 870 μm LABOCA catalog, but the LABOCA map shows a $S/N \sim 3.1$ emission peak near this red IRAC/MIPS source GS22b.

AzTEC/GS23. The faint radio source GS23a ($S_{1.4} = 23.4 \pm 6.5$ μJy; $P_{1.4} = 0.030$) is a robust counterpart, and its red IRAC color ([3.6μm] − [4.5μm] = +0.45) adds to the high likelihood of being the correct counterpart. A second tentative radio counterpart, GS23b is only slightly further from the AzTEC centroid, and it is a red IRAC/MIPS source with a spectroscopic redshift of $z = 2.277$ (Chapin et al. 2011). Both GS23a & GS23b are within the beam area of the 870 μm LABOCA source LESS J033221.3−275623 ($S_{870\mu} = 4.7 \pm 1.4$ mJy) and the 250 μm BLAST source 158. Dunlop et al. (2010) and Biggs et al. (2011) have identified GS23b as the counterpart consisting of "an extremely complex faint system" at optical wavelengths.

AzTEC/GS24. There is a single tentative faint radio counterpart within the 12.2″ counterpart search radius, GS24a. This red IRAC/MIPS source is the most likely counterpart to AzTEC/GS24. The 250 μm BLAST source 104 straddles GS24a and a $z = 2.578$ type 2 QSO J033235.78−274916.82 (Rigopoulou et al. 2009, also detected at MIPS 70 μm), and both sources likely contribute to the 250 μm continuum. Dunlop et al. (2010) instead identified the $z = 0.547$ radio source located at the edge of the AzTEC and BLAST beam based on the radio P−statistic. No nearby source is found in the 870 μm LABOCA catalog, but the LABOCA map shows a $S/N \sim 3$ emission peak near the $z = 2.578$ type 2 IR QSO J033235.78−274916.82 and a secondary $S/N \sim 2$ emission peak near GS24a. The AzTEC contours are elongated in the north-south direction, and this may be another example of a blended source.

AzTEC/GS25. The red IRAC/MIPS source associated with radio emission GS25a is located only 6.8″ away from the AzTEC centroid position. This galaxy, also detected in the X-ray by *Chandra*, has a spectroscopic redshift of $z = 2.292$ (Popesso et al. 2009). The 870 μm LABOCA source LESS J033246.7−275120 ($S_{870\mu} = 5.9 \pm 1.3$ mJy) is well-centered on GS25a, and Biggs et al. (2011) also identify the same galaxy as the robust LABOCA counterpart.

AzTEC/GS26. AzTEC/GS26 has no radio counterpart within the 12.2″ search radius of the AzTEC position, but there are five red IRAC sources. Of these, GS26a ([3.6μm] − [4.5μm] = +0.22; $P_{color} = 0.237$) located 5.5″ away is the most probable counterpart to this AzTEC source. GS26b and GS26c are other red IRAC sources located slightly further away (∼ 7″). No nearby source is found in the 870 μm LABOCA catalog, but the LABOCA map shows a $S/N \sim 2.9$ emission peak near the $z = 2.331$ MIPS galaxy J033216.3−274343.4 with a red IRAC color ([3.6μm]

− [4.5μm] = +0.35), located ∼ 7.5″ away from the AzTEC position.

AzTEC/GS27. The red IRAC/MIPS source GS27a ([3.6μm] − [4.5μm] = +0.38) is located 13.0″ away from the AzTEC centroid, just within the counterpart search radius of 13.0″, and is associated with weak radio emission ($S_{1.4} = 23.6 \pm 6.5$ μJy) from a $z = 2.577$ (Popesso et al. 2009) galaxy. However, formally this is not a secure identification ($P_{1.4} > 0.20$) owing to its large separation from the AzTEC centroid. Still, this is the most plausible counterpart within the proximity of AzTEC/GS27. No nearby source is found in the 870 μm LABOCA catalog, but the LABOCA map shows a $S/N \sim 3.1$ emission peak near this red IRAC/MIPS source GS27a.

AzTEC/GS28. AzTEC/GS28 has no radio source within the 13.0″ counterpart search radius. The red IRAC sources GS28a ([3.6μm] − [4.5μm] = +0.55; $P_{color} = 0.073$) and GS28b ([3.6μm] − [4.5μm] = +0.07; $P_{color} = 0.136$) are the most likely counterparts. No nearby source is found in the 870 μm LABOCA catalog, but the LABOCA map shows an extended source with a $S/N \sim 3.0$ emission peak near the AzTEC source position, and this may be another blended source.

AzTEC/GS29. There are no compelling counterparts to AzTEC/GS29. The closest IRAC/MIPS source GS29a (3.8″ away) is very blue ([3.6μm] − [4.5μm] = −0.43) and has a spectroscopic redshift of $z = 0.577$, so this is likely a foreground source. The next closest source GS29b is a $z = 2.340$ galaxy located 4.6″ away, but it is also blue ([3.6μm] − [4.5μm] = −0.10). There are two radio sources located just outside the 13.0″ search radius, but they both have relatively high probabilities of being false associations. No nearby source is found in the 870 μm LABOCA catalog, but the LABOCA map shows an extended source with two $S/N \sim 2$-3 emission peaks near the red IRAC/MIPS sources J033158.65−274516.3 and J033200.13−274453.2.

AzTEC/GS30. The brightest MIPS 24 μm source within the counterpart search radius of 13.5″ ($S_{24\mu} = 459 \pm 6$μJy; $P_{24\mu} = 0.44$) is also a faint radio source ($S_{1.4} = 37.2 \pm 6.2$μJy; $P_{1.4} = 0.082$) with a red IRAC color ([3.6μm] − [4.5μm] = +0.19). Therefore, GS30a is a tentative but the most plausible counterpart for AzTEC/GS30. The spectroscopic redshift of this galaxy is yet unknown. A second radio source (GS30b) and a radio-faint IRAC source (GS30c) are also tentative counterparts to AzTEC/GS30, both with red IRAC colors. No nearby source is found in the 870 μm LABOCA catalog, but the LABOCA map shows an extended source with a $S/N = 2.9$ centered on the AzTEC centroid position.

AzTEC/GS31. Both of the two bright MIPS 24 μm sources (GS31b) within the 13.6″ search radius region are associated with faint radio emission. The western source GS31a however is closer (2.7″) to the AzTEC centroid, making it a robust counterpart candidate ($P_{1.4} = 0.015$). The eastern source GS31b is located 7.9″ away and is a tentative counterpart ($P_{1.4} = 0.118$). It is possible that both sources contribute to the 1.1 mm emission detected by AzTEC. They both have *blue* IRAC colors ([3.6μm] − [4.5μm] = −0.25 and −0.36 for GS31a and GS31b, respectively) however, and the true counterpart may be a much fainter source

located between or behind these sources. The spectroscopic redshift of GS31a is $z = 1.843$ (Wuyts et al. 2009). No nearby source is found in the 870 μm LABOCA catalog, but the LABOCA map shows an elongated north-south structure with a $S/N = 2.8$ peak, similar to the AzTEC source morphology, and it is likely another blended source.

AzTEC/GS32. There are three radio counterparts within the 13.5″ search radius of the AzTEC centroid, and all three are also MIPS 24 μm sources. The nearest radio source GS32a ($S_{1.4} = 30.3 \pm 6.8$ μJy, $P_{1.4} = 0.162$; and $S_{24\mu} = 371.1 \pm 11.7$ μJy, $P_{24\mu} = 0.421$), located 9.6″ away from the AzTEC centroid, is the primary candidate by its proximity. The source GS32b is similarly bright in radio and MIPS 24μm bands, but it is slightly further away, 10.5″, from the AzTEC centroid position. Both GS32a and GS32b are quite blue, however; we include GS32c, a faint radio galaxy with red IRAC color, in the catalog as an alternative, although it is located 13.4″ from the AzTEC centroid. No nearby source is found in the 870 μm LABOCA catalog, and no significant emission peak is found at this location in the LABOCA map.

AzTEC/GS33. The faint IRAC source GS33a located 7.4″ from the AzTEC centroid position is associated with a weak radio source ($S_{1.4} = 28.6 \pm 6.2$ μJy). It is also a weak MIPS 24 μm source and has a red IRAC color ($[3.6\mu m] - [4.5\mu m] = +0.34$; $P_{color} = 0.390$). Therefore this galaxy is a tentative candidate counterpart for AzTEC/GS33. No nearby source is found in the 870 μm LABOCA catalog, but the LABOCA map shows an isolated emission peak with $S/N \sim 2.3$ centered near GS33a.

AzTEC/GS34. There is a high density of IRAC sources in this field, but few are located in the immediate vicinity of the AzTEC centroid position. There are no robust or tentative counterparts to AzTEC/GS34: $P > 0.20$ for all sources within the 13.5″ search radius. No nearby source is found in the 870 μm LABOCA catalog, but the LABOCA map shows an emission peak with a $S/N \sim 3.5$ centered near the $z = 1.356$ (Silverman et al., in prep) faint radio and MIPS source GS34a.

AzTEC/GS35. The red IRAC source GS35a, located 2.0″ away from the AzTEC source centroid position, has a robust radio counterpart ($S_{1.4} = 41.3 \pm 6.7\mu$Jy; $P_{1.4} = 0.008$). Its MIPS emission ($P_{24\mu} = 0.027$) and red IRAC color ($[3.6\mu m] - [4.5\mu m] = +0.37$; $P_{color} = 0.022$) make this galaxy a robust counterpart to the AzTEC source. Its spectroscopic redshift is unknown. The second red IRAC source GS35b located 4.9″ away from the AzTEC position ($P_{color} = 0.191$) is undetected at radio or MIPS 24 μm bands. No nearby source is found in the 870 μm LABOCA catalog, and the LABOCA map shows an emission peak with a $S/N \sim 2.1$ centered near the $z = 0.734$ radio-loud QSO J033227.00−274105.0.

AzTEC/GS36. No radio source is detected within the 13.5″ counterpart candidate search radius, and the galaxy GS36a is the only IRAC source with a red IRAC color, $[3.6\mu m] - [4.5\mu m] = +0.68$ ($P_{color} = 0.304$). So this IRAC source is the most promising counterpart candidate, although it has a high probability of false association. Few other potential candidates are present in this field. No nearby source is found in the 870 μm LABOCA catalog, and

the LABOCA map does not show any significant emission peak within the search radius.

AzTEC/GS37. The red IRAC/MIPS source GS37a with $[3.6\mu m] - [4.5\mu m] = +0.08$ is associated with faint radio emission ($S_{1.4} = 20.5 \pm 6.4\mu$Jy), though it is not formally a tentative counterpart candidate for AzTEC/GS37. There is a single tentative red IRAC source 4.3″ from the AzTEC centroid, which is possibly at high redshift ($z > 3$) given its non-detection at 1.4 GHz. No nearby source is found in the 870 μm LABOCA catalog, but the LABOCA map shows a ridge of 2.1-2.7σ peaks running along the similar ridge found in the AzTEC map (including GS37a), suggesting this is likely another blended source.

AzTEC/GS38. There is a single tentative radio counterpart (GS38a; $P_{1.4} = 0.116$), which is also a *Chandra* X-ray source. It has a very blue IRAC color ($[3.6\mu m] - [4.5\mu m] = -0.55$) and a spectroscopic redshift of $z = 0.735$ (Vanzella et al. 2008). Therefore GS38a is likely a foreground object. No nearby source is found in the 870 μm LABOCA catalog, but the LABOCA map shows a 2.3σ peak near the red IRAC/MIPS source GS38b, located 7.4″ away from the AzTEC centroid ($P_{24\mu} = 0.453$, $P_{color} = 0.386$).

AzTEC/GS39. There is a single tentative radio counterpart (GS39a; $P_{1.4} = 0.083$) which is also a red IRAC source ($[3.6\mu m] - [4.5\mu m] = +0.55$). The position centroid of the 870 μm LABOCA source LESS J033154.4−274525 ($S_{870\mu} = 3.8 \pm 1.4$ mJy) is offset from GS39a by only 4.9″. Biggs et al. (2011) also identify GS39a as a tentative LABOCA counterpart, and GS39a is a strong counterpart candidate for AzTEC/GS39. Another tentative counterpart, GS39b, is a MIPS source located only 2.8″ from the AzTEC centroid, but given its blue color, it is likely a foreground object.

AzTEC/GS40. There are no compelling counterparts to AzTEC/GS40. We list a single IRAC source within the 15.0″ search radius. GS40a is 10.2″ away, and is slightly blue with a high probability of being a false association. No nearby source is found in the 870 μm LABOCA catalog, and the LABOCA map shows only a 2σ emission peak located $\sim 10''$ northwest of the AzTEC position.

AzTEC/GS41. The radio sources GS41a and GS41b are both promising counterparts to AzTEC/GS41 with $P_{1.4} = 0.120$ & 0.132. They are also red IRAC sources with $[3.6\mu m] - [4.5\mu m] = +0.23$ & $+0.30$ although they are just far enough away from the AzTEC centroid to make them tentative counterparts only. Two other red IRAC sources GS41c and GS41d are slightly closer to the AzTEC centroid and are tentative counterparts as well. The centroid of the 870 μm LABOCA source LESS J033302.5−275643 ($S_{870\mu} = 12.0 \pm 1.2$ mJy) is located closest to GS41b and GS41d, and Biggs et al. (2011) identify GS41b as the robust counterpart to the LABOCA source.

AzTEC/GS42. There are no radio counterparts within the 6.9″ search radius of AzTEC/GS42. The only tentative counterpart is GS42a, a red IRAC source ($[3.6\mu m] - [4.5\mu m] = +0.04$) that is also well-matched to the position of the LABOCA source LESS J033314.3−275611 ($S_{870\mu} = 14.5 \pm 1.2$ mJy). The AzTEC contours are extended in the north-south direction, and Weiss et al. (2009) modeled this source

with a second, fainter component (LESS J033313.0−275556, $S_{870\mu} = 4.3 \pm 1.4$ mJy). Biggs et al. (2011) identified adjacent red IRAC/MIPS source J033314.41−275612.0 as the robust LABOCA counterpart.

AzTEC/GS43. The only tentative counterpart is a red IRAC source GS43a, which has a red IRAC color ([3.6μm] − [4.5μm] = +0.23) and is also centered on the 870 μm LABOCA source LESS J033302.9−274432 ($S_{870\mu} = 6.7\pm1.3$ mJy). Since this object is undetected in the radio and MIPS 24 μm, it is also likely a high redshift object ($z_{MR} > 4.1$). Biggs et al. (2011) did not find any robust or tentative counterpart for the LABOCA source. The AzTEC contours are significantly elongated in the east-west direction, suggesting this is a blend of more than one source. Weiss et al. (2009) model this source with a fainter second component, LESS J033303.9−274412 ($S_{870\mu} = 5.3 \pm 1.4$ mJy).

AzTEC/GS44. There is only one VLA radio source found within the 10.4$''$ search radius centered on the AzTEC peak position. This source GS44a has a flat IRAC color, [3.6μm] − [4.5μm] = −0.07 and is a modest MIPS 24 μm source with $S_{24\mu} = 143.1 \pm 9.3$ μJy. The 870 μm LABOCA source LESS J033240.4−273802 ($S_{870\mu} = 5.0 \pm 1.4$ mJy) is found within the AzTEC search radius, but its centroid is offset from GS44a by 12$''$, just outside the nominal beam area of LABOCA. Another radio source J033239.14−273810.5 at $z = 0.830$ (Le Fevre et al. 2004) is a better candidate for the LABOCA counterpart, but this radio source is located 24$''$ away from the AzTEC centroid, which is well outside the nominal search radius for the AzTEC source. We list the LABOCA flux in the Table, but note the large separation between this source and GS44a.

AzTEC/GS45. Two red IRAC/MIPS sources (GS45b & GS45c) are found within 2$''$ of the AzTEC centroid, and they are the most likely candidate counterparts to the AzTEC source, primarily by their proximity. The 870 μm LABOCA source LESS J033218.9−273738 ($S_{870\mu} = 8.1 \pm 1.2$ mJy) is found within the AzTEC search radius, half way between GS45b and GS45a, the latter of which is a bright MIPS 24 μm source and a VLA radio continuum source with a rather blue IRAC color ([3.6μm] − [4.5μm] = −0.32). A higher resolution K-band image shows that the brighter radio peak is associated with a fainter component, suggesting this is a blended source. GS45b is 5.8$''$ away from the LABOCA centroid, and it is a robust counterpart for both AzTEC and LABOCA sources (Biggs et al. 2011).

AzTEC/GS46. No radio source is found within the 13.0$''$ search radius. The IRAC/MIPS source GS46a located 6.2$''$ away from the AzTEC centroid is the tentative counterpart based on the combination of its red IRAC color ([3.6μm] − [4.5μm] = +0.17; $P_{color} = 0.255$) and MIPS 24 μm emission ($P_{24\mu} = 0.226$). The LABOCA source LESS J033157.2−275633 ($S_{870\mu} = 4.8 \pm 1.4$ mJy) is located 23$''$ from GS46a and thus also far from the AzTEC centroid. We list the LABOCA flux in the table but note this large separation.

AzTEC/GS47. The faint VLA 1.4 GHz radio source GS47a ($S_{1.4} = 43.2 \pm 7.0$ μJy, $P_{1.4} = 0.105$) is found 7.6$''$ away from the AzTEC centroid, and it is also a red IRAC source ([3.6μm] − [4.5μm] = +0.46) as well as a

MIPS 24 μm source. The 870 μm LABOCA source LESS J033208.1−275818 ($S_{870\mu} = 7.3 \pm 1.2$ mJy) coincides in position with AzTEC/GS47 within 3.4$''$ of each other, making it a robust LABOCA counterpart as well (Biggs et al. 2011).

This figure "Figure1.jpg" is available in "jpg" format from:

http://arxiv.org/ps/1109.6286v1